Universidade de São Paulo

Instituto de Física

Dinâmica de partículas carregadas no poço quântico de GaAs/AlGaAs

Eduard Levinson

Orientador: Prof. Dr. Alexandre Levine

Tese de doutorado apresentada ao Instituto de Física como requisito parcial para a obtenção do título de Doutor em Ciências

Banca examinadora:

Prof. Dr. Alexandre Levine (IFUSP - Orientador)
Prof. Dr. José Fernando Diniz Chubaci (IFUSP)
Prof. Dr. Guilherme Matos Sipahi (IFSC/USP)
Prof. Dr. Nilo Maurício Sotomayor Choque (UFT)
Profa. Dra. Ana Melva Champi Farfan (UFABC)

São Paulo

2019

FICHA CATALOGRÁFICA
Preparada pelo Serviço de Biblioteca e Informação
do Instituto de Física da Universidade de São Paulo

Levinson, Eduard

Dinâmica de partículas carregadas no poço quântico de GaAs/AlGaAs. São Paulo, 2019.

Tese (Doutorado) – Universidade de São Paulo. Instituto de Física. Depto. de Física dos Materiais e Mecânica

Orientador: Prof. Dr. Alexandre Levine
Área de Concentração: Física

Unitermos: 1. Medições de magnetoresistência; 2. Transporte balístico; 3. Transporte hidrodinâmico.

USP/IF/SBI-093/2019

University of São Paulo

Physics Institute

Charged particle dynamics in GaAs/AlGaAs quantum well

Eduard Levinson

Supervisor: Prof. Dr. Alexandre Levine

Thesis submitted to the Physics Institute of the University of São Paulo in partial fulfillment of the requirements for the degree of Doctor of Science

Examining Committee:

Prof. Dr. Alexandre Levine (IFUSP - Supervisor)
Prof. Dr. José Fernando Diniz Chubaci (IFUSP)
Prof. Dr. Guilherme Matos Sipahi (IFSC/USP)
Prof. Dr. Nilo Maurício Sotomayor Choque (UFT)
Profa. Dra. Ana Melva Champi Farfan (UFABC)

São Paulo

2019

Acknowledgments

Throughout the writing of this thesis I have received a great deal of support and assistance. I would like to thank to the University of São Paulo for giving me the opportunity to do my PhD work. Also, I am grateful for the financial support provided by Brazilian federal government agency. This study was financed in part by the Coordenação de Aperfeiçoamento de Pessoal de Nível Superior - Brasil (CAPES) - Finance Code 001. I would like to express my special thanks to the Department of Physics Materials and Mechanics, where I did the main research work as a member of the Prof. G. Gusev's laboratory.

The experimental work would be impossible without, the high-quality samples which were produced in the Institute of Semiconductor Physics in Novosibirsk Russia for samples processing.

Also, I would like to give thanks to the Department of Electronic Systems Engineering of Polytechnic School of the University of São Paulo for provide the access to the clean room. I spent mostly of samples processing time in this clean room.

Resumo

Neste trabalho apresento um estudo do magnetotransporte (MT) em poços quânticos de amostras de GaAs em baixos campos magnéticos. A ideia de estudar MT em GaAs poços quânticos veio dos resultados das medições de amostras de HgTe. Alguns desses resultados são apresentados no Apêndice I. Medi a magnetorresistência em configurações locais, não locais e Hall. Além disso, estudei uma resposta do sistema de amostras de GaAs à irradiação de microondas (MR).

A tese está composta por três capítulos, cinco anexos e cinco apêndices. No capítulo primeiro é dada a base teórica do magnetotransporte em 2DES. No final do primeiro capítulo, são descritos brevemente diferentes regimes de transporte que podem ser observados no 2DES.

Amostras e configurações experimentais são descritas no capítulo segundo. Este capítulo fornece uma descrição da preparação da amostra, padrões que foram usados durante a fotolitografia para fazer a estrutura 2D, e a configuração experimental que foi empregada neste trabalho.

No capítulo terceiro, medições de MT de GaAs são apresentadas, e é a parte principal da tese. Primeiro, o modelo balístico foi comparado com os resultados experimentais, reveleando que o transporte de elétrons tem um caráter complicado e não pode ser descrito por apenas um modelo. Supomos que o transporte de elétrons em nossas amostras tenha transporte hidrodinâmico além de balístico. Assim, o experimento foi continuado para esclarecer a natureza do transporte de elétrons em nossas amostras. Realizamos medições nas configurações local, não local e Hall, com diferentes direções de fluxo de corrente e arranjos para sondas de tensão. Observamos a contribuição dinâmica para o transporte de elétrons. Também confirmamos o efeito Gurzhi previsto teoricamente em nossas amostras.

Os apêndices consistem no trabalho experimental e teórico que não foi incluído no texto principal. O primeiro, são medições de MR de amostras de HgTe e comparação dos resultados experimentais com a teoria. O segundo apêndice é sobre as medidas de MR de amostras de Ge:P. Este trabalho foi feito em colaboração com outro laboratório. Terceiro, consistem em medidas de MR de amostras de GaAs sob excitação de MW. Nos dois últimos apêndices são discutidas algumas questões que apareceram durante o trabalho teórico e análise de resultados.

Os anexos consistem em artigos e uma apresentação de pôster. Primeiro, são as medidas de MR do germânio dopado. Em segundo lugar, é o poster sobre as medidas de MR no GaAs e a

comparação teórica. Os últimos três anexos são sobre medidas de MR de amostras de GaAs e a comparação com a teoria.

Palavra-chave: medições de magnetoresistência, preparação de amostras de GaAs, fotolitografia, transporte balístico, transporte hidrodinâmico.

Abstract

In this thesis, I present a study of the magnetotransport (MT) in the quantum wells of GaAs samples in the low magnetic fields. The idea of studying MT in the GaAs quantum wells (QWs) appeared as a result of measurements of HgTe samples. The effects of MT observed in the HgTe samples required strong numerical analysis. Some of the results are presented in Appendix I. We have measured magnetoresistance in local, non-local and Hall configurations during the Ph.D. In addition, I have studied a system response of GaAs samples to microwave (MR) irradiation.

The thesis consists of three chapters, five attachments, and five appendixes. In the first chapter, I give a theoretical basis of the magnetotransport in two dimensional electron system (2DES). At the end of the first chapter, I describe different transport regimes which can be observed in 2DES.

Samples and experimental setup are described in the second chapter. This chapter provides a description of samples processing, patterns that I used in photolithography, and experimental setup used for this work.

In the third chapter of the thesis, I explain MT measurements of GaAs. It is the main part of this work. First, we compared a ballistic model with the experiment. It revealed that electron transport has complicated character, and it is necessary more than one model for be described. We supposed that the electron transport in our samples has hydrodynamic transport besides ballistic. Thus, the experiment was continued to clarify the nature of electron transport in the structures. We performed measurements at local, non-local, and Hall configurations with different current flow directions and arrangements for voltage probes. We observed the dynamic contribution to the electron transport. We also confirmed theoretically predicted Gurzhi effect in our samples.

Appendixes consist of supplementary experimental and theoretical. First, consist of MR measurements of HgTe samples and comparison experimental results with theory. Second appendix is about MR measurements of GeP samples. This work was done in collaboration with another laboratory. Third appendix consist of MR measurements of GaAs samples under MW excitation. In the last two appendixes are discussed some questions which appeared during the theoretical work and results analysis.

Attachments consist of four articles and one poster presentation. First, is the MR measurements of doped germanium. Second, is the poster about MR measurements in the GaAs with

theoretical comparison. Last three attachments are MR measurements of GaAs samples with analysis of the results.

Key words: magnetoresistance measurements, GaAs samples processing, photolithography, ballistic transport, Hydrodynamic transport

Contents

List of figures

Introduction

First anisotropic magnetoresistance (AMR) effects were observed in the experiments by W. Thomson in 1857. In his experiments, he discovered that magnetoresistance depends on the direction of the applied magnetic field to sample. His experiments were starting point in transport measurements. In 1879 E. Hall discovered the effect that later took his name. He observed that, if put sample with a current in the magnetic field it is possible to observe the difference in the perpendicular voltage. Going deeply in condensed matter physics, H. K. Onnes discovered superconductivity in 1911. Super fluidity in ^{4}He was discovered by P. Kapitsa in 1938, in 1947 J. Bardeen made bipolar junction transistor. In 1972, super fluidity was discovered in ^{3}He. Then, in the 1980s when nanofabrication technology began, was discovered giant magnetoresistance (GMR). GMR is a quantum mechanical phenomena that can be observed in thin films with alternate ferromagnetic and conducted nonmagnetic layers. This phenomenon consists of a change in magnetoresistance with a change in the direction of magnetization of neighboring layers. By changing the applied magnetic field is possible to control the direction of magnetization. The basic principle of this phenomena is electrons scattering what depends on the spin direction. At this time, there were many other discoveries that were observed in 2DES. Such as integer quantum Hall effect (IQHE). The related effect, which called the Shubnikov-de Haas oscillations. And fractional quantum Hall effect (FQHE) what can be observed in the higher magnetic fields.

Since the 1980s, significant progress has been made in understanding the electron transfer in micro and nanometer systems. Successful fabrication of modern electronic components, for example ballistic field-effect transistors, requires a fundamental understanding of the mechanism of charge carrier transport. The commonly accepted mechanism for the transport properties is described by semi classically or by the Landauer-Buttiker formalism. These models are based on the assumption that the rate of momentum conserving scattering exceeds that of momentum relaxation scattering. In this thesis I worked with two different transport models.

First, is the semi classical approach. Magnetoresistance is a perfect tool for experimental studies of electronic systems. Magnetoresistance is a change in the resistivity of a material in an applied magnetic field. Which depends on the strength of the magnetic field and it relative direction to the current.

Second, is the hydrodynamic approach. There has been increasing interest in the fabrication of devices with new types of functionality whose operation is determined by new principles. The hydrodynamic regime of a Fermi liquid of electrons in a 2D system is reachable when the mean free path for electron-electron collisions l_{ee} is smaller than the mean free path with static defects and phonons l, and transport resembles a viscous electron flow.

This thesis is dedicated to the study of transport phenomena in low dimensional systems in the presence of external fields. The main part of the thesis is devoted to the measurenments of longitudinal and Hall resistance. In addition, non-local resistance measurements are presented. These measurements helped to characterize electronic transport such as electron-electron, electron-hole scattering times. Also, I present in this thesis an electron transport in a certain temperature range with a constant magnetic field. Moreover, the electron transport in the samples at the MW irradiation have been studied.

The research started with the MR measurements of GaAs QWs. Measurements were carried out to study the local, Hall, and non-local electron transport. We observed features related to ballistic regime of electron transport. It had a significant effect on resistance, which demonstrates power and frequency dependence. The next step was to compare the theoretical calculations from the ballistic model with experimental data to interpret this effect. I participated in developing a numerical simulation tool to calculate the contribution of the ballistic conduction effect, which facilitated analyzes. Results of this work I presented on 18th Brazilian workshop on semiconductor physics which was at August of 2017. The poster is attached in [II].

Further measurements revealed more interesting features of the samples. During the experiments were found that the probe configuration and sample geometry strongly affects the temperature evolution of local resistance. These transport properties can be attributed to the presence of hydrodynamic effects. Experimental results confirmed the theoretically predicted significance of viscous flow in mesoscopic devices. This work is publication in *AipAdv.**8**.025318 (2018)* and is presented in the attachment [III].

Another important finding was an observation of the negative nonlocal resistance. It was supposed what whirlpools are formed in the electron flow. To clarify this effect I participated in different measurements using different samples with different geometries of nonlocal transport. Then experimental data was compared with the simulation's results based on the

hydrodynamic model. This work is publication in *PhysRevB.**97**.245308 (2018)* and is presented in attachment [IV].

Also, a negative Hall resistivity was observed in the experiments. For experiments, we used mesoscopic size samples at the low magnetic field. The observed effect was attributed to Hall viscosity in the inhomogeneous charge flow. Hall viscosity is a nondissipative response function describing momentum transport in 2D systems with broken time-reversal symmetry. In the classical regime, Hall viscosity contributes to the viscous flow of 2D electrons in the presence of a magnetic field. Experimental results supported by a theoretical analysis confirmed that the conditions for observation of Hall viscosity are correlated with predictions. This work is publication in *PhysRevBRapidComm..**98**.161303 (2018)* and is presented in attachment [V].

Additionally I helped to measure the longitudinal magnetoresistance on heavily P-doped germanium samples. The experimental results have compared to those from a many-body theory where the donor-electrons are assumed to reside at the bottom of the many-valley conduction band of the host. Good qualitative agreement between theory and experiment was obtained. This work is attached in [I].

Chapter 1

1 The basis of 2-dimensional electron systems

1.1 Magnetotransport in 2DES

Description of electronic transport in a solid is a very interesting and competitive task. It can be described by a many-body quantum mechanical approach. A many-body approach includes a total number of particles and interactions between them and with the external environment. Without simplification, such type of approach has too many variables for computational methods. Below, in the ***Fig. 1*** is presented the hierarchy of the models from the simplest which gives approximate solution to the complicated which gives more precise solution.

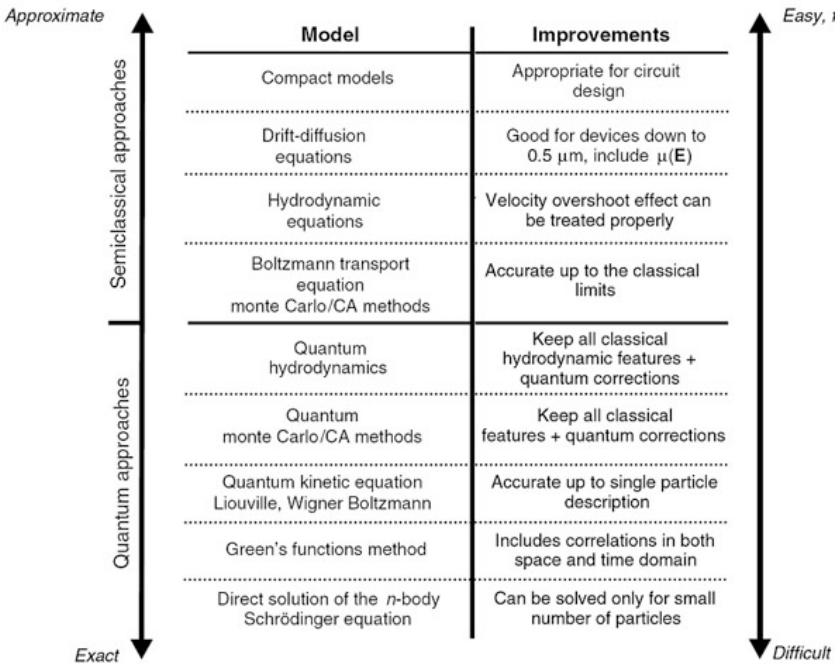

Fig. 1 *Connection of different approaches which describe MT. Adapted from [1].*

Also, the characteristic length scale of samples can change the transport behaviour from classical to quantum. Depending on it, the transport can be purely classical, purely quantum or, under certain conditions, a mixture of both.

1.1.1 Semiclassical model

First I want to start from the Drude theory. This is a classical theory that explains electron transport in metals. Drude suggested this theory at the 1900 one year after the electron was discovered. In this theory, electrons are treated as an electron gas which can be described by applying the kinetic theory of gases. In this case, electrons are same solid spheres that move straight before they collide. It is assumed that the collision time is infinitely short and there are no forces between particles other than the moment of collision. There are some general proposes of Drude theory. First, there is no electron-electron interaction between collisions, this means that without external electromagnetic fields electrons move straight with constant speed. In the presence of an external electromagnetic field, electrons move according to Newton's law. Additional fields generated by interaction with other particles don't take into consideration. Second, all collisions occur instantaneously, which means that the speed and direction of electron change immediately. Third, the probability of collision for an electron for infinitely small time dt has this form: $\mathrm{P} = \frac{\mathrm{dt}}{\tau}$, where τ is a relaxation time.

Based on these assumptions, the general equation of motion in the semiclassical model can be written as:

$$m\frac{d\vec{v}}{dt} = -m\frac{\vec{v}}{\tau} - e(\vec{E} + \vec{v} \times \vec{B}), \qquad (1.1)$$

where $m\frac{\vec{v}}{\tau}$ is a scattering force due to disorder. The constant drift velocity can be find from the ***eq. (1.1)*** under the steady state conditions. It has the following form $\vec{\mathrm{v}}_{\mathrm{D}} = -\frac{e\tau}{m}\vec{E}$, where $\frac{e\tau}{m}$ is a mobility μ. Also conductivity and resistivity for the case without magnetic field are $\sigma_0 = \mathrm{n}e\mu$ and $\rho_0 = {}^{1}/_{\sigma_0}$ respectively.

In the presence of a magnetic field perpendicular to 2DES, the electric field generated by the current has the form:

$$\begin{pmatrix} E_x \\ E_y \end{pmatrix} = \begin{pmatrix} \rho_{xx} & \rho_{xy} \\ \rho_{yx} & \rho_{yy} \end{pmatrix} \begin{pmatrix} j_x \\ j_y \end{pmatrix} = \begin{pmatrix} {}^{1}/_{ne\mu} & {}^{B}/_{ne} \\ -{}^{B}/_{ne} & {}^{1}/_{ne\mu} \end{pmatrix} \begin{pmatrix} j_x \\ j_y \end{pmatrix} = \begin{pmatrix} \rho_L & \rho_H \\ -\rho_H & \rho_L \end{pmatrix} \begin{pmatrix} j_x \\ j_y \end{pmatrix}, \qquad (1.2)$$

where for the isotropic system the longitudinal resistivity ρ_{L} is equal to the ρ_0 and ρ_{H} is a Hall resistivity. Negative sign significates different polarity of the Hall electric filed. The resistivity tensor is the inverse of the conductivity tensor, finally, components of the resistivity tensor are:

$$\rho_L = \frac{\sigma_L}{\sigma_L^2+\sigma_H^2} \text{ and } \rho_H = \frac{\sigma_H}{\sigma_L^2+\sigma_H^2}. \quad (1.3)$$

To measure resistivity from the experiment it is necessary to know the current flow and sample geometry. For example, for Hall bar structure (***Fig. 2***) the longitudinal and Hall resistivity can be written as $\rho_{\mathrm{L}} = \mathrm{R_L}\frac{\mathrm{W}}{\mathrm{L}}$ and $\rho_{\mathrm{H}} = \mathrm{R_H}$, respectively. Hall bar geometry excludes the influence of contact resistance.

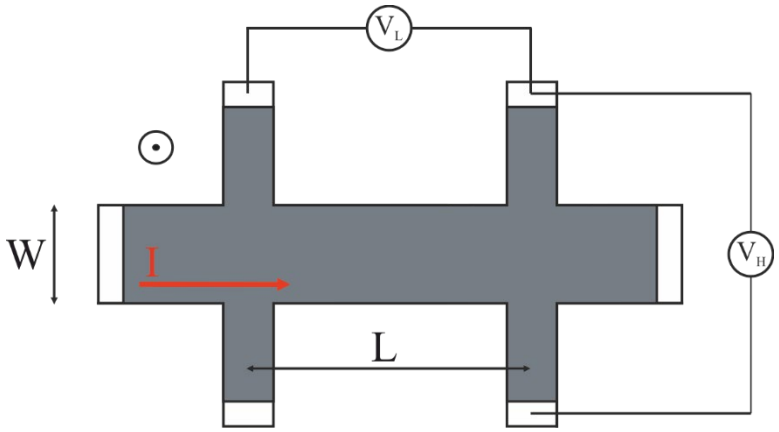

Fig. 2 *Schematic of the Hall bar structure.*

1.2 2D electron system

In a 2DES, electrons are free to move in a plane and in the direction perpendicular to the plane electrons are confined in the energetic potential well. A typical realization of 2DES are semiconductor heterojunctions. As an example, the 2DES is located in the quantum well, formed by 2 layers of AlGaAs on the sides and GaAs inside is schematically presented below in the ***Fig. 3***.

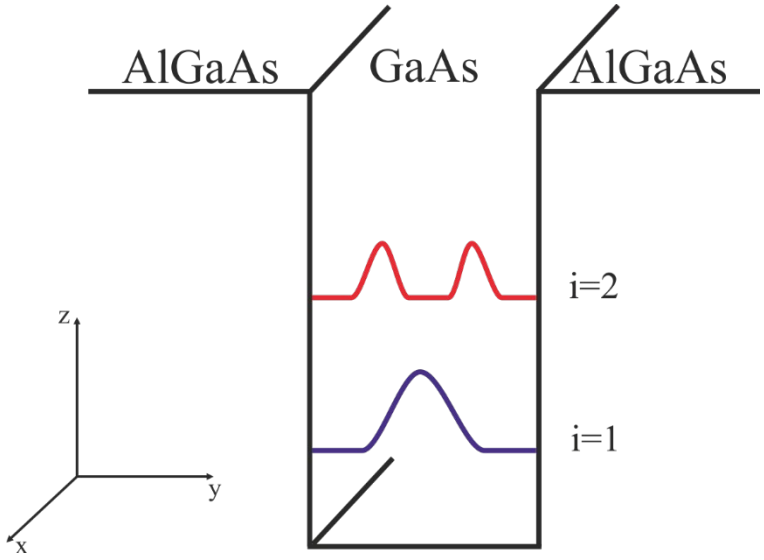

Fig. 3 *Probability density of 2 lowest wave functions in a quantum potential well.*

The total energy of electrons can be found from the Shcrödinger equation:

$$(-\frac{\hbar^2}{2m}\nabla^2 + V(z))\psi = E\psi. \tag{1.4}$$

Due to the fact that the potential depends only on z-direction the electron states are quantized but also they have free motion in x – y plane. Taking into account previous assumptions the electron wave function can be written as $\psi(x,y,z) = \varphi_n(z)e^{ik_x+ik_y}$. Then, the next step is the separation of Shcrödinger equation. Thus the solution for the total energy of electrons has the following form:

$$E_n = \varepsilon_n + \frac{\hbar^2(k_x^2+k_y^2)}{2m}, \tag{1.5}$$

where the total energy E is a sum of quantized energy ε_n in z direction and energy in the x – y plane.

For the case when the 2DES placed in magnetic field the ***eq. (1.4)*** is modified:

$$(\frac{1}{2m}(\vec{P} - \frac{e}{c}\vec{A})^2 + V(z))\psi = E\psi, \tag{1.6}$$

where $\vec{P} = -i\hbar\nabla$ and $\vec{A}$ is a vector potential. Thus, the total energy of the system is:

$$E_{n,i} = \varepsilon_n + (i + \frac{1}{2})\hbar\omega_c, \tag{1.7}$$

where $\omega_c = \frac{eB}{m}$ is the cyclotron frequency.

1.3 Transport regimes in 2DES

The behavior of electron transport in a low dimensional system, depends on the characteristic lengths in the active region of a sample. In the ***Fig. 4*** is presented the active region of a sample with a length L, and a width W of the conducting channel. The electronic mean free path between collisions is labeled as l_e. Collisions occur due to the samples inperfections such as impurities or irregularities in a device. The mean free path l_e is possible to express as: $l_e = \tau_e v_F$. Where τ_e is the electron scattering time and $v_F = \frac{p_F}{m}$ is the Fermi velocity with the momentum $p_F = (2\pi n)^{1/2}$.

Also, the phase breaking length l_Ψ appears in the ***Fig. 4*** as the addition scale parameter. This is the length scale at which quantum coherence is maintained. The latter is often associated with environmental issues and results in quantum mechanical phase breaking. At low temperatures the phase braking length can be much larger than the mean free path l_e. In this thesis the electron transport was described by classical or semi classical models. In this case, the phase breaking length have to satisfy the following condition: $l_\Psi < l_e$.

The different mean free path l_e in comparison with the dimensions of a device can reveal different transport regimes. Fig. 4 (a) illustrates the case when the L and W are much larger than the electron mean free path $l_e \ll$ L, W. This is a purely diffusive transport, and the system behaves like a semiclassical metal or semiconductor.

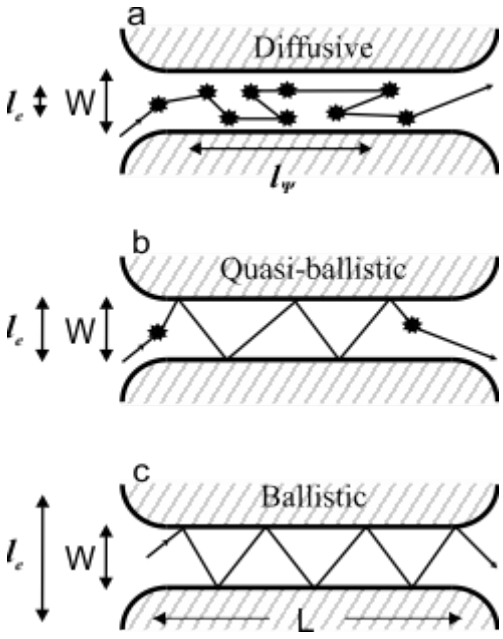

Fig. 4 *Transport in nanostructures for diffusive (a), quasi-ballistic (b), and ballistic (c) regimes.*

In the ***Fig. 4 (b)***, the width, W, is much smaller than the characteristic mean free path, and the length, L, is much longer than W: $W \ll l_e \ll L$. This regime can be observed in a quantum-confined system where the carrier's motion is quantized in one dimension however has diffusive motion in others. In the last ***Fig. 4 (c)*** the system is purely ballistic, which means that L and W are shorter than the elastic and inelastic mean free paths $L, W \ll l_e$. The motion of charge in this system is determined by the wave-like behavior of the particle and its reflective and transmitting properties through the structure.

Above I described transport regimes which are based on the diffusibe and ballistic models. Also electrons in a conductor, under some conditions, can exhibit hydrodynamic flow. Thus, equations of hydrodynamic can be applied to explain the electron transport.

Such flow of the electrons can be observed in so-called pipe geometry and exhibit Poiseuelle-type flow. It is usually considered that the Poiseuelle-type flow is the axisymmetric flow in an infinitely long, circular pipe. The flow is caused by a pressure gradient in the axial direction. The difference between the motion of molecules in a liquid and the motion of electrons in a crystal lattice creates additional difficulties in applying the equations of hydrodynamics. Electrons have collisions between themselves and also with phonons and impurities. The way to observe the hydrodynamic regime in a conductor is to create a condition when the electron-electron interaction time will be smallest in comparison with another characteristic times such as electron-phonon and electron-impurity scattering times. For the small temperatures the electron-impurity scattering is dominating while the electron-phonon scattering is dominating at high temperatures. Thus, biggest contribution from hydrodynamic regime in the electron transport lies in the temperature window when electron-impurity and electron-phonon scattering are dominating less.
The way to describe hydrodynamic processes in the electron liquid is to solve the Navier-Stockes and continuity equations. In general form these equations for the one-component systems have the following form:

$$\frac{\partial \delta n_e}{\partial t} + \nabla \cdot \vec{j} = 0, \tag{1.8}$$

where δn_e is the deviation of the carrier density and $\vec{j}$ are the carrier's current.

$$\frac{\partial \vec{v}}{\partial t} = \eta \nabla^2 \vec{v} - (\vec{v} \cdot \nabla)\vec{v} - \nabla w + \vec{g}, \tag{1.9}$$

where η is the kinematic viscosity tensor, w is the specific thermodynamic work and $\vec{g}$ is a sum of forces that can be applied to the system.

Chapter 2

2 Samples and experimental setup

2.1 Samples

In the experiments, we studied high mobility electron gas in the GaAs/AlGaAs mesoscopic size samples with narrow QW of 14 nm. These samples were fabricated by molecular beam epitaxy technique (MBE). MBE is a process when one or more thermal evaporated beams of atoms or molecules react with a crystalline surface under ultrahigh vacuum. A schematic representation of the MBE for studied sampels is presented in the ***Fig. 5***.

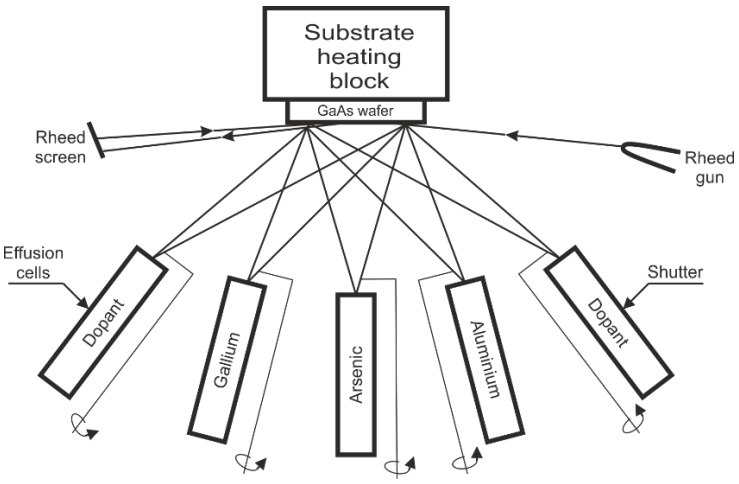

Fig. 5 *The scheme of the MBE growth chamber.*

The substrate, a GaAs wafer, is placed on the substrate holder in the upper part of the vacuum chamber. Molecular beams are generated from effusion cells that are located at the bottom of the chamber. Individual opening or closing of a shutters for effusion cells allows to grow samples with different thikness of the deposited elements. Growing process is controlled by reflection high-energy diffraction (RHEED). This control allows to grow layers with different composition and atomic level thickness.

The samples which were studied consist of narrow 14 nm quantum well with an electron density of $n_s \cong 1.0 \times 10^{12}$ cm^{-2} and mobility of $\mu \approx 1.7 - 3.2 \times 10^6$ cm^2/V s. QW is a potential well with discrete energy levels. For the samples we studied, the QWs were formed as a

sandwich between GaAs and AlGaAs, which have a different bandgaps. The samples structure we studied in the experiments is presented in the ***Fig. 6***.

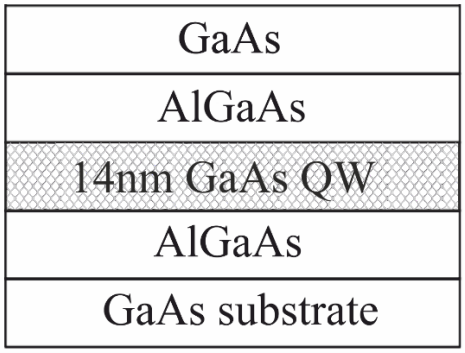

Fig. 6 *Schematic of layer structures of GaAs/AlGaAs QWs.*

It is possible to describe QW as a one-dimensional potential barrier for the quantum particle. Motion in this barrier bounded by two dimensions. The main property of movement of a quantum particle in the potential barrier is discrete energy levels. The QW has a discrete energy levels $E_1 \ldots E_n$ as possible to see in the ***Fig. 7***.

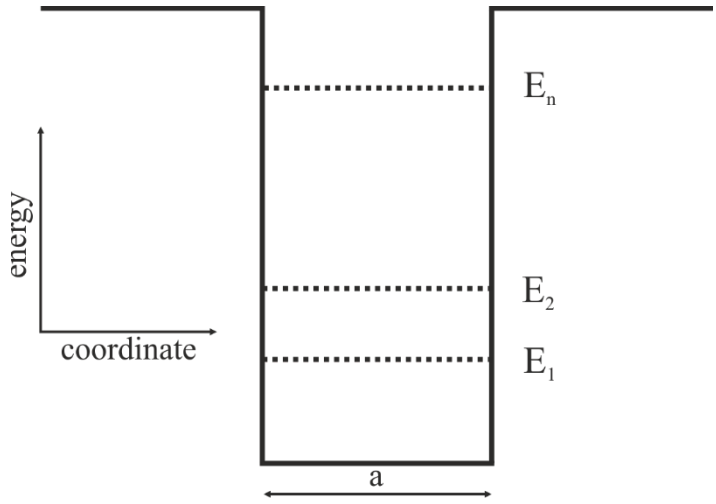

Fig. 7 *Schematic representation of a quantum well.*

2.1.1 Sample processing

To carry out MT measurements it was necessary to make samples with various patterns. Also, pattern scale can affect on electronic transport in the samples.

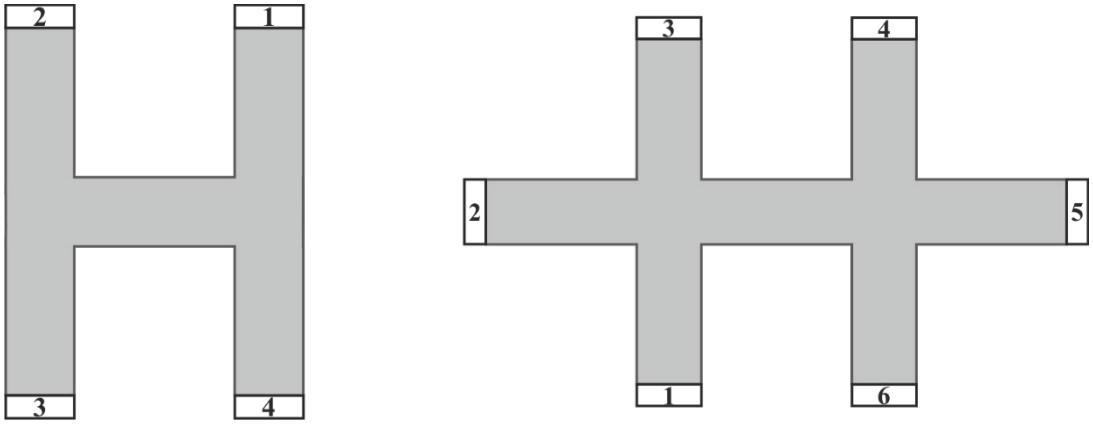

Fig. 8 *Principal geometries to measure non-local transport.*

We used H-bar and Hall-bar geometries in my experiments. Schematically these geometries are presented in ***Fig. 8***. There are some important procedures that had to be performed before raw samples were ready for measurements. First one was the samples processing in a clean room. Some of the steps I have completed are listed below:

1. Samples processing – it is the first step for the samples processing. Samples must be free of any type of contamination. Acetone and alcohol must be used for cleaning samples. Then it is necessary to dry samples with N_2.
2. Spin-Coating – then the samples should be completely covered with a drop of photoresist. For different types of photoresist, the rotational speed of spinor and the rotation time can be different. It is necessary to check carefully and prepare test samples before, to find optimal parameters of the speed and the time to obtain good resolution.
3. Softbake – this step is necessary for better adhesion of the photoresist to the sample surface. Optimal results should be by using the hot plate at T=100°C for 50 seconds.
4. Exposure and development- the exposure time and energy requirements can vary depending on coating thickness, baking conditions, sample reflectivity and the developer concentration. After the exposure, the sample should be placed in the developer. Usual time in the developer is about 50 seconds. Then it is recommended to check the made structure under the microscope for quality. Sometimes it is recommended to place the sample in the developer for a few seconds to remove the residual photoresist.

5. Postbake – postbake is a step that improves image stability, adhesion and chemical resistance. For most samples, it is recommended to use a temperature of about 150°C during 50 seconds.
6. Chemical etching – this step is intended to improve the separation of the layers in the samples after photolithography. Solutions with different chemical activity can be used. For my samples, I used a chemical solution based on orthophosphoric acid. Etching speed depends on concentration and applicable time. Good results should be obtained for 15-20 seconds of etching.

Another important step includes good ohmic contacts. I used indium to deposit metal contacts on GaAs / AlGaAs samples. Then contacts were annealed at 410^0C for 20 min. Annealing improves indium diffusion into the sample volume, which improves contact and reduces parasitic resistance.

Two photographs of samples with different structures are presented in the ***Fig. 9***. The H-bar structure before etching is presented on the left side. The Hall-bar structure after the etching is presented on the right side. As it possible to see, both structures have good resolution. Also, chemical etching improves the structure and makes it more distinct.

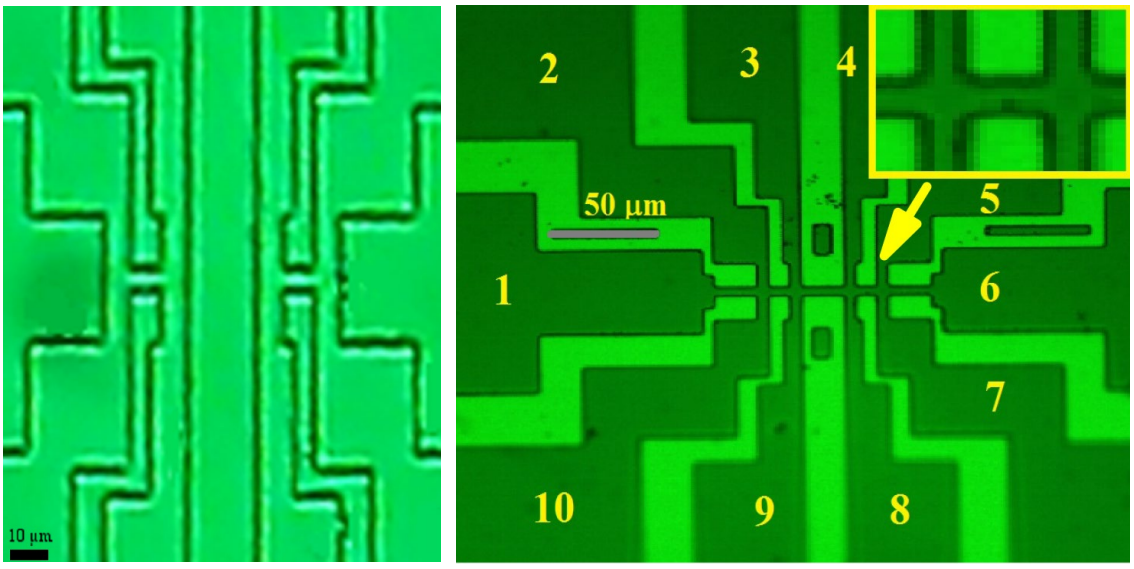

Fig. 9 *Photo of a sample with two H-Shaped structures (left) and 10 contact Hall bar(right) obtained with microscopic resolution. The width of the narrow current channels is about 5 µm.*

2.2 Experimental setup

The study of electron transport in low dimensional structures requires the use some specific equipment. The experimental setup we used included an OXFORD cryostat, a superconducting magnet, and peripheral equipment to control the measurements.

The measurements were carried out in the variable temperature insert (VTI) cryostat. This cryostat allows to reach temperatures up to 4.2K, and 1.5 K with the help of a pump. Such low temperatures are achievable due to a special cryostat device. Thermical isolation of VTI cryostat consists of 3 main volumes. External chamber with liquid N_2 inside, then a vacuum chamber and an internal the chamber with liquid ^4He.

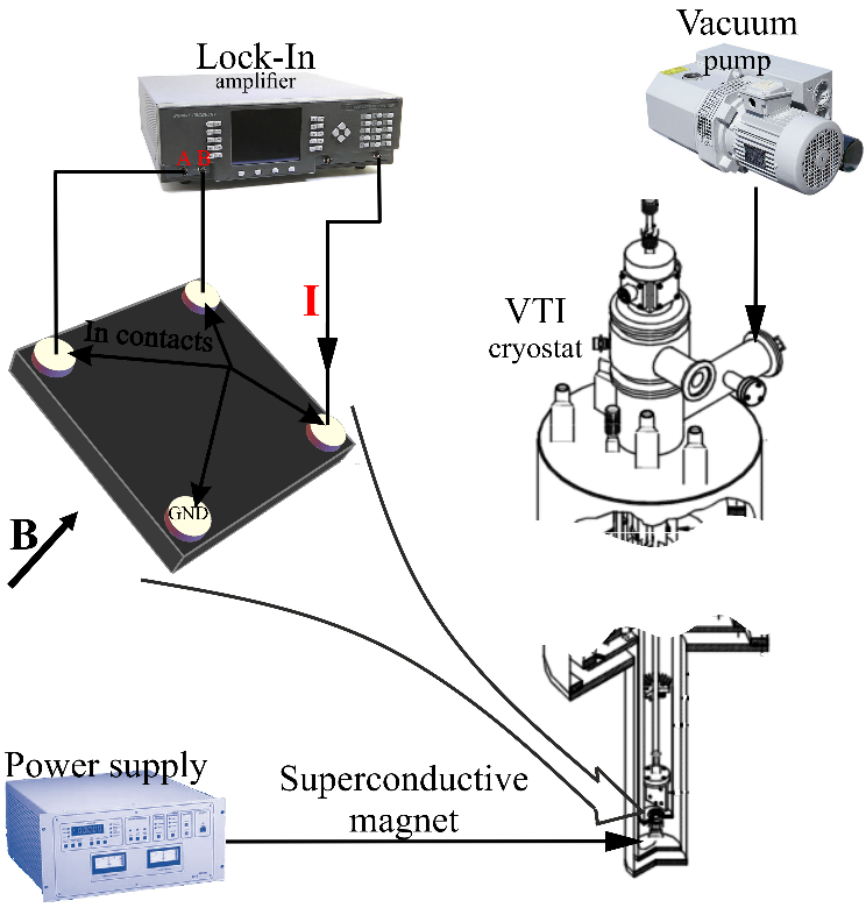

Fig. 10 *Measurement setup consists of VTI (Variable Temperature Insert) cryostat with the superconductive magnet, Lock-In amplifier, and pump. Sample has 4 In contacts arranged in Van der Paw geometry located at the corners of 5 mm × 5mm square. MT measurements are done by the conventional Lock-In technique with* ***SIGNAL RECOVERY*** *(Model 7280) DSP dual phase amplifier, which has a high input impedance of 100 MΩ. For the measurements, we used frequency range from 0.5 Hz to 13 Hz. The sample was located in the superconductive magnet (Oxford) with the perpendicular to its surface magnetic field up to 5 Tesla. Mechanical pump allowed us to rich temperatures down to 1.5 K (copied from* ***Attachment I****).*

A typical measurement arrangement that we used for experiments is presented in the ***Fig. 10***. A sample is placed in a liquid ^{4}He bath that allows it to cool down up to 4.2K. A needle valve allows to control the flow of liquid ^{4}He from the main bath with a sample inside to the VTI. In this case, temperature measurements depend by controlling the flow of fluid of liquid ^{4}He. Also, the experimental setup allows to measure MT at low temperatures up to 1.5K by using a pump that can draw out ^{4}He vapor from VTI. For the measurements under MW excitation, we used the MW generator. It generates and transmits MW through a rectangular waveguide to a sample.

We used generator with frequency ranging from 110GHz to 170GHz. Also, we used an attenuator that permits to control MW power. Samples are usually placed at a distance of 1mm from the waveguide output. Maximum achievable power from the MW generator was 1 mW on the sample surface. MW generator and attenuator, which we used, are presented in the ***Fig. 11***.

Fig. 11 *Elmika G4402E Sweep Generator and attenuator.*

For voltage measurements, we used DSP dual phase Lock-In amplifier **SIGNAL RECOVERY** (Model 7280). Lock-In amplifier is a type of electronic amplifier that uses the principle of synchronous signal detection. The main part of Lock-In amplifier is the phase-sensitive detector (PSD). Lock-In amplifier makes it possible to detect periodic signals with a previously known frequency against a background of very large interference. This reference frequency Lock-In amplifier takes from the signal generator. Then the Lock-In amplifier generating its own internal reference and multiplication by signal at the base frequency that Lock-In amplifier takes from the signal generator. Reference is usually a sine signal:

$$V_{psd} = V_{sig}V_L \, sin(\omega_r t + \theta_{sig}) \, sin(\omega_L t + \theta_{ref}), \qquad (2.1)$$

where V_{psd} is the output signal, $V_{sig} \, sin(\omega_r t + \theta_{sig})$ is the detecting signal, $V_L \, sin(\omega_L t + \theta_{ref})$ is the internal reference signal, ω_r and ω_L is the signal frequency for detecting and reference signal respectively, θ_{sig} and θ_{ref} is the signal phase for detecting and reference signal

respectively. Then, if use the trigonometric formula for cos difference and pass signal V_{psd} through low pass (LP) filter it will remove the AC component. Finally, the output signal which passed through the low pass filter has the following form:

$$V_{psd} = \frac{1}{2} V_{sig} V_L \, cos(\theta_{sig} - \theta_{ref}) \tag{2.2}$$

Schematically Lock-In amplification is presented in the ***Fig. 12***. Input signal $V_s(t)$ divides into two components X and Y. Then each of them multiplies with reference and pass through (LP) filter.

LP filter rejects the noise and the second harmonic of the output signal. Components of the output signal are possible to convert to the polar coordinates.

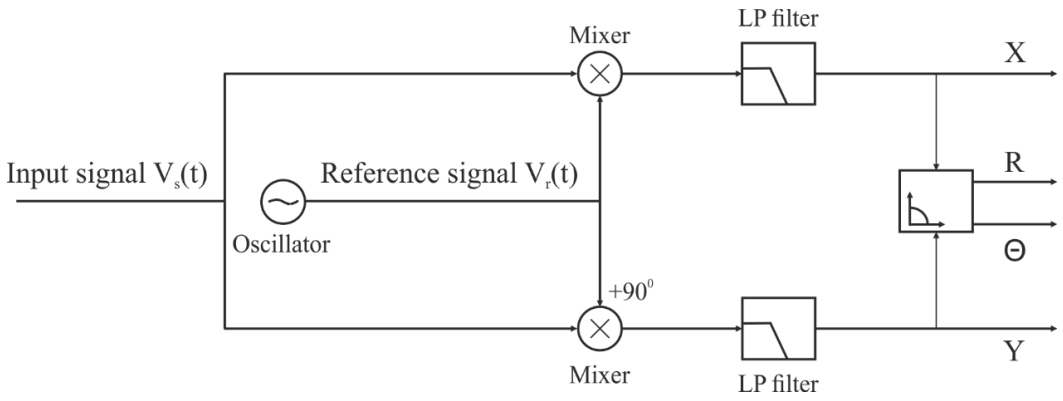

Fig. 12 *Schematic of Lock-In amplification.*

Chapter 3

3 Magnetoresistance measurements of GaAs QW

This section has the aim to describe MT of 2D structures with two patterns used in the experiments. We studied different devices in the experiments with two structure patterns. First was the commonly called Hall bar pattern to perform local and non-local measurements. Second was the H bar pattern that mostly used to measure non-local transport.

The samples we studied have the high electron density $n_s \approx 10^{12}\mathrm{cm}^{-2}$ and mobility $\mu \approx 2.5 \times 10^6\ \mathrm{cm}^2/\mathrm{V\ s}$. I helped to develop a numerical simulation tools to analyze experimental results related to dynamics in 2DES under MW excitation. First, I simulated ballistic transport in studied samples. Ballistic transport occurs when the electron mean free path is bigger than sample dimensions. Second, the electron transport was simulated at hydrodynamic regime. One of the way to achieve this regime is to create 2DES with high electron density. This contributes to the fact that electrons interact between each other. Finally, the comparison between simulations of two models with experimental results are presented.

3.1 Ballistic regime in GaAs QW

The ballistic regime occurs when the mean free path between electron-electron collisions l_{ee} is much longer than the sample width W. In other words, electrons don't interact between them and/or with impurities. In this situation, geometry defines transport properties (***Fig. 13***).

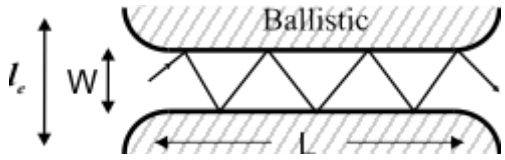

Fig. 13 *Schematically representation of ballistic transport in a sample channel.*

In the ballistic regime, electron transport through a 2D sample occurs without scattering from defects in the crystal cell, at the interface, or in self-scattering. This regime was described by Shepelianskii's model [31]. The starting point was Newton's equation, which took into account the reflection from the walls of sample, MW electric field interaction, and Lorentz force:

$$\vec{F} = -k\Delta\vec{r} + e\vec{E}\,cos(\omega t) + e[\vec{v} \times \vec{B}]. \qquad (3.1)$$

The next step was to solve Newton's equation:

$$m\frac{d\vec{v}}{dt} = -k\Delta\vec{r} + e\vec{E}\,cos(\omega t) + e[\vec{v}\times\vec{\omega}_c]\frac{m}{e},$$

where $\vec{\omega}_{\mathrm{c}} = \vec{\mathrm{B}}\frac{e}{\mathrm{m}}$ is the cyclotron motion and $-k\Delta\vec{r}$ is the soft wall potential. I simplified Newton's equation and it came to the following form:

$$\frac{d\vec{v}}{dt} = -\frac{k}{m}\Delta\vec{r} + \frac{e\vec{E}\,cos(\omega t)}{m} + [\vec{v}\times\vec{\omega}_c]. \tag{3.2}$$

After some mathematical procedures, the ***eq. (3.2)*** became similar to the equation from [31]. I used this equation in the numerical calculations. However, it was important to simplify the equation for use in numerical simulations. First, velocity in the ***eq. (3.2)*** was normalized by v_F to obtain dimensionless velocity $\vec{\mathrm{V}} = \frac{\vec{\mathrm{v}}}{v_F}$ and introduced new quantity for $\vec{\epsilon}$:

$$\frac{d\vec{V}}{dt} = -\frac{k}{mv_F}\Delta\vec{r} + \vec{\epsilon}\omega cos(\omega t) + [\vec{V}\times\vec{\omega}_c], \tag{3.3}$$

where $\vec{\epsilon}\omega = \frac{\vec{E}e}{\mathrm{m}v_F}$.

To simplify simulations of the ***eq. (3.3)*** some new variables were introduced: $T = \frac{t}{C} \rightarrow \Omega = \omega C$.

$$\frac{d\vec{V}}{CdT} = -\frac{k}{mv_F}\Delta\vec{r} + \vec{\epsilon}\omega cos(\Omega T) + [\vec{V}\times\vec{\omega}_c],$$

Finally, ***eq. (3.3)*** in new variables has the following form:

$$\frac{d\vec{V}}{dT} = -\frac{kC}{mv_F}\Delta\vec{r} + \vec{\epsilon}\Omega\,cos(\Omega T) + [\vec{V}\times\vec{\Omega}_c], \tag{3.4}$$

where $\vec{\epsilon}\Omega = \frac{\mathrm{Ce}\vec{E}}{\mathrm{m}v_F}$ and $\vec{\mathrm{V}}$ measures in a units of the Fermi velocity. $C = 10^{-11}$ is the normalization coefficient that was chosen to scale a time.

The normalized velocity can be expressed thought derivative of position vector:

$$\frac{d\vec{V}}{dT} = \frac{d}{dT}\frac{\vec{v}}{v_F} = \frac{d}{v_F dT}\frac{d\vec{r}}{dt} = \frac{d^2}{Cv_F dT^2}\vec{r} = \frac{d^2}{dT^2}\vec{R}, \tag{3.5}$$

where $\vec{\mathrm{R}} = \frac{\vec{\mathrm{r}}}{Cv_F}$.

Transformation of $\vec{V}$ has the following form:

$$\vec{V} = \frac{\vec{v}}{v_F} = \frac{d\vec{r}}{v_F dt} = \frac{Cd\vec{R}}{dt} = \frac{Cd\vec{R}}{CdT} = \frac{d\vec{R}}{dT}. \tag{3.6}$$

After all of these transformations, the final equation for numerical simulations is:

$$\frac{d^2}{dT^2}\vec{R} = -\frac{kC^2}{m}\Delta\vec{R} + \vec{\epsilon}\Omega\, cos(\Omega T) + [\frac{d\vec{R}}{dT} \times \vec{\Omega}_c]. \tag{3.7}$$

Fermi velocity in the samples was estimated using the following expression for $v_F = \frac{\hbar k_F}{m}$, where for 2DEG $k_F = (2\pi n)^{\frac{1}{2}}$, [32].

For the ballistic model, the shape of the wall potential is considered to be parabolic. The potential is estimated to be steepness from the assumption that the width of the region where the potential increases from the bottom to the Fermi energy has of the same order as the Fermi wavelength for typical electron concentrations. Assuming confinement edge potential $U = \frac{kx^2}{2}$ (for coordinates outside the Hall bar geometry), k is igual $0{,}008 meV/A^2$.

The theoretical model to calculate conductance was based on work of Landauer and Büttiker [40]. Following it, the generalized formula of conductance has the following form:

$$G = \left(\frac{e^2}{\pi h}\right)\frac{T}{R}, \tag{3.8}$$

where *T* and *R* are transmission and refraction coefficients respectively.

First, start with the simplest case of a single channel. Current $\vec{I}$ injects into the lead 1.

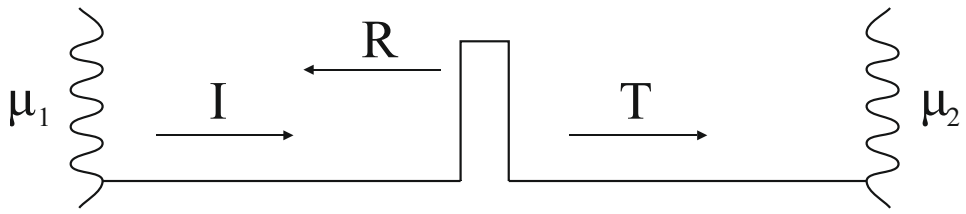

Fig. 14 *Single channel transmission*

So, injected current into the lead 1 is $\mathrm{I}_1 = ev_\mathrm{F}\left(\frac{dn_1}{dE}\right)\mu_1$, where v_F is the velocity at the Fermi level and $\frac{dn_1}{dE} = \frac{1}{2\pi\hbar v_\mathrm{F}}$. Thus $\mathrm{I}_1 = \frac{e}{h}(\mu_1 - \mathrm{T}_{12}\mu_2)$ is the current injected into the lead 1 and T_{21} is the transmission probability. Generalized formula for single channel has the following form:

$$I_{dc_i} = \frac{e}{h}(\mu_i - T_{ij}\mu_j). \tag{3.9}$$

Now it is possible to write the equation for current I_{dc} into the lead i. For the H-Shape structure, I used the formula for 4 terminals from the work of Buttiker [41], which later Beenakker [62] used for 6 terminals:

$$I_{dc_i} = \frac{e}{h}\left[(1 - R_{ii})\mu_i - \sum_{j\neq i} T_{ij}\mu_j\right], \tag{3.10}$$

where T_{ij} is a probability for carriers incident in lead j to be transmitted into lead i; R_{jj} is a probability for carrier incident in lead j to be reflected back in the same lead.

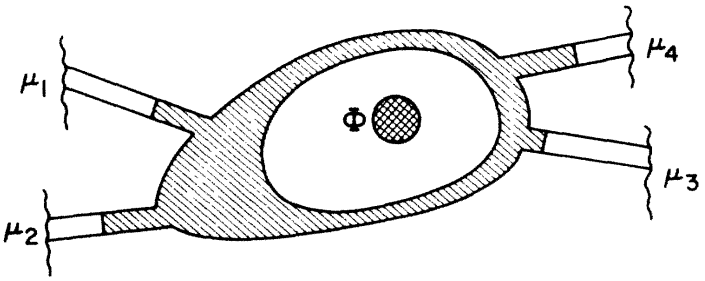

Fig. 15 *H Shape geometry presented in original Buttiker paper [40]*

Potential measured in the experiment is $V = \mu/e$, thus the equation for current can be modified as:

$$I_{dc_i} = \frac{e^2}{h}\left[(1 - R_{ii})V_i - \sum_{j\neq i} T_{ij}V_j\right]. \tag{3.11}$$

In H bar geometry for currents is possible to write the following expressions:

$$I_1 = \frac{e^2}{h}[(1 - R_{11})V_1 - (T_{12}V_2 + T_{13}V_3 + T_{14}V_4)]$$

$$I_2 = \frac{e^2}{h}[(1 - R_{22})V_2 - (T_{21}V_1 + T_{23}V_3 + T_{24}V_4)]$$

$$I_1 = -I_3$$

$$I_2 = -I_4,$$

where $I_1 = -I_3$ and $I_2 = -I_4$. After analytical calculations [41] for any 4 terminal geometry resistance is given by the following expression:

$$\mathcal{R}_{mn,kl} = \frac{h}{e^2}\frac{(T_{km}T_{ln} - T_{kn}T_{lm})}{D} \tag{3.12}$$

For local and non-local resistances in the experiment with H bar geometry the local and non-local resistances can be written as:

$$\mathcal{R}_L = \mathcal{R}_{21,34} = \frac{h}{e^2}\frac{(T_{32}T_{41} - T_{31}T_{42})}{D}, \mathcal{R}_{NL} = \mathcal{R}_{41,32} = \frac{h}{e^2}\frac{(T_{34}T_{21} - T_{31}T_{24})}{D},$$

where D has the following form:

$$\begin{gathered}
\mathrm{D} = \left(\frac{\mathrm{h}}{\mathrm{e}^2}\right)^2 (\alpha_{11}\alpha_{22} - \alpha_{12}\alpha_{21})\mathrm{S} \\
\alpha_{11} = \left(\frac{h}{e^2}\right)^{-1} [(1 - T_{11})S - (T_{32} + T_{12})(T_{41} + T_{21})]/S \\
\alpha_{22} = \left(\frac{h}{e^2}\right)^{-1} [(1 - T_{22})S - (T_{21} + T_{41})(T_{32} + T_{12})]/S \\
\alpha_{12} = \left(\frac{h}{e^2}\right)^{-1} [T_{12}T_{12} - T_{32}T_{32}]/S \\
\alpha_{21} = \left(\frac{h}{e^2}\right)^{-1} [T_{21}T_{21} - T_{41}T_{41}]/S \\
S = 2(T_{12} + T_{32})
\end{gathered} \tag{3.13}$$

In the matrix form after symmetrization the transmission matrix [see **Appendix I**] has the following form:

$$T = \begin{bmatrix} T_{11} & T_{12} & T_{31} & T_{32} \\ T_{21} & T_{22} & T_{41} & T_{42} \\ T_{31} & T_{32} & T_{11} & T_{12} \\ T_{41} & T_{42} & T_{21} & T_{22} \end{bmatrix} \tag{3.14}$$

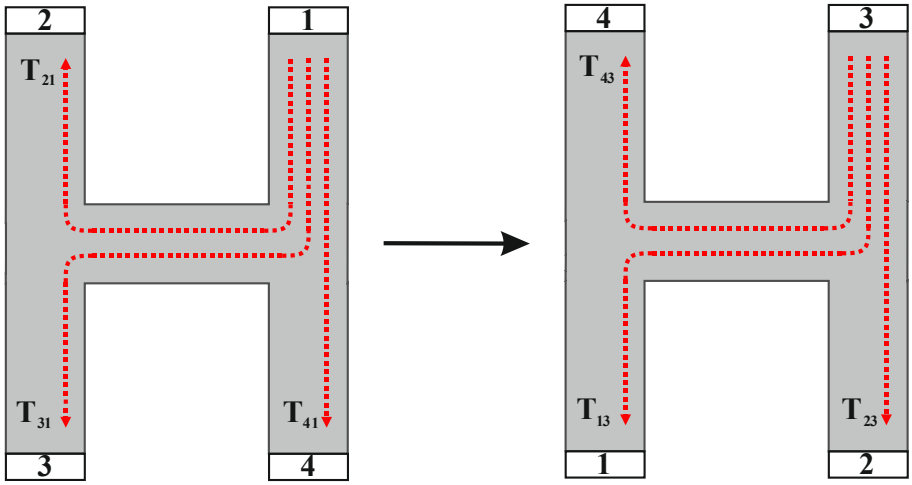

Fig. 16 *Rotational symmetry for H bar pattern.*

For the Hall bar geometry with 6 contacts, by using the same approach as for H bar geometry, currents are possible to write as follows:

$$I_1 = \frac{e^2}{h}[(1 - R_{11})V_1 - (T_{12}V_2 + T_{13}V_3 + T_{14}V_4 + T_{15}V_5 + T_{16}V_6)]$$

$$I_2 = \frac{e^2}{h}[(1 - R_{22})V_2 - (T_{21}V_1 + T_{23}V_3 + T_{24}V_4 + T_{25}V_5 + T_{26}V_6)]$$

$$I_3 = \frac{e^2}{h}[(1 - R_{33})V_3 - (T_{31}V_1 + T_{32}V_2 + T_{34}V_4 + T_{35}V_5 + T_{36}V_6)]$$

$$I_1 = -I_4$$

$$I_2 = -I_5$$

$$I_3 = -I_6,$$

where $I_1 = -I_4$, $I_2 = -I_5$ and $I_3 = -I_6$ by symmetry.

Hall bar geometry was treated extensively in Beenakker paper. I kept terminal numbering consistent with Beenakker's work [62]. Buttiker system of equations [41] can be written as in matrix form as:

$$I_{dc} = \frac{e^2}{h}SV, \text{ where} \qquad (3.15)$$

$$I_{dc} = \begin{pmatrix} I_{dc_1} \\ \vdots \\ I_{dc_n} \end{pmatrix}, V = \begin{pmatrix} V_1 \\ \vdots \\ V_n \end{pmatrix}, S = \mathbb{I} - T, T = \begin{pmatrix} T_{11} & \cdots & T_{1m} \\ \vdots & \ddots & \vdots \\ T_{n1} & \cdots & T_{nm} \end{pmatrix}$$

To calculate resistance between terminals k and l (see ***eq. (3.12)***), in case of current leaving terminal m and entering terminal n ($I_m = -I_n$, electrons are injected in n and are transmitted in all the other terminals) the following expression procedure was used:

1. Define current vector as 1 in position m and -1 in position n, the rest of elements are zeros.

$$I_{dc} = (0, \dots, 1, \dots, 0, \dots, -1, \dots, 0)^T.$$

2. Solve the equation in matrix form

$$I_{dc} = \frac{e^2}{h} SV.$$

3. Calculate

$$\mathcal{R}_{mn,kl} = V_k - V_l.$$

In particular, for comparison with published results and experiments, I focused on the following cases:

$$I_{dc}(1) = 1, I_{dc}(2) = -1, \mathcal{R}_{12,53} = V_5 - V_3$$

$$I_{dc}(2) = 1, I_{dc}(5) = -1, \mathcal{R}_{25,16} = V_1 - V_6$$

$$I_{dc}(4) = 1, I_{dc}(6) = -1, \mathcal{R}_{46,31} = V_1 - V_3$$

$$I_{dc}(6) = 1, I_{dc}(3) = -1, \mathcal{R}_{63,41} = V_4 - V_1$$

If suppose what electrons are injected into terminal 2. Using symmetry [see Appendix I]:

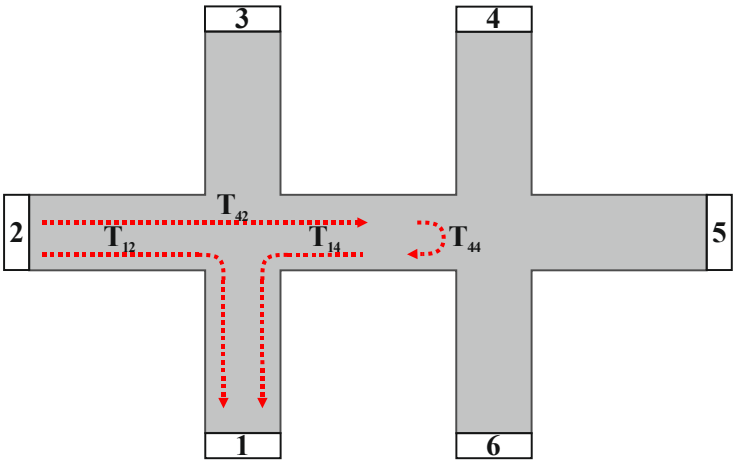

Fig. 17 *Hall-bar with 6 leads*

Based on this approach it is possible to determine transition for a long structure with two cross-sections depicted in the figure. The product of probabilities to pass through two cross-sections can be used. Also, it is nesessary to take into account probability of being reflected by neighbor cross section.

For the symmetry consideration, a complete transmission matrix has the following form:

$$\mathrm{T6} = \begin{bmatrix} T6_{11} & T6_{12} & T6_{13} & T6_{14} & T6_{15} & T6_{16} \\ T6_{21} & T6_{22} & T6_{23} & T6_{24} & T6_{25} & T6_{26} \\ T6_{31} & T6_{32} & T6_{33} & T6_{34} & T6_{35} & T6_{36} \\ T6_{41} & T6_{42} & T6_{43} & T6_{44} & T6_{45} & T6_{46} \\ T6_{51} & T6_{52} & T6_{53} & T6_{54} & T6_{55} & T6_{56} \\ T6_{61} & T6_{62} & T6_{63} & T6_{64} & T6_{65} & T6_{66} \end{bmatrix}$$

Carriers injected into terminal 1

$$T6_{11} = T_{22} + T_{41}T_{22}T_{14}, \qquad T6_{21} = T_{21} + T_{41}T_{22}T_{24}, \qquad T6_{31} = T_{31} + T_{41}T_{22}T_{34},$$

$$T6_{41} = T_{41}T_{32}, \qquad T6_{51} = T_{41}T_{42}, \qquad T6_{61} = T_{41}T_{12},$$

Carriers injected into terminal 2

$$T6_{12} = T_{12} + T_{42}T_{22}T_{14}, \qquad T6_{22} = T_{22} + T_{42}T_{22}T_{24}, \qquad T6_{32} = T_{32} + T_{42}T_{22}T_{34},$$

$$T6_{42} = T_{42}T_{32}, \qquad T6_{52} = T_{42}T_{42}, \qquad T6_{62} = T_{42}T_{12},$$

Carriers injected into terminal 3

$$T6_{13} = T_{13} + T_{43}T_{22}T_{14}, \qquad T6_{23} = T_{23} + T_{43}T_{22}T_{24}, \qquad T6_{33} = T_{22} + T_{43}T_{22}T_{34},$$

$$T6_{43} = T_{43}T_{32}, \qquad T6_{53} = T_{43}T_{42}, \qquad T6_{63} = T_{43}T_{12},$$

Carriers injected into terminal 4

$$T6_{14} = T_{23}T_{14}, \qquad T6_{24} = T_{23}T_{24}, \qquad T6_{34} = T_{23}T_{34},$$

$$T6_{44} = T_{22} + T_{23}T_{22}T_{32}, \qquad T6_{54} = T_{43} + T_{23}T_{22}T_{42}, \qquad T6_{64} = T_{13} + T_{23}T_{22}T_{12},$$

Carriers injected into terminal 5

$$T6_{15} = T_{24}T_{14}, \qquad T6_{25} = T_{24}T_{24}, \qquad T6_{35} = T_{24}T_{34},$$

$$T6_{45} = T_{34} + T_{24}T_{22}T_{32}, \qquad T6_{55} = T_{22} + T_{24}T_{22}T_{42}, \qquad T6_{65} = T_{14} + T_{24}T_{22}T_{12},$$

Carriers injected into terminal 6

$$T6_{16} = T_{21}T_{14}, \qquad T6_{26} = T_{21}T_{24}, \qquad T6_{36} = T_{21}T_{34},$$

$$T6_{46} = T_{31} + T_{21}T_{22}T_{32}, \qquad T6_{56} = T_{41} + T_{21}T_{22}T_{42}, \qquad T6_{66} = T_{22} + T_{21}T_{22}T_{12}$$

3.2 Physical parameters for simulations

In the simulations, I used the following physical parameters:

$$m_0 = 9.1 \times 10^{-31}(kg), m = 0.065m_0(kg), n = 10^{12}(cm^{-2}) \qquad (3.16)$$

Fermi velocity in the samples was estimated from the following expression:

$$v_F = \frac{\hbar k_F}{m}, \qquad (3.17)$$

where $\hbar$ is Planck constant, m is the effective mass of electron and k_F is Fermi constant. For the 2DES Fermi constant has the following form $k_F = (2\pi n)^{\frac{1}{2}}$ [32]. Thus, after put the physical parameters from ***eq. 3.16*** into the expression for Fermi velocity ***(3.17)***, it can be expressed as:

$$v_F = \frac{1.1\times10^{-34}\cdot(2\cdot3.14\times10^{16})^{\frac{1}{2}}}{0.065\cdot9.1\times10^{-31}} \approx 4{,}5 \cdot 10^5(^m/_S). \qquad (3.18)$$

To estimate soft wall parabolic potential it was assumed that electrons with Fermi energy are able to approach the edge of the sample to around d = 0.37μm, then k was calculated as:

$$k = \frac{2E_F}{d^2}, \frac{kC^2}{m} = 146s^{-2}.$$

To verify that the simulations were correct, the results obtained for Hall geometry were compared with those published by Beenakker. Good agreement in the shape of curves was found. In the ***Fig. 18*** is presented a comparison with Beenaker's calculations for several geometrical parameters.

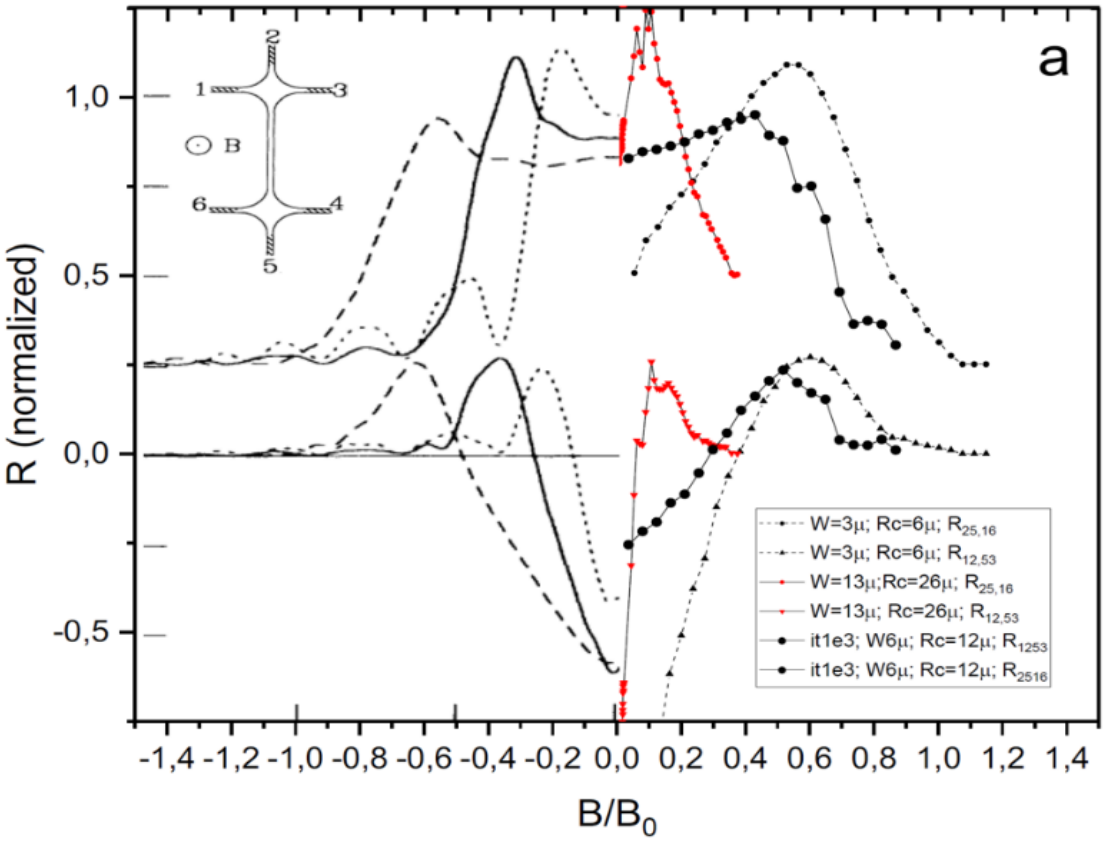

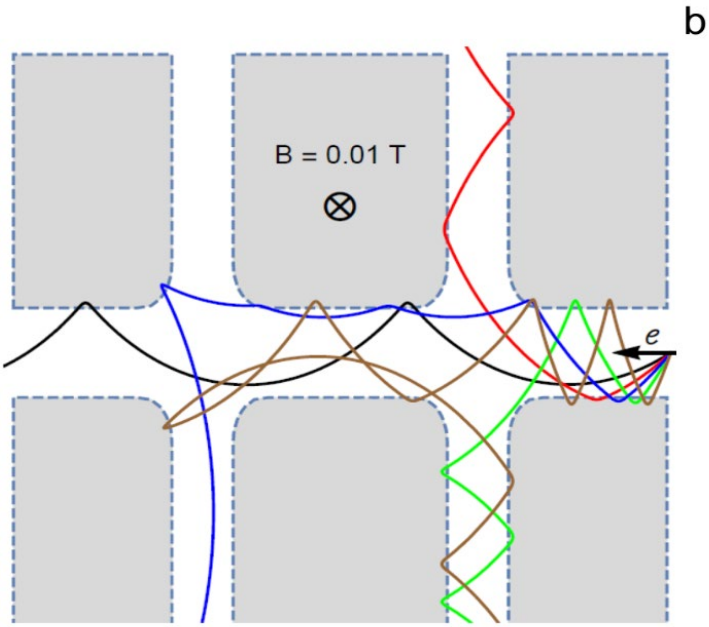

Fig. 18 *(a) Comparison of local and non-local resistances calculated for several dimentions of a Hall bar. The negative magnetic field has curves published by Beenakker. Positive magnetic field has simulated results. (b) Examples of electron trajectories inside Hall bar presented for five different injection angles. Electrons are injected from the right lead with Fermi velocity* $v_F = 4{,}1 \times 10^5 \mathrm{m/s}$*, magnetic field is maintained fixed at* $B = 0.01T$*. Gray areas are Hall bar walls modeled as repulsive parabolic potential for electrons.*

3.3 Comparison of the ballistic model with experiment

The next step was to compare experiment with theory. we measured the longitudinal and nonlocal resistance of samples with an H-shaped pattern at low temperatures. In measurements, we used the generally accepted Lock-In measuring technique. The results are presented in the figures below.

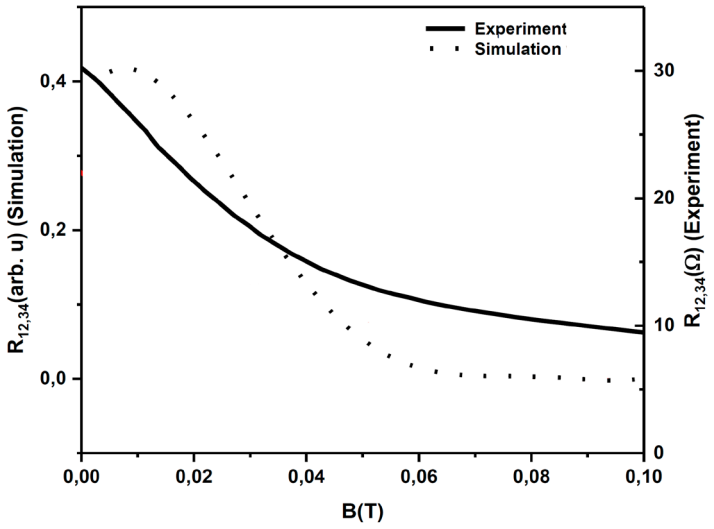

Fig. 19 *Comparison of local resistance for the H bar structure with numerical simulations (dashed).*

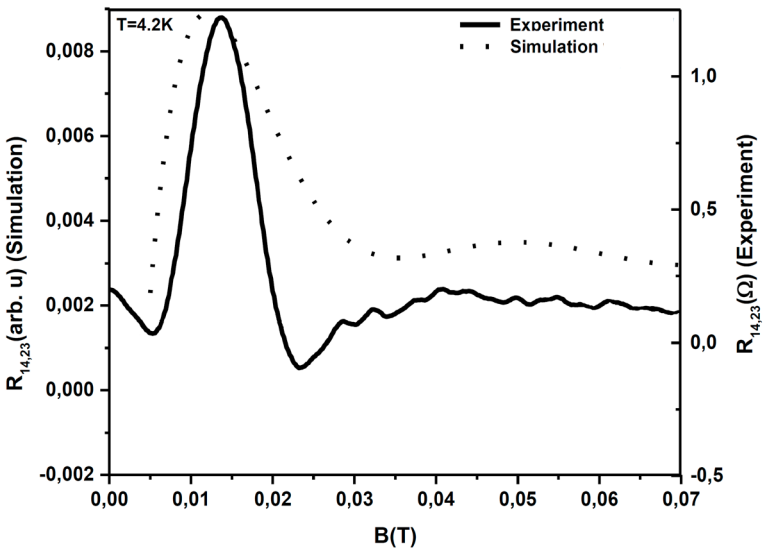

Fig. 20 *Comparison of non local resistance for the H bar structure with numerical simulations (dashed).*

As possible to see the ballistic model can be useful as a first approximation. Therefore this theory can't reproduce maxima or minima close to the zero magnetic field. This indicates that

the samples we studied had more complex electron dynamics. Thus was taken a decision to try to explain effects in the sample by using other theory. It was supposed that due to big electron density and high electron mobility the electrons in the samples can act like a viscous flow. This means that hydrodynamic model may be applied.

3.4 Temperature dependence

Before explaining the theoretical model and the results of the experiments, I want to present some configurations of measurements that were used in the experiment. Configurations are presented in the ***Fig. 21***. The four terminal, H bar pattern consists of a 4 μm width central channel located between 5μm wide legs. The 8 terminal Hall bar pattern consists of three, 5μm wide consecutive segments of different length (10, 20, 10μm). Also, it is possible to see a different connection scheme to the Hall bar patterned samples. The first type of measurement was performed for local configurations.

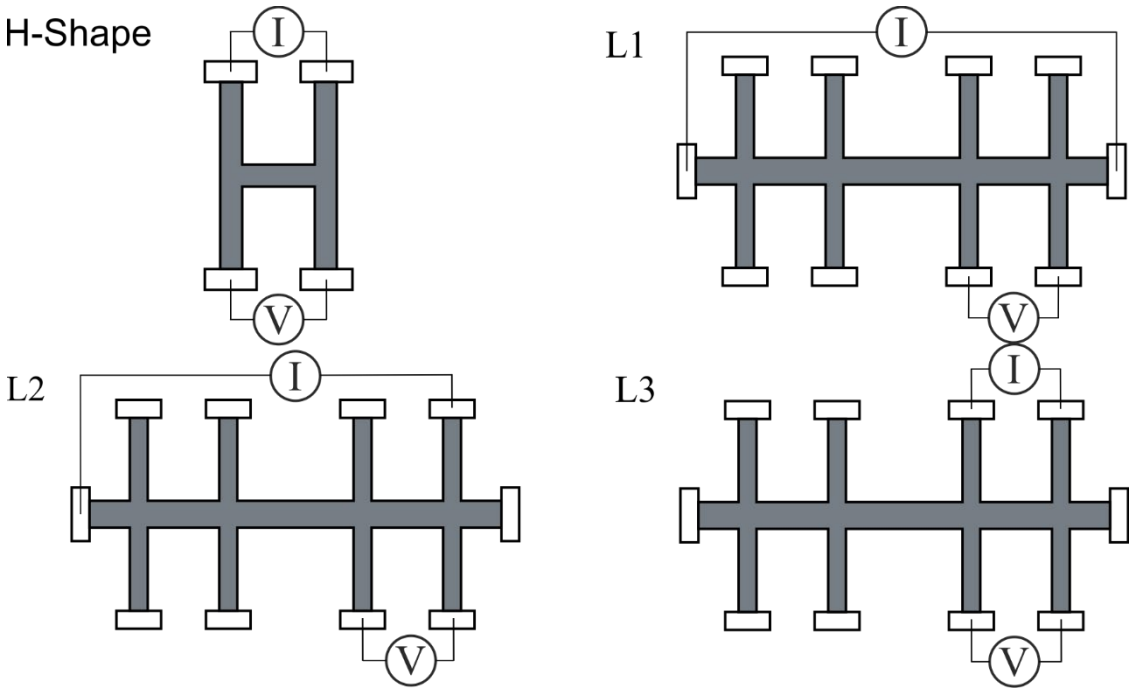

Fig. 21 *Different measurement configurations for H bar geometry, conventional (L1) and modified (L2, L3) configurations for Hall bar geometry.*

The ballistic contribution to electron transport depends on the temperature due to the thermal broadening of the Fermi distribution function and scattering by the phonons. A rough estimate of the nonlocal ballistic resistance may be obtained using the formula $R_{NL} \sim exp(-L/l)$, where

L is the distance between probes and mean free path $l = v_F\tau$ [33]. In experiments, a more complicated situation was observed. The electron-electron interaction was considered.

It is generally believed that, in the absence of disorder, a many-body electron system may resemble a viscous flow. Hydrodynamic characteristics can be specially enhanced in a pipe flow setup, where the mean free path for electron-electron collision l_{ee} is much shorter than the sample width W, while the mean free path due to impurity and phonon scattering l is larger than W. Viscosity is characterized by momentum relaxation in the fluid and, in marrow samples, occurs at the sample boundary. When fluid flows along a pipe, a quadratic velocity profile is formed, which leads to the Gurzhi effect ($\rho \sim T^{-2}$) [56, 57, 58] and can be detected from the anomalous temperature and sample width dependence, as is mentioned above. For illustration, we modeled the Poiseuille flow for a 2D neutral fluid.

Fig. 22 shows the longitudinal magnetoresistivity ρ_{xx} measured in local configuration for a H-bar sample as a function of magnetic field and temperature. It is possible to see two characteristic features: a giant negative magnetoresistance ($\sim$ 400−1000%) and a pronounced temperature dependence of the zero field resistance. In ***Fig. 23*** is presented the longitudinal magnetoresistivity ρ_{xx} measured in local configuration for a Hall-bar sample as a function of magnetic field and temperature. It is possible to see the same behavior of magnetoresistance ($\sim$ 400−1000%) and the temperature dependence of the zero field resistance. The magnetoresistance feature is qualitatively similar, although the decrease is not so rapid as in the H-bar.

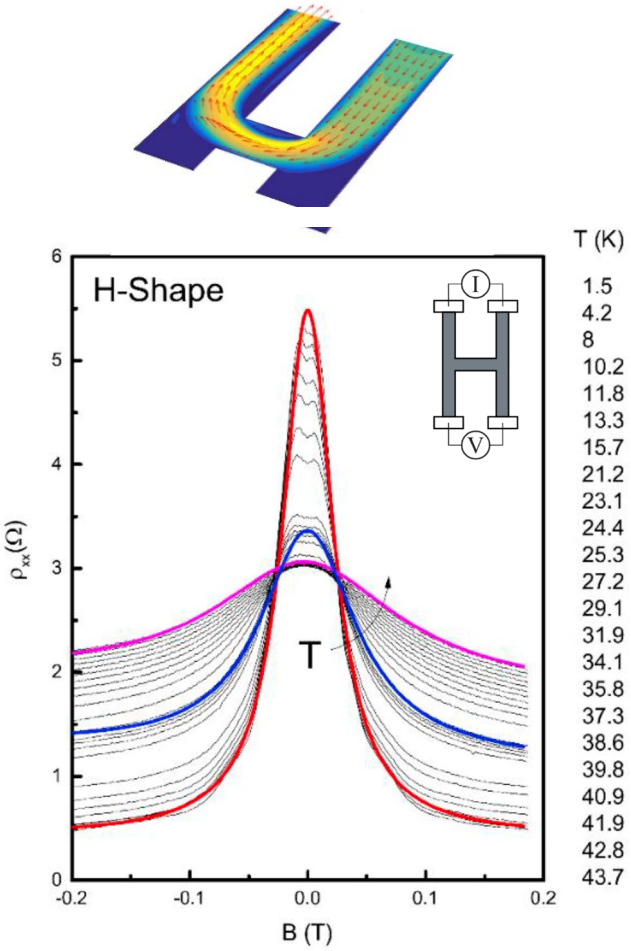

Fig. 22 *Top- a sketch of the velocity flow profile for viscous flow in the experimental set up used in this study. Temperature-dependent magnetoresistance of a GaAs quantum well in an H-bar sample. Thick curves are examples illustrating magnetoresistance calculated from theory (**eq. (3.22)**) for different temperatures: 1.5 K (red), 27.2 K(blue) and 43.7 K (magenta).*

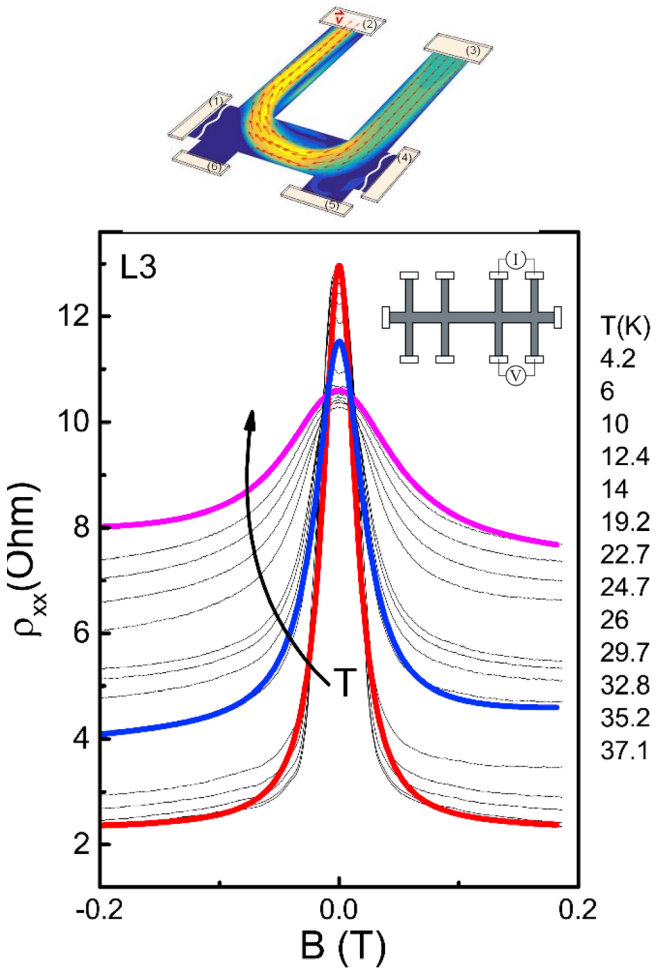

Fig. 23 *Top- a sketch of the velocity flow profile for viscous flow in the experimental set up used in this study. Temperature-dependent magnetoresistance of a GaAs quantum well in a Hall bar sample. Thick curves are examples illustrating magnetoresistance calculated from theory (**eq. (3.22)**) for different temperatures: 4.2 K (red), 19.2 K(blue) and 37.1 K(magenta).*

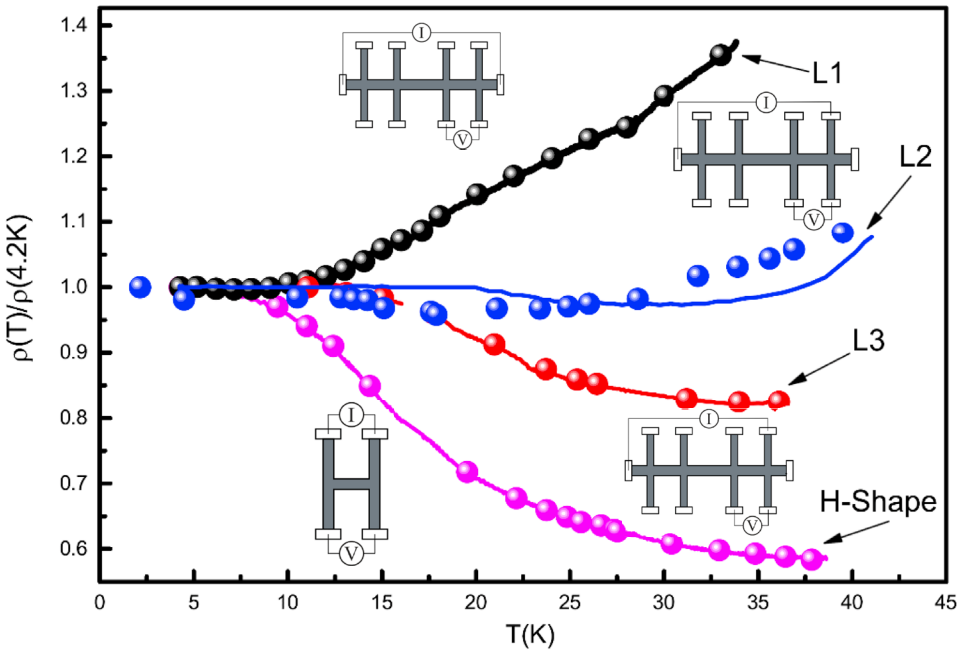

Fig. 24 *Temperature dependent resistivity of a GaAs quantum well in a Hall bar and H-bar for different configurations in zero magnetic field. Circles show calculations from the theory* ***(eq. (3.22))****.*

Im ***Fig. 24*** is presented the dependence of the normalized resistivity of GaAs for Hall bar and H bar samples for different configurations from the temperature at a zero magnetic field. It is possible to see that resistance in the L1 setup is increasing while the resistance for L3 and H-Shape setups is decreasing.

To observe the hydrodynamic effect and Hall viscosity in a 2D electron system and present experimental results, I participated in measurements of resistance in the Hall configuration. For this purpose, GaAs mesoscopic samples with high mobility 2D electron gas were used. In addition, the magnetoresistance measurements were performed in nonlocal and Hall configurations to characterize electron shear viscosity, electron-electron scattering time, and to reexamine electron transport over a certain temperature range of 1.5-40 K. We observed negative corrections to the Hall effect near zero magnetic fields, which can be attributed to classical Hall viscosity.

Hall resistance measurements were performed in two configurations. Conventional H1 configuration and modified configuration H2 (***Fig. 25***).

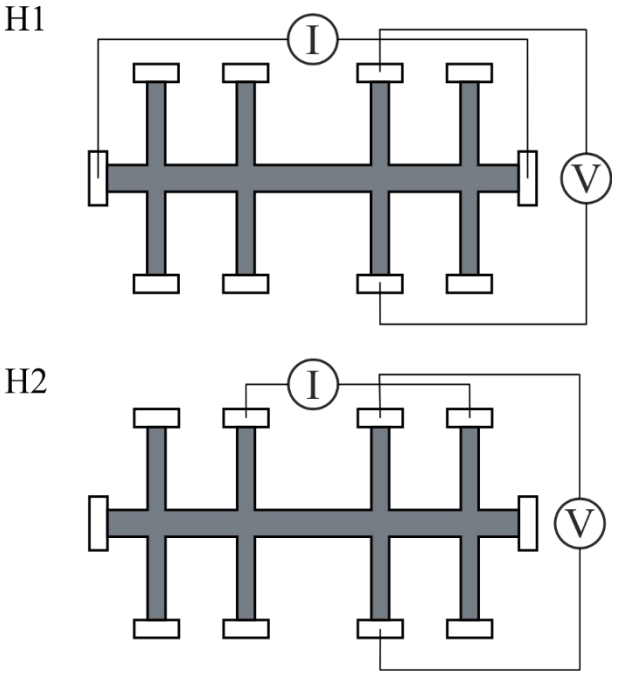

Fig. 25 *Conventional configuration (H1) and modified configuration (H2)*

Fig. 26 (a) shows deviations from Hall resistivity $\Delta\rho_{xy}(T) = \rho_{xy}(T) - \rho_{xy}^{bulk}$ as a function of temperature. ***Fig. 26 (b)*** shows the ratio $\Delta\rho_{\mathrm{xy}}(\mathrm{T})/\rho_{\mathrm{xy}}^{\mathrm{bulk}}$ for different temperatures. It is possible to see a strong (~ 10 - 20%) deviation from the linear slope. The slope is opposite to the bulk Hall slope at low fields and has the same sign (negative for electrons) at large positive magnetic field and low temperatures.

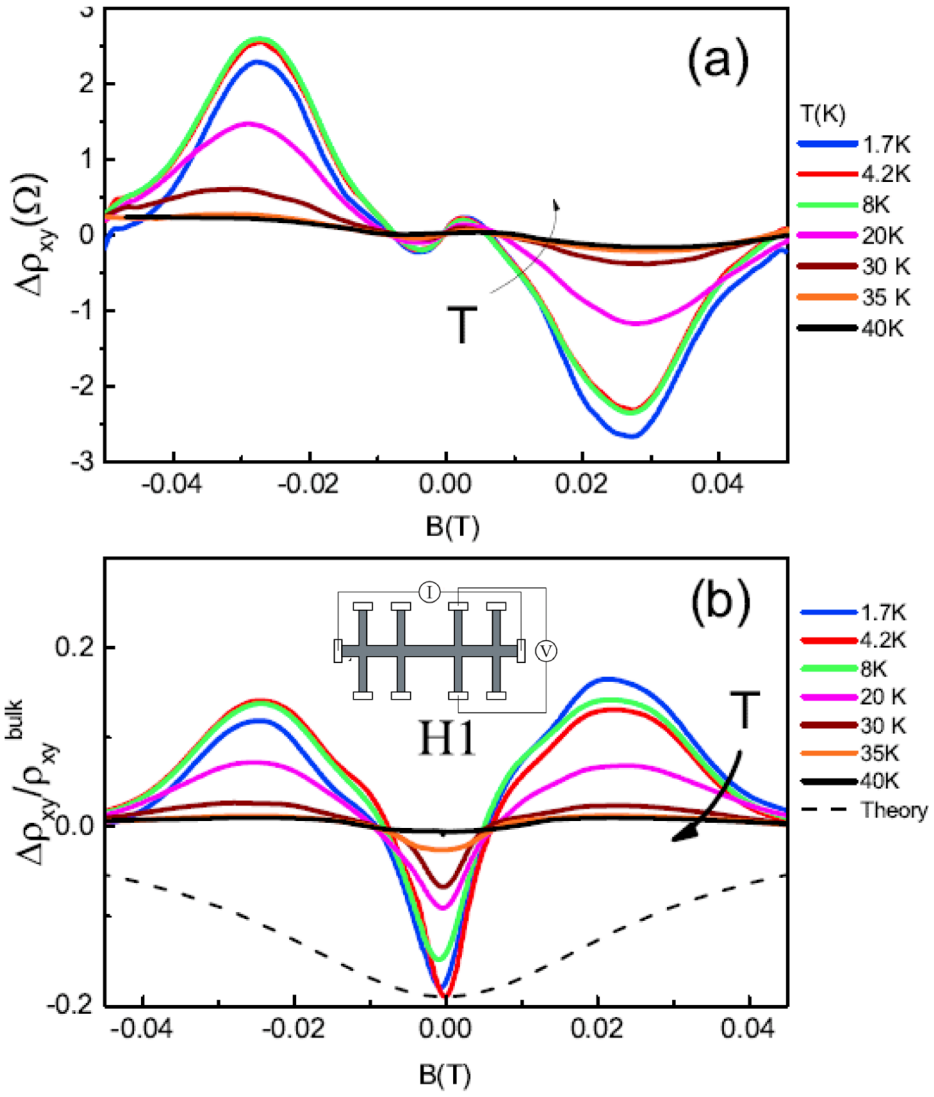

Fig. 26 *(a) Temperature dependentdeviations from the Hall resistivity* $\Delta\rho_{xy}(T)$ *of a mesoscopic GaAs sample. (b) The ratio* $\Delta\rho_{xy}(T)/\rho_{xy}^{bulk}$ *for different temperatures. Dashes line represents theory* ***(eq. (3.25))***.

In ***Fig. 27 (a)*** shows a comparison of Hall effect in the H1 configuration with the H2 configuration. It is possible to see that Hall resistivity is wider for the H2 configuration at low magnetic fields. Therefore, the ratio $\Delta\rho_{xy}(T)/\rho_{xy}^{bulk}$ has wide negative peak near the zero magnetic field. In ***Fig. 27 (b)*** shows the results of measurements in comparison with the hydrodynamic model. As possible to see, the H2 configuration has a wider negative peak around zero magnetic fields. This is explained by the fact that in the H2 configuration the hydrodynamic effect is manifested more strongly than in the H1 configuration. And the measurement results have better match for this configuration with the hydrodynamic model.

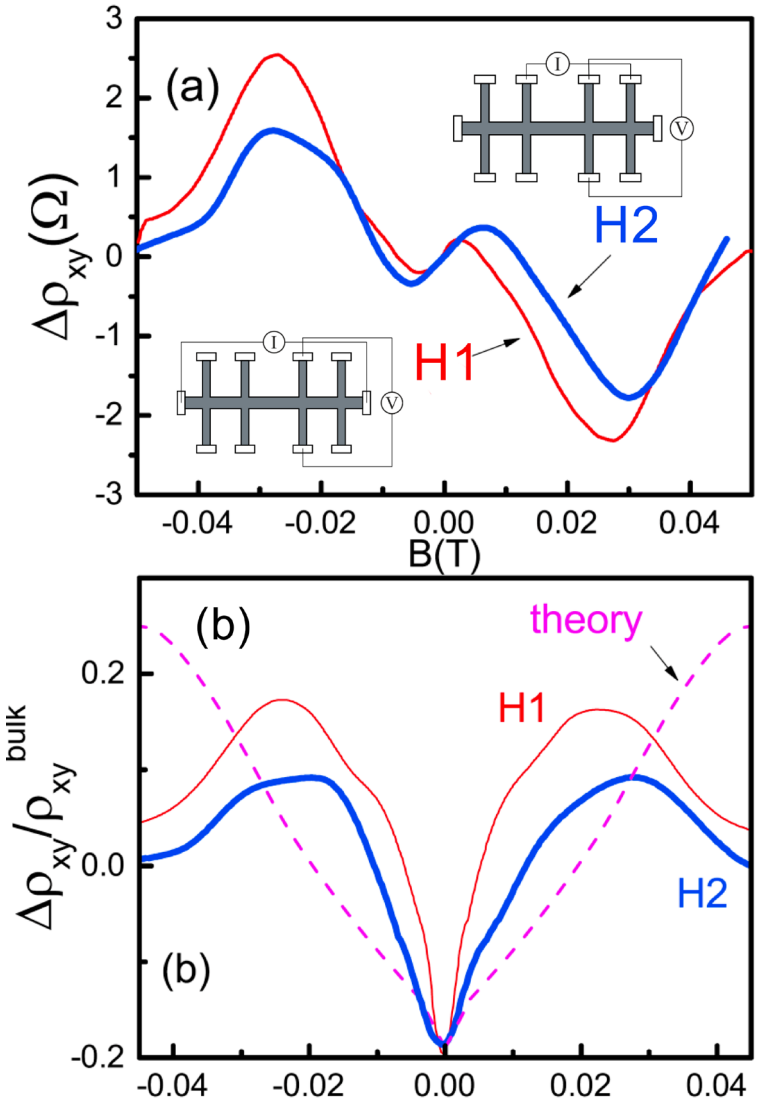

Fig. 27 *(a) The Hall effect for two configurations at T=4.2K. (b) The ratio* $\Delta\rho_{xy}(T)/\rho_{xy}^{bulk}$ *for configurations H1 and H2. Dashes line represents theoretical calculation* ***(eq. (3.25))***.

The third type of measurement was performed at a non-local configuration. For this case two different configurations were chosen.

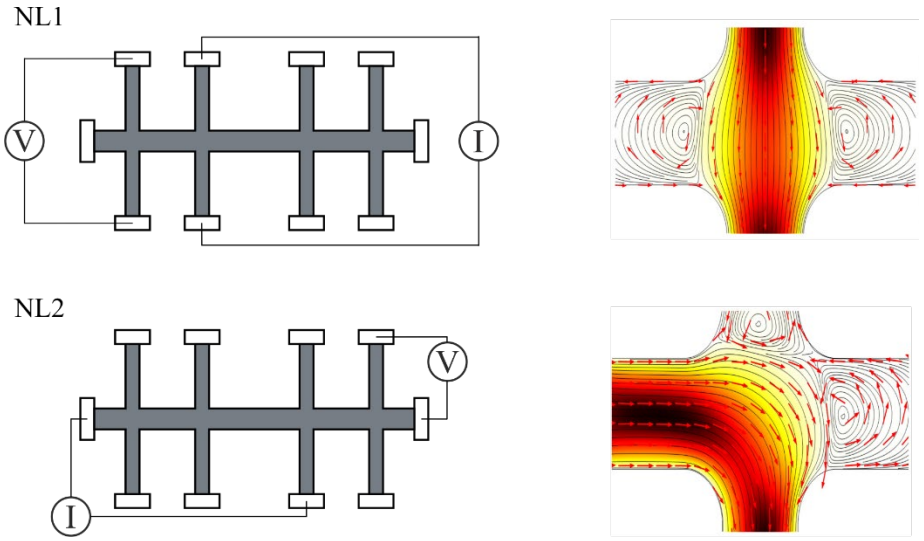

Fig. 28 *Configuration C1 and a sketch of the velocity flow profile (top) and configuration C2 and a sketch of the velocity flow profile (bottom).*

These configurations permit non-local measurements with the easier observation of current whirlpools. The NL1 transport measurement setup was proposed in [59]. The NL2 transport measurement setup, also known as “vicinity”, was proposed in [55 - 60].

First, the electron transport was measured in the NL1 configuration. (***Fig. 29)***.

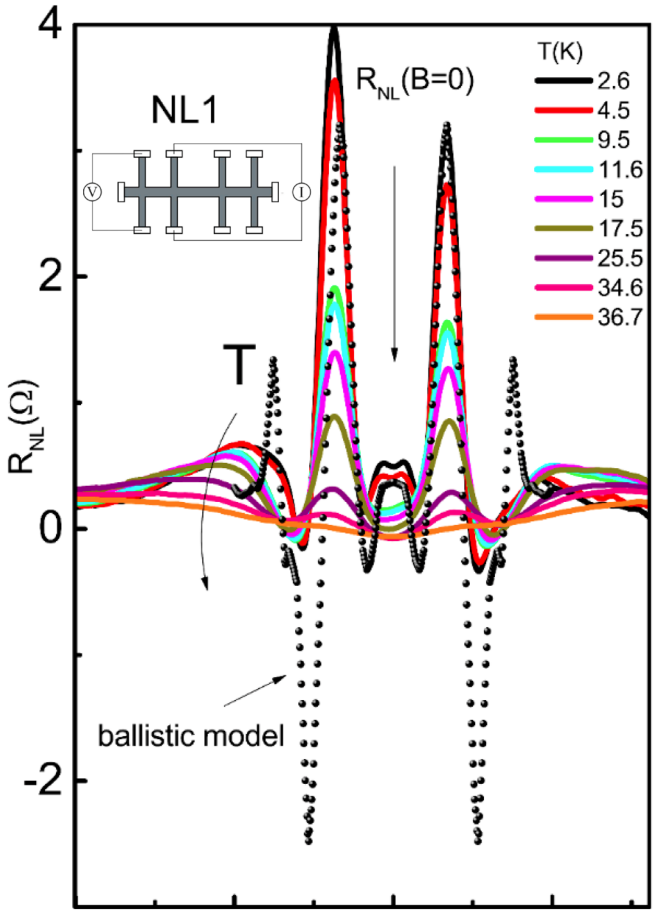

Fig. 29 *Non-local transport signal vc magnetic field for different temperatures. The dots represent result for the ballistic model.*

It is possible to see a strong oscillation in the weak magnetic fields due to geometrical resonance effects considered in the semiclassical billiard model. Numerical simulations have helped to better understand the results obtained experimentally. The results of these simulations (black dots) were compared to the experimental data. Agreement with experimental data was observed only at the low magnetic fields. Although, as it presented in ***Fig. 29***, the position of resistance peaks at higher magnetic field coincides with calculations, the negative peak has a much smaller value and the positive peak is wider than that obtained from the billiard model. ***Fig. 29*** also shows the evolution of the nonlocal magnetoresistance with temperature. All oscillations are smeared out by temperature and magnetoresistance at high temperature has a parabolic shape. Remarkably, the nonlocal resistance at $B = 0$ is positive at low temperatures, in accordance with the ballistic model calculations, and then it changes sign and becomes negative at higher temperatures.

Then, the non-local transport was measured in NL2 configuration. Thr result of the measurements ***(Fig. 30)*** was qualitatively different from the result of the measurements in NL1 configuration.

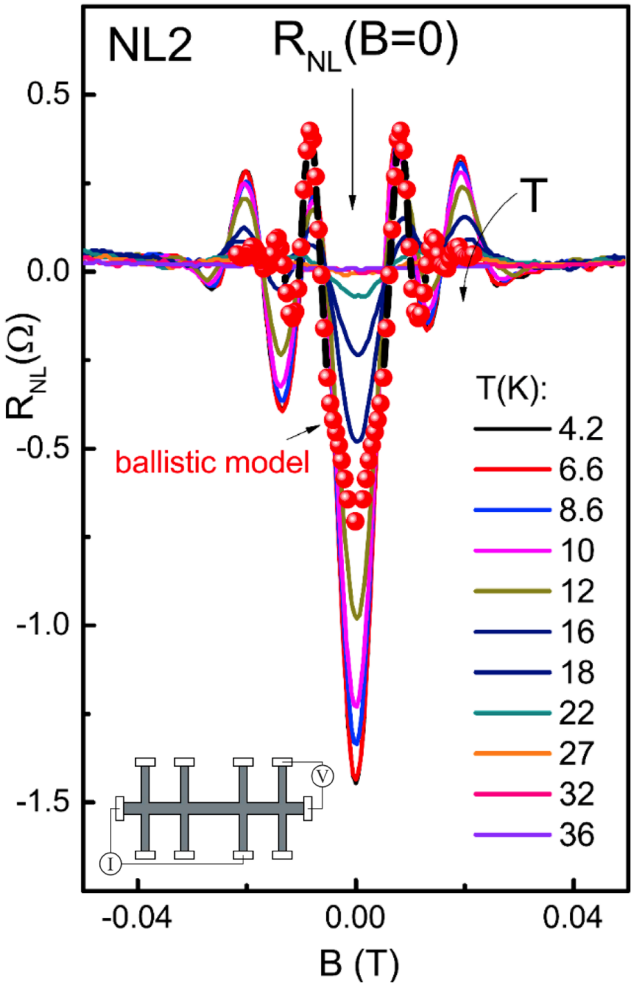

Fig. 30 *Non-local transport signal vc magnetic field for different temperatures. The dots represent result for the ballistic model.*

As in configuration NL1, configuration NL2 has strong oscillations due to the geometrical resonance effect. Note that the ballistic transport in this configuration is very well established and studied previously in numerous publications. In cross junction geometry, it was denominated as bend resistance. Also the classical simulations were performed for the transport in the NL2 configuration. However, that in contrast to configuration NL1, the bend resistance reveals a strong negative resistance peak near zero magnetic fields. This peak may mask the negative nonlocal signal due to viscosity, and a detailed comparison is required to examine the significance of the hydrodynamic effect at low and high temperatures.

3.5 Model for a hydrodynamic regime in 2DES

In the GaAs samples with high electron density $n_s \approx 10^{12}\text{cm}^{-2}$ it is possible to consider electrons like a viscous flow in so called hydrodynamic regime. Hydrodynamic regime is possible to reach when the mean free path of electron-electron collisions l_{ee} is much smaller than sample width W that leads to electron-electron interactions and interactions between electrons and impurities [42 - 49]. Also, if apply the magnetic field it is possible to consider that the hydrodynamic regime can be obtained with l_{ee} > W but cyclotron radius r_c need to be much smaller than sample width W. In this case, it is possible to use the Navier-Stokes hydrodynamic equation for an incompressible liquid to describe the processes observed in the samples (***eq. 1.9***).

The first assumption that the flow of electrons in the samples does not have a convective acceleration $(\vec{v}\cdot\nabla)\vec{v} = 0$ and the internal thermodynamic work $\nabla w = 0$. The force $\vec{g}$ here is the electromagnetic force which is equal $\vec{g} = e\vec{E} + e[\vec{v}\times\vec{B}]$. It is possible to rewrite ***eq. (1.9)*** in vector form as follows:

$$\frac{\partial\vec{v}}{\partial t} = \eta\nabla^2\vec{v} + \frac{e\vec{E}}{m} + \frac{e}{m}\left[\vec{v}\times\vec{B}\right], \tag{3.19}$$

where τ it is the momentum relaxation time due to interaction with defects and η is the electron viscosity tensor that has two components: symmetric $\eta_{ij}^{(s)} = \frac{1}{2}(\frac{\partial v_i}{\partial x_j} + \frac{\partial v_j}{\partial x_i})$ and antisymmetric $\eta_{ij}^{(a)} = \frac{1}{2}(\frac{\partial v_i}{\partial x_j} - \frac{\partial v_j}{\partial x_i})$.

It is necessary to solve ***eq. (3.19)*** in the stationary regime without applying external magnetic field [52, 54].

$$\eta\nabla^2\vec{v} + \frac{e\vec{E}}{m} = 0 \tag{3.20}$$

The hydrodynamic regime can be observed in the pipe flow setup. Thus the boundary conditions are the follows $v_i(x,y) = (v_x(y), 0)$ (if supposed that current flows in x direction). Then, the solution for velocity profile can be used ***(eq. 3.20)*** to write resistivity ρ:

$$\rho = \frac{m}{e^2 n\tau^*}, \tag{3.21}$$

where $\tau^* = \frac{W(W+6l_s)}{12\eta}$ is the effective relaxation time and $\eta = \frac{1}{4}v_F^2\tau_2$ is the diffusion constant, τ_2 is the electron-electron scattering time.

Solution of the ***eq. (3.20)*** can be modified if momentum relaxation time τ due to interaction with phonons and static defects is close to the τ^* [52, 53]. For this case in the ***eq. (3.20)*** is necessary to put additional bulk friction term $-v/\tau$. Therefore, for interpolation, it is possible to use formula, which gives an expression for resistance ρ for any value of τ/τ^*:

$$\rho = \rho_0(1 + \frac{\tau}{\tau^*}), \tag{3.22}$$

where $\rho_0 = \frac{m}{e^2 n\tau}$ is the bulk resistivity.

Next step is to solve ***eq. (3.19)*** in the presence of magnetic field. If rewrite ***eq. (3.19)*** by component representation, two additional parameters appear. The η_{xx} and η_{xy} which are regular and Hall components of the kinematic viscosity tensor:

$$\eta_{xx} = \frac{\eta}{1+(2\omega_c\tau_2)^2} \text{ and } \eta_{xy} = 2\omega_c\tau_2\eta_{xx}. \tag{3.23}$$

Also, incompressibility of the electron fluid was supposed, so $\mathrm{div}\vec{v} = 0$. Finally, the hydrodynamic equation in the stationary regime has the following form:

$$\eta_{xx}\frac{d^2v_x}{dy^2} + \frac{e}{m}E_x - \frac{v_x}{\tau} = 0 \text{ and } \eta_{xy}\frac{d^2v_x}{dy^2} + \omega_c v_x + \frac{e}{m}E_y = 0. \tag{3.24}$$

Now eq. ***(3.24)*** can be solved by applying the previous boundary conditions, which were used for the case with the absence of a magnetic field. The following solutions were used to compare theoretical calculations with experimental results [53]:

$$\rho_{xx} = \rho_0(1 + \frac{\tau}{\tau^*}\frac{1}{1+(2\omega_c\tau_2)^2}) \text{ and } \rho_{xy} = \rho_0(1 - r_H\frac{2\tau_2}{\tau^*}\frac{1}{1+(2\omega_c\tau_2)^2}), \tag{3.25}$$

where $\rho_0 = \frac{m}{ne^2\tau}$, τ is the momentum relaxation time due to interactions with defects, $\tau^* = \frac{W(W+6l_s)}{12\eta}$ is the effective relaxation time, τ_2 is the electron-electron scattering time and r_H is a numerical coefficient in order 1.

Resistance was also measured at the non-local and vicinity configurations. For the case of the non-local measurements resistance *R* has the following expression [61]:

$$R_{NL1} = -\rho_0 \left[\frac{ln\,(tanh^2(\bar{x}/2))}{\pi} + 4\pi(\frac{D_\eta}{W})^2 \frac{cosh\,(\bar{x})}{sinh^2(\bar{x})}\right], \qquad (3.26)$$

where $\bar{x} = {}^{\pi x}/_{W}$ is a distance from the main current path where negative non-local resistance can be observed [55 - 60] and $D_\eta = \sqrt{\eta\tau}$ is the vorticity diffusion length.

The expression for the non-local resistance in vicinity geometry [61] has the following form:

$$R_{NL2} = -\frac{\rho_0}{2}\left[\frac{ln\,(4sinh^2(\bar{x}/2))}{\pi} - \frac{\bar{x}}{W} + \pi(\frac{D_\eta}{W})^2 \frac{1}{sinh^2(\bar{x})}\right]. \qquad (3.27)$$

These results were used to compare with the experimentally obtained data and extract system physical parameters. In the figures below is presented the comparison between theory and experiment.

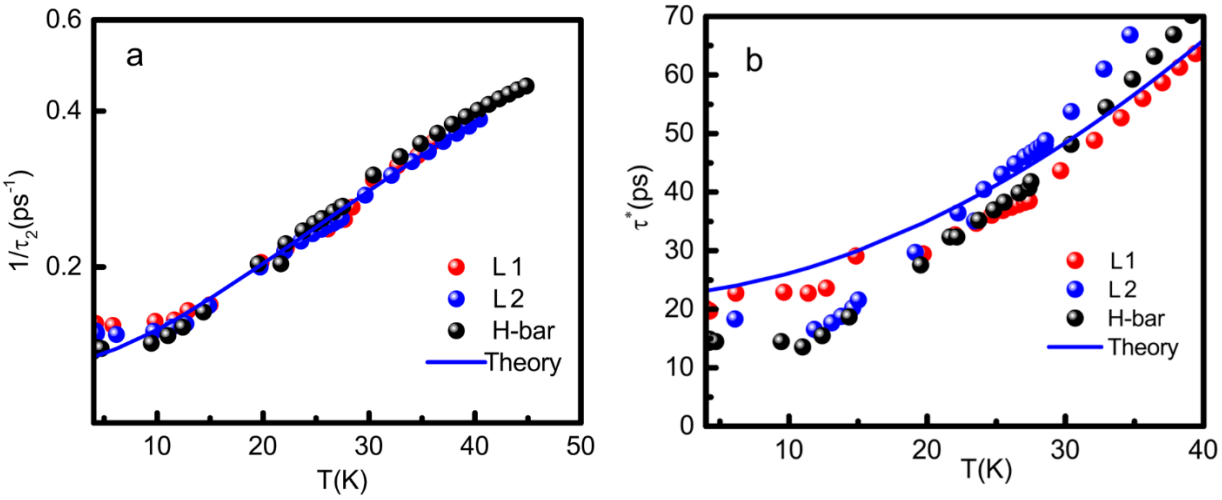

Fig. 31 *(a) The relaxation time τ_2 as a function of the temperature obtained by fitting the theory with experimental results. The solid line is theory. (b) The relaxation time τ^* as a function of the temperature obtained by fitting the theory with experimental results. The solid line is theory.*

The scattering time dependencies are presented in ***Fig. 31***. The effective relaxation time τ^* is proportional to the second moment relaxation rate $\frac{1}{\tau_2}$ (not a time) and can be also compared with the theory. It contains additional parameter - boundary slip length, which depends on the viscous flow conditions. It is possible to reproduce the evolution of characteristic time with temperature in the experimets, assuming that l_s depends on probe configuration. Some

simulations were done with modelling of the Poiseuille flow for two dimensional situations depicted in ***Fig. 22*** and ***Fig. 23***. It is possible to see that the velocity profile is strongly depends on the geometry and liquid flow injections.

In ***Fig. 32*** is presented the temperature dependence of characteristic lengths of interaction with defects $l = v_F\tau$, the mean free path of electron-electron scattering $l_2 = v_F\tau_2$, and the vorticity diffusion length $D_\eta = \sqrt{\eta\tau}$ in a W = 5 μm sample. The study shows that developed current whirlpools are sensitive to the geometry and confinement effect [50, 55, 60]. However, the careful inspection of theoretical results [55] reveals that geometry NL1 exhibits the occurrence of whirlpools only above the threshold value of $D_\eta = 0.225W$ ***(Fig. 32)***. The vicinity geometry NL2, by contrast, allows the formation of current whirlpools for arbitrary small values of D_η. However, the value of D_η effects the spatial extension of the whirlpools, therefore, a high viscosity system facilitates observation of the negative vicinity resistance for a voltage detector placed at a large distance from the current injection probe. Moreover, the ballistic effect may induce the negative vicinity signal [51] and, therefore, requires more careful qualitative analysis.

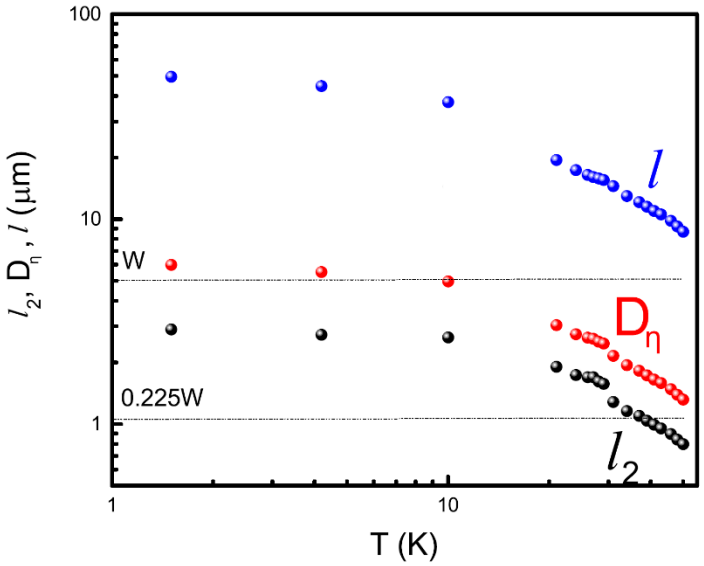

Fig. 32 *The characteristic parameters as a function of the temperature for the sample with width W = 5 μm. The whirlpool threshold is indicated by the dashes.*

3.6 Conclusion

In the conclusion, it is necessary to note that in the ballistic regime resistance has a strong dependence on device geometry and size effects. The magnitude of the ballistic effect depends on the ratio between sample width (W) and the Larmor radius (R_L). Analyze of ballistic samples were done to better-understanding MT effects that can take place in different geometries.

We have measured the evolution of several magnetotransport characteristics in high quality GaAs quantum wells with temperature at different configuration. In order to fulfill requirements for a hydrodynamic regime, we use mesoscopic samples, where very recently numerous different predictions have been made. These results open possibilities to control the current flow in microstructures by variation of the viscosity and manipulation of the fluids at a micro and nanoscale, developing new microtechnologies.

The Poiseuille flow was modelled for local, Hall and non-local configurations. Results of the modelling showed that the velocity profile strongly depends on the geometry and liquid flow injections. Also, the contribution from the ballistic and hydrodynamic effects in the varying magnetic field $\vec{B}$ can obscure each other. In addition the relative ballistic contribution $\rho_{xx}^{ball}/\rho_0^{bulk}$ exhibits strong variation with W=R_L, where R_L is the Larmor radius, because the resistivity directly depends on the relaxation time τ through the boundary scattering, while relative contribution to the Hall effect $\rho_{xy}^{ball}/\rho_{xy}^{bulk}$ is almost independent of it, since the Hall effect does not depend on the relaxation time.

We have measured the evolution of the longitudinal and Hall resistivities with temperature in high-quality GaAs quantum wells. Our observations are correlated with the predictions of classical Hall viscosity for electron flow.

Also, we have studied nonlocal transport in a mesoscopic two-dimensional electron system in terms of viscosity of the fluids. In contrast to the Ohmic flow of the particles, viscous flow can result in a backflow of the current and negative nonlocal voltage. We have measured voltage in different arrangements of current and voltage contacts and found a negative response, which we attributed to the formation of current whirlpools. Nonlocal viscosity-induced transport is strongly correlated with observations of the Gurzhi effect and low magnetic field transport described by hydrodynamic theory.

Bibliography

1. D. K. Ferry, S. M. Goodnick, and J. Bird "*Transport in nanostructures*" (2009).
2. M. N. Baibich, J. M. Broto, A. Fert, F. Nguyen Van Dau, F. Petroff, *Phys.Rev.Lett.**61**.2472 (1988).*
3. G. Binasch, P. Grünberg, F. Saurenbach, W. Zinn, *Phys.Rev.B.**39**.4828 (1989).*
4. K. von Klitzing "The quantized Hall effect" Nobel lecture (1985).
5. H. L. Störmer, *Physica B.**177**.401-408 (1992).*
6. P. D. Ye, L. W. Engel, D. C. Tsui, J. A. Simmons, J. R. Wendt, G. A. Vawter, and J. L. Reno, *Appl.Phys.Lett.**79**.2193 (2001).*
7. M. A. Zudov, I. V. Ponomarev, A. L. Efros, R. R. Du, J. A. Simmons, and J. L. Reno, *Phys.Rev.Lett.**86**.3614 (2001)*.
8. R. G. Mani, J. H. Smet, K. von Klitzing, V. Narayanamurti, W. B. Johnson, and V. Umansky, *Nature.**420** (2002).*
9. M. A. Zudov, R. R. Du, L. N. Pfeifer, and K. W. West, *Phys.Rev.Lett.**90**.046807 (2003).*
10. A. C. Durst, S. Sachdev, N. Read and S. M. Girvin, *Phys.Rev.Lett.**91**.086803 (2003).*
11. A. D. Levin, Z. S. Momtaz, G. M. Gusev, and A. K. Bakarov, *Phys.Rev.B.**89**.161304 (2014).*
12. I. A. Dmitriev, M. G. Vavilov, I. L. Aleiner, A. D. Mirlin and D. G. Polyakov, *Phys.Rev.B.**71**.115316 (2005).*
13. M. Z. Hasan, C. L. Lane, *Rev.Mod.Phys.**82**.3045 (2010).*
14. O. A. Pankratov, S. V. Pachomov, B. A. Volkov, *SolidStateComm.**61**.93-96 (1987).*
15. B. A. Bernevig, T. L. Hughes, S. C. Zhang, *Science314.1757 (2006).*
16. M. König, S. Wiedmann, C. Brüne, A. Roth, H. Buhmann, L. W. Molenkamp, X. –L. Qi and S. –C. Zhang, *Science.**318**.766 (2007).*
17. A. Roth, C. Brüne, H. Buhmann, L. W. Molenkamp, J. Maciejko, X. –L. Qi and S. –C. Zhang, *Science.**325**.294 (2009).*
18. C. Brüne, A. Roth, H. Buhmann, E. M. Hankiewicz, L. W. Molenkamp, J. Maciejko X. –L. Qi and S. –C. Zhang, *Nat.Phys.**8** (2013)*
19. B. A. Bernevig, T. L. Hughes, S. C. Zhang, *Science314.1757 (2006).*
20. S. Murakami, N. Nagaosa, S. C. Zhang, *Phys.Rev.Lett.**93**.156804 (2004).*
21. Y. Toyozawa, *J.Phys.Soc.Jpn.**17**.986 (1962).*
22. M. N. Alexander, and D. F. Holcomb, *Rev.Mod.Phys.**40**.815 (1968).*
23. C. L. Lane, E. J. Mele, *Phys.Rev.Lett.**95**.146802 (2005).*
24. B. A. Bernevig, S. C. Zhang, *Phys.Rev.Lett.**96**.106802 (2006).*
25. F. Ortmann, S. Roche and S. O. Valenzuela "Topological Insulators Fundamentals and Perspectives" (2015).
26. C. W. J. Beenaker, H. van Houten, *SolidStatePhys.**44**.1 (1991).*
27. E. M. Hankiewicz, L. W. Molenkamp, T. Jungwirth and J. Sinova, *Phys.Rev.B.**70**.241301 (2004).*
28. S. O. Valenzuela and M. Tinkham, *Nat.Phys.**442** (2006).*

29. C. Brüne, A. Roth, E. G. Novik, M. König, H. Buhmann, E. M. Hankiewicz, W. Hanke, J. Sinova and L. W. Molenkamp, *Nat.Phys.**6** (2010).*

30. D. G. Rothe, R. W. Reinthaler, C. –X. Liu, L. W. Molenkamp, S. –C. Zhang and E. M. Hankiewicz, *NewJ.Phys.**12**.065012 (2010).*

31. A. D. Chepelianskii and D. L. Shepelyansky, *Phys.Rev.B.**80**.241308* (2009).

32. T. Ando "*Electronic properties of two-dimensional systems*" (1982).

33. Y.Hirayama, S.Tarusha, *Appl.Phys.Lett.**63**.2366 (1993).*

34. J. Iñarrea and G. Platero, *Phys.Rev.Lett.**94**.016806* (2005).

35. A. D. Chepelianskii and D. L. Shepelyansky, *Phys.Rev.B.**80**.241308(R) (2009).*

36. H. A. H. Boot, R. B. R. –S. Harvie, *Nat.Phys.**4596** (1957).*

37. S. A. Mikhailov and N. A. Savostianova, *Phys.Rev.B.**74**.045325 (2006).*

38. S. A. Mikhailov, *Phys.Rev.B.**83**.155303 (2011).*

39. C. W. J. Beenakker and H. van Houten, *Solid State Physics.**44**. (1991).*

40. M. Büttiker, Y. Imry, R. Landauer and S. Pinhas, *Phys.Rev.B.**31**.6207 (1985).*

41. M. Büttiker, *Phys.Rev.Lett.**57**.1761(1986).*

42. R. N. Gurzhi, *Sov.Phys.Usp.**11**.255 (1968).*

43. R. N. Gurzhi, A. N. Kalinenko and A. I. Kopeliovich, *Phys.Rev.Lett.7**4**.3872 (1995).*

44. M. Dyakonov and M. Shur, *Phys.Rev.Lett.7**1**.2465 (1993).*

45. M. Dyakonov and M. Shur, *Phys.Rev.B.**51**.14341 (1995).*

46. A. O. Govorov and J. J. Heremans, *Phys.Rev.Lett.**92**.026803 (2004).*

47. R. Bistritzer and A. H. MacDonald, *Phys.Rev.B.**80**.085109 (2009).*

48. A. V. Andreev, S. A. Kivelson and B. Spivak, *Phys.Rev.Lett.**106**.256804 (2011).*

49. B. N. Narozhny, I. V. Gornyi, M. Titov, M. Schutt and A. D. Mirilin, *Phys.Rev.B.**91**.035414 (2015).*

50. L. Levitov and G. Falkovich, *Nat.Phys.**12**.672 (2016).*

51. T. Kawamura and S. Das Sarma, *Phys.Rev.B.**45**.3612 (1992).*

52. P. S. Alekseev, *Phys.Rev.Lett.**117**.166601 (2016).*

53. G. M. Gusev, A. D. Levin, E. V. Levinson, and A.K. Bakarov, *AIP.Adv.**8**.025318 (2018).*

54. T. Scaffidi, N. Nandi, B. Schmidt, A. P. Mackenzie and J. E. Moore, *Phys.Rev.Lett.**118**.226601 (2017).*

55. I. Torre, A. Tomadin, A. K. Geim and M. Polini, *Phys.Rev.B.**92**.165433 (2015).*

56. R. N. Gurzhi, *Sov.Phys.Usp.**11**.255 (1968).*

57. L. W. Molenkamp and M. J. M. de Jong, *Solid-State Electron.**37**.551 (1994)*.

58. M. J. M. de Jong and L. W. Molenkamp, *Phys.Rev.B.**51**.13389 (1995).*

59. L. Levitov and G. Falkovich, *Nat.Phys.**12** (2016).*

60. F. M. D. Pellegrino, I. Torre, A. K. Geim and M. Polini, *Phys.Rev.B.**94**.155414 (2016).*

61. A. D. Levin, G. M. Gusev, E. V. Levinson, Z. D. Kvon and A. K. Bakarov, *Phys.Rev.B.**97**.245308 (2018).*

62. C. W. J. Beenakker and H. van Houten, *Phys.Rev.Lett.**63**.1857 (1989).*

63. D. A. Bandurin, I. Torre, R. K. Kumar, M. B. Shalom, A. Tomadin, A. Principi, G. H. Auton, E. Khestanova, K. S. Novoselov, I. V. Grigorieva, L. A. Ponomarenko, A. K. Geim and M. Polini, *Science.**351**.1055 (2016).*

64. K. S. Novoselov, A. K. Geim, S. V. Morozov, D. Jiang, Y. Zhang, S. V. Dubonos, I. V. Grigorieva, and A. A. Firsov, *Science.**306**.666 (2004).*

65. A. K. Geim and K. S. Novoselov, *Nat.Mater.**6**.183 (2007).*

66. A. K. Geim, *Science.**324**.1530 (2009).*

67. K. S. Novoselov, *Rev.Mod.Phys.**83**.837 (2011).*

68. A. K. Geim, *Rev.Mod.Phys.**83**.851 (2011).*

69. B. A. Bernevig, T. A. Hughes, and S. C. Zhang, *Science.**314**.1757 (2006).*

70. L. Fu and C. L. Kane, *Phys.Rev.B.7**6**.045302 (2007).*

71. M. König, S. Wiedmann, C. Brne, A. Roth, H. Buhmann, L. W. Molenlamp, X. L. Qi, and S. C. Zhang, *Science.**318**.766 (2007).*

72. Y. Xia, D. Qian, D. Hsieh, L. Wray, A. Pal, H. Lin, A. Bansil, D. Grauer, Y. S. Hor, R. J. Cava, and M. Z. Hasan, *Nat.Phys.**5**.398 (2009).*

73. Z. K. Liu, B. Zhou, Y. Zhang, Z. J. Wang, H. M. Weng, D. Prabhakaran, S. –K. Mo, Z. X. Shen, Z. Fang, X. Dai, Z. Hussain, and Y. L. Chen, *Science.**343**.864 (2014).*

74. S. Borisenko, Q. Gibson, D. Evtushinsky, V. Zabolotnyy, B. Büchner, and R. J. Cava, *Phys.Rev.Lett.**113**.027603 (2014).*

75. S. –Y. Xu, I. Belopolski, N. Alidoust, M. Neupane, C. Zhang, R. Sankar, S. -M. Huang, C. –C. Lee, G. Chang, B. Wang, G. Bian, H. Zheng, D. S. Sanchez, F. Chou, H. Lin, S. Jia, and M. Z. Hasan, *Science.**349**.613 (2015).*

76. B. Q. Lv, N. Xu, H. M. Weng, J. Z. Ma, P. Richard, X. C. Huang, L. X. Zhao, G. F. Chen, C. Matt, F. Bisti, V. Strokov, J. Mesot, Z. Fang, X. Dai, T. Qian, M. Shi, and H. Ding, *Nat.Phys.**11**.724 (2015).*

77. V. F. Gantmakher and I. B. Levinson, *ZhEkspTeorFiz.**74**.261 (1978)* [*Sov.Phys.JETP.**47**.133 (1978)*]

78. P. S. Alekseev, A. P. Dmitriev, I. V. Gornyi, V. Y. Kachorovskii, B. N. Narozhny, M. Schütt, and M. Titov, *Phys.Rev.Lett.**114**.156601 (2015).*

79. G. M. Gusev, E. B. Olshanetsky, Z. D. Kvon, N. N. Michailov, and S. A. Dvoretsky, *Phys.Rev.B.**87**.081311 (2013).*

80. M. König, H. Buhmann, L. W. Molenkamp, T. Hughes, C. –X. Liu, X. –L. Qi, and S. –C Zhang, *J.Phys.Soc.Jpn.77.3 (2008).*

81. F. Kisslinger, C. Ott, C. Heide, E. Kampert, B. Butz, E. Spiecker, S. Shallcross and H. B. Weber, *Nat.Phys.**11**.650 (2015).*

82. J. Klier, I. V. Gornyi, and A. D. Mirilin, *Phys.Rev.B.**92**.205113 (2015).*

83. S. Wiedman, A. Jost, C. Thienel, C. Brune, P. Leubner, H. Buhmann, L. W. Molenkamp, J. C. Maan, and U. Zeitler, *Phys.Rev.B.**91**.205311 (2015).*

84. G. Y. Vasilieva, D. Smirnov, Y. L. Ivanov, Y. B. Vasilyev, P. S. Alekseev, A. P. Dmitriev, I. V. Gornyi, V. Y. Kachorovskii, M. Titov, B. N. Narozhny, and R. J. Haug, *Phys.Rev.B.**93**.195430 (2016).*

85. B. N. Narozhny, I. V. Gornyi, M. Titov, M. Schütt, and A. D. Mirilin, *Phys.Rev.B.**91**.035414 (2015).*

86. P. S. Aleeksev, A. P. Dmitriev, I. V. Gornyi, V. Y. Kachorovskii, B. N. Narozhny, M. Schütt, and M. Titov, *Phys.Rev.Lett.**114**.156601 (2015).*

87. P. S. Alekseev, A. P. Dmitriev, I. V. Gornyi, V. Y. Kachorovskii, B. N. Narozhny, M. Schütt, and M. Titov, *Phys.Rev.B.**95**.165410 (2017).*

88. B. N. Narozhny and A. Levchenko, *Rev.Mod.Phys.**88**.025003 (2016).*

89. U. Briskot, M. Schütt, I. V. Gornyi, M. Titov, B. N. Narozhny, and A. D. Mirlin, *Phys.Rev.B.**92**.115426 (2015).*

90. P. S. Alekseev, A. P. Dmitriev, I. V. Gornyi, V. Y. Kachorovskii, B. N. Narozhny, and M. Titov, *Phys.Rev.B.**97**.085109 (2018).*

91. G. Bian, T. –F. Chung, C. Chen, C. Liu, T. –R. Chang, T. Wu, I. Belopolski, H. Zheng, S. –Y. Xu, D. S. Sanchez, N. Alidoust, J. Pierce, B. Quilliams, P. P. Barletta, S. Lorcy, J. Avila, G. Chang, H. Lin, H. –T. Jeng, M. –C. Asensio, Y. P. Chen, and M. Z. Hasan, *2DMat.**3**.021009 (2016).*

92. W. Cao, R. –X. Zhang, P. Tang, G. Yang, J. Sofo, W. Duan, and C. –X. Liu, *2DMat.**3**.034006 (2016).*

Appendix I Magnetoresistance measurements of HgTe

In **Appendix I**, I would like to describe the initial measurements of MR of HgTe QWs in which I participated, which gave motivation for the main work. The mercury telluride is one of the compound which can be used to make a two-component system with a small band gap. Controll of the carriers concentration by adding externally positively or negatively charge quasiparticles allow to put this system at charge neutrality.

In a two-component systems near the charge neutrality Hall voltage is suppressed. This means that the quasiparticles have a strong drift in the direction perpendicular to the electric current and magnetic field. It is responsible for a strong geometrical increase of resistance in weak magnetic fields. Also, in such types of the systems, electron-hole recombination near the sample edges is present. As the result, classical edge currents may dominate the resistance in the vicinity of charge compensation. This leads to linear magnetoresistance (LMR) in two dimensions.

Phenomenological model

In this paragraph I describe the first model that was used to fit the experimental data. In this model supposed that the momentum relaxation time is much smaller than another typical scattering times. It is possible to write this as $\tau_{imp} \ll \tau_{ee}, \tau_{ph}$, where time is related to the impurity, electron-electron, and electron-phonon scattering. Previous assumptions lead to diffusive motion of carriers.

In my work I studied HgTe samples at charge neutrality. To fit experimental data, I used theory suggested by Alekseev in his work **[87]** for the situation of symmetric parabolic spectrum at charge neutrality.

The LMR is derived from the Boltzmann kinetic equation and continuity equation. First one it is possible to write as:

$$\vec{v}\frac{\partial f}{\partial \vec{r}} + e\left(\vec{E} + \vec{v} \times \vec{B}\right)\frac{\partial f}{\partial \vec{p}} = St[f]. \qquad (1)$$

Where for the case of charge neutrality is used Fermi distribution function $f = \frac{1}{e^{\varepsilon/T}}$. ε is the symmetric parabolic spectrum which has the following form: $\varepsilon = \frac{\Delta}{2} + \frac{p^2}{2m}$. Right side of the

equation consists of the collision integral which includes contributions from the impurity, electron-phonon, and electron-electron scattering.

In the presence of an external magnetic field, the system is going out of equilibrium. This deviates the quasiparticle densities from their equilibrium values. The nonequlibrium densities and currents are connected by the continuity equation:

$$divj_{e(h)} = -\frac{\delta n_e + \delta n_h}{2\tau_R}, \tag{2}$$

where τ_R is the quasiparticle recombination time.

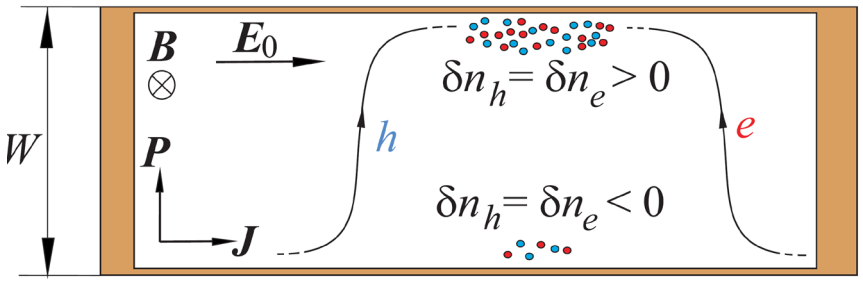

Fig. 33 *Typical semi classical trajectories for oppositely charged quasiparticles in two-component systems at charge neutrality. (copied from [87]).*

In the ***Fig. 33*** schematically presents the situation of a two-particle system at charge neutrality in the presence of external fields. Compensated Hall effect leads that quasiparticle currents flow in the same direction in the bulk of the sample. It is possible to write the quasiparticle flow as a sum of quasiparticle currents for electrons and holes, $\vec{J} = \vec{J}_e + \vec{J}_h$. For the case when the system is symmetric, the quasiparticle flow is orthogonal to external field. The quasiparticles can be accumulated near the boundaries with a width of the order of the recombination length l_R.

As was mentioned before, the motion of quasiparticles has the diffusive character. To simplify, the diffusion coefficient is assumed to be the same for electrons and holes and has the form:

$$D = \frac{T\tau}{m}, \tag{3}$$

where the momentum relaxation time τ is constant.

Then it is necessary to introduce recombination rates for electrons and holes. For my case, the recombination rates are the same:

$$\Gamma = 2\gamma n_{e,h}, \tag{4}$$

where the coefficient γ(T) depends on a particular model of electron-hole recombination. Diffusion coefficient and recombination rate are included for the expression of recombination length:

$$l_R = \sqrt{\frac{2eD}{\Gamma(1+\omega_c^2\tau^2)}}. \tag{5}$$

Also, I used expression for the resistance obtained by Alekseev in his work **[87]**. It has the following form:

$$R_{xx} = \frac{m}{e^2\tau\rho_0}\frac{1+\omega_c^2\tau^2}{1+\omega_c^2\tau^2 F\left(\frac{W}{l_R}\right)}, F(x) = \frac{tanh(x)}{x}, \tag{6}$$

where $\rho_0 = n_{0,e} + n_{0,h}$ is the quasiparticle density.

Hydrodynamic model

Previously, I described the phenomenological model that was used. However, the particle dynamics in the measured samples was more complex and could not be explained by only one model. The second model which I used in my simulations was the hydrodynamic model. This model is applicable when the mean free path of electron-electron interactions is much smaller than other characteristically lengths. In this case particles have collective motion that can affect the resistance.

For the two-component systems is characteristic that particle flow depends from the quasiparticle recombination near the edges of the sample and impurity, electron-electron, and electron-phonon scattering. Viscous effect starts to play a role when the mean free path between electron-electron interactions is bigger than the sample dimensions. In the hydrodynamic regime particles accumulated near the sample edges can form a small layer along the sample edge which is characterized by Gurzhy length. In this case the hydrodynamic regime can include particle recombination near the edge regions of the sample and viscous flow along the edges. For my samples I calculated that the sample width and recombination length l_R is much longer than the Gurzhy length l_G.

To describe particle motion in the hydrodynamic regime, it is necessary to solve two equations. Navier-Stokes equation:

$$\frac{\partial \vec{j}_\alpha}{\partial t} + \frac{\langle v^2 \rangle}{2} \nabla \delta n_\alpha - \frac{e_\alpha n_\alpha^0}{m} \vec{E} - \omega_\alpha [\vec{j}_\alpha \times \vec{e}_z] = -\frac{\vec{j}_\alpha}{\tau} - \frac{\vec{j}_\alpha - \vec{j}_{\alpha'}}{2\tau_3} + \eta_{xx} \Delta \vec{j}_\alpha + \eta_{xy} [\Delta \vec{j}_\alpha \times \vec{e}_z] + \xi \nabla (\nabla \vec{j}_\alpha), \quad (7)$$

where e_α is the electron or hole charge, ω_α is the cyclotron frequency, τ_3 is the electron-hole scattering time, η_{xx} and η_{xy} are the are regular and Hall components of the kinematic viscosity tensor: $\eta_{xx} = \frac{\eta}{1+(2\omega_c \tau_2)^2}$ and $\eta_{xy} = 2\omega_c \tau_2 \eta_{xx}$, and ξ is the coefficitent which includes linear combination of the bulk and shear viscosities.

And, the continuity equation:

$$\frac{\partial \delta n_\alpha}{\partial t} + \nabla \cdot \vec{j}_\alpha = -\frac{\delta n_e + \delta n_h}{2\tau_R}, \quad (8)$$

where α is the electron or hole, δn_α are the deviations of the carrier densities, $\vec{j}_\alpha$ are the carrier currents, and the τ_R is the electron-hole recombination time.

It was necessary to solve these equations for the system at charge neutrality. As for phenomenological model for the hydrodynamic model the quasiparticle density $\rho_0 = n_{0,e} + n_{0,h}$ and quasiparticle currents $\vec{J} = \vec{j}_e + \vec{j}_h$ are introduced.

In my comparison of the experimental results with theoretical data I used the solution of the ***eq. 7*** and ***eq. 8***. I assumed that the samples have electron-hole recombination. For the finite samples with electron-hole recombination, the finall expression for the resistance has the following form:

$$R = R_0 \left[\left(1 - \frac{2l_G(B)}{W} th \frac{W}{2l_G(B)}\right) - \left(1 - \frac{2l_R}{W} th \frac{W}{2l_R}\right) \frac{\omega_c^2 \tau \tau_*}{1+\omega_c^2 \tau \tau_*} \right]^{-1}, \quad (9)$$

where l_G is the Gurzhy length and l_R is the recombination length. I used the following expressions for Gurzhy and recombination length respectively:

$$l_R = \sqrt{\frac{\langle v^2 \rangle \tau_R \tau}{2}} \; and \; l_G(B) = \sqrt{\frac{\eta_0 \tau_*}{1+(2\omega_c \tau_{ee})^2}}, \quad (10)$$

where τ, τ_R is disorder mean-free time and recombination time and $\tau_* = \frac{\tau \tau_{eh}}{\tau + \tau_{eh}}$. η_0 is the shear viscosity in the absence of the magnetic field.

Samples and experimental results

In the experiments, I used the $Cd_{0.65}Hg_{0.35}Te/HgTe$ quantum wells with (013) surface orientations and a width *d* of 8–8.3 nm. Samples were prepared by using molecular beam epitaxy. The structure of samples is shown in the ***Fig. 34***. In these measurements, I used the nine-probe Hall bar samples. The gate was prepared in two steps. First, a dielectric layer containing 100 nm of SiO_2 and 200 nm of Si_3Ni_4 was first grown on the structure. Then a TiAu gate was deposited. The ohmic contacts to the 2DES were formed by the in-burning of indium. The density variation with the gate voltage was 1.09×10^{15} m^{-2} V^{-1}.

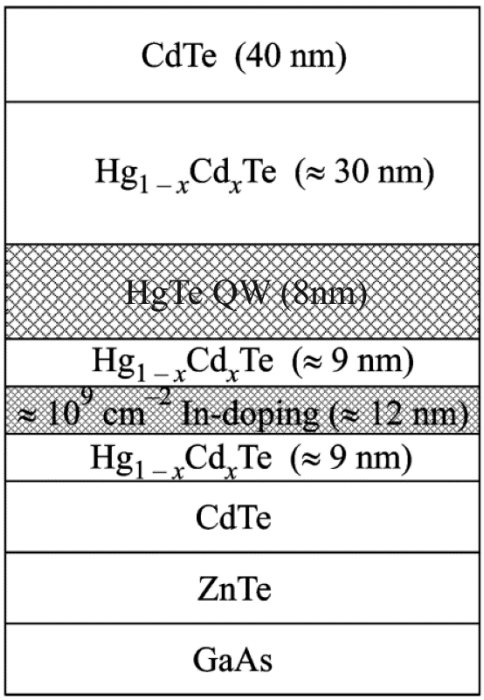

Fig. 34 *Schematic structure of HgTe QW used in our experiments.*

The MT measurements in the described structures were performed in the temperature range 1.4–4.2 K and in magnetic fields up to 6 T with a small current of 0.1–10 nA through the sample, which is sufficiently low to avoid overheating effects. The applied gate voltage V_g can vary the charge carriers density in HgTe quantum wells. The gate voltage changes into charge density, converting the conductivity of a quantum well from n-type to p-type.

The local magnetoresistance measurements were done on the several devices. The schematic view of the pattern that was used in the measurements is presented in the ***Fig. 35***.

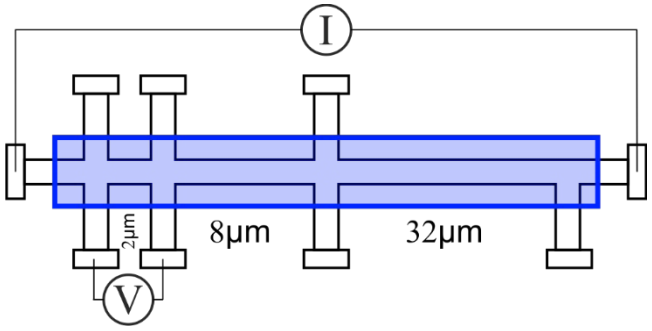

Fig. 35 *Scheme of the 9 probes Hall-bar pattern with TiAu gate.*

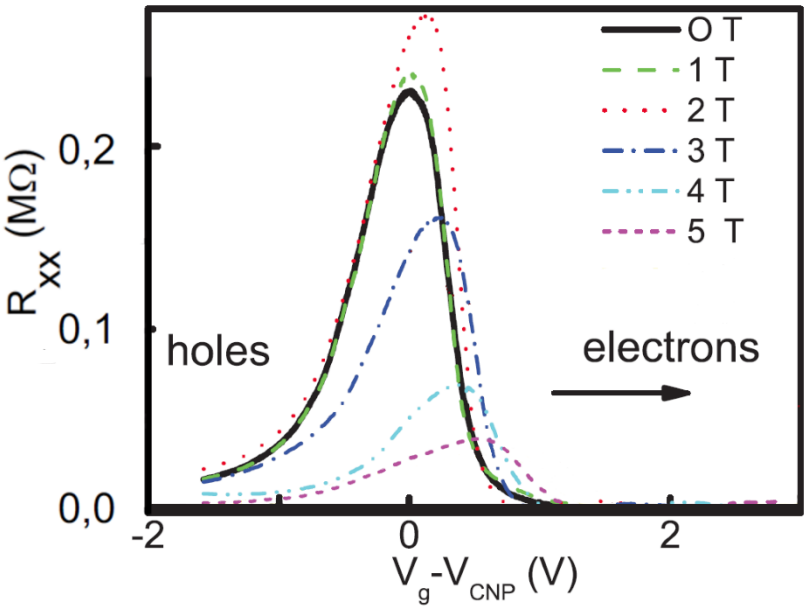

Fig. 36 *Control of the carriers density by applied gate voltage V_g (Adapted from [79]).*

Sweeping the gate voltage could allow to change the conductivity from n-type to p-type (***Fig. 36***). As it presented in the figure above, local resistance R_{xx} moves from a low value on the electron side through a maximum at the bulk energy gap to another low value on the hole side. In the ***Fig. 37*** is presented the result of magnetoresistance measurements for two different temperatures. It is possible to see the suppression of the peaks in magnetoresistance at the higher temperature. Also it is possible to see the evolution of the resistance in weak magnetic fields. The magnetoresistance has a parabolic dependence at weak magnetic fields. At the higher magnetic fields, the magnetoresistance decreases, marking a pronounced crossover to the quantum Hall effect regime. The resistance does not turn to zero, as would be expected for a conventional QHE state.

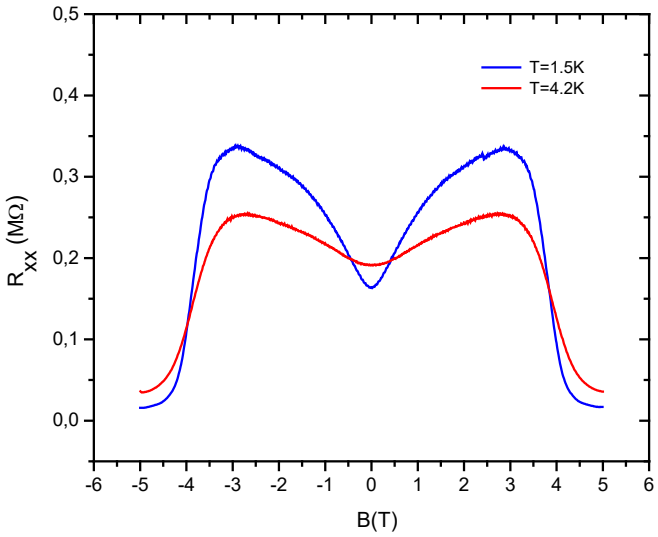

Fig. 37 *Local magnetoresistance of HgTe for different temperatures at charge neutrality.*

The next step was an attempt to describe the experiment by two theoretical models which I described below. The main parameters that were used to calculate the fits are characteristically times $\tau, \tau_R, \tau_{ee}, \tau_*$. Changing them, I did fits of the experiment.

In the ***Fig. 38*** are presented fits of the experimental results for the two models. I fitted the experimental results by phenomenological and hydrodynamic models. Fits were done for the resistance in the weak magnetic fields before 3T. The phenomenological model, red dotted line, has the parabolic dependence in all range of field. For the hydrodynamic model, green dashed line, it is possible to see more complicated dependence.

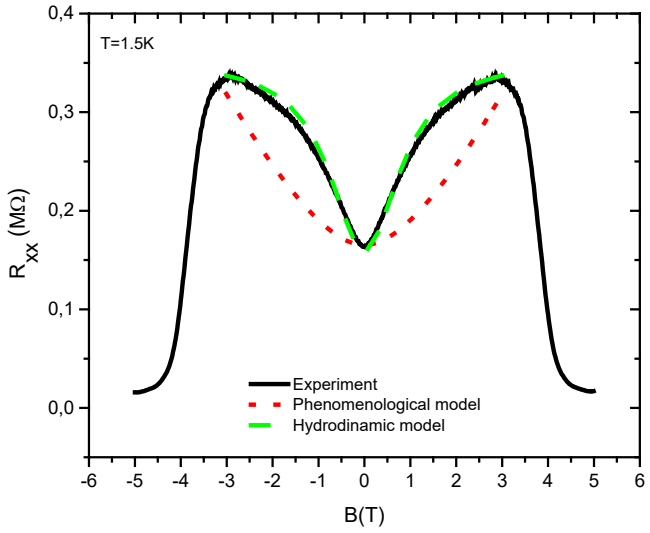

Fig. 38 *Fits of the experimental results by phenomenological (red dot) and hydrodynamic (green dash) models at T=1.5K.*

In the ***Fig. 39*** are presented fits for the higher temperature T=4.2K. For the phenomenological model it is possible to see the same parabolic dependence as in the ***Fig. 38***. For the higher temperature the hydrodynamic model gives good agreement between applied theory and experiment.

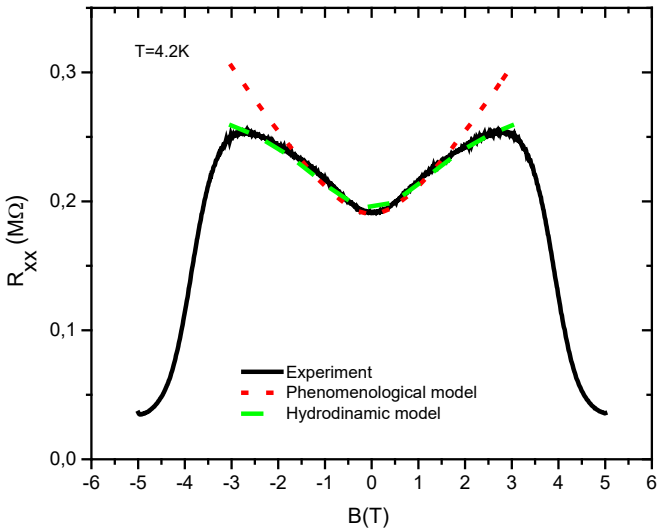

Fig. 39 *Fits of the experimental results by phenomenological (red dot) and hydrodynamic (green dash) models at T=4.2K.*

Electron mean free path can be found by using this expression $l = v_F\tau$. For the samples I studied, it gave $l \sim 10^{-6}$. Thus, the samples had a width that was of the same order as the

electron mean free path. This is not a condition that could mean that the movement in the samples was purely diffusive. However, in the ***Fig. 39*** it can be seen that the diffusion model can describe the experiment under certain conditions. Relatively small magnetic fields and temperature. With lowering temperature, the diffusion character of motion is not dominating anymore. The model can't give a good representation of experiment at any range of magnetic field. The ***Fig. 38*** and ***Fig. 39*** show significant difference when model can't be applied. As was mentioned by Alekseev **[90]** can exist a temperature limit when the electron-electron interactions can dominate. This leads to collective motion of particles and gives a permission to apply hydrodynamic model.

For the hydrodynamic model is supposed that the electron-electron interaction length is much smaller than another characteristically lengths. In the hydrodynamic model like in the diffusive I took into account particle recombination. In the ***Fig. 38*** and ***Fig. 39*** is possible to see that the model can give better representation of experiment than the phenomenological model. From this model the recombination lengths for both temperatures 1.4K and 4.2K have the same order as sample width. And the Gurzhi length is much smaller than the recombination length.

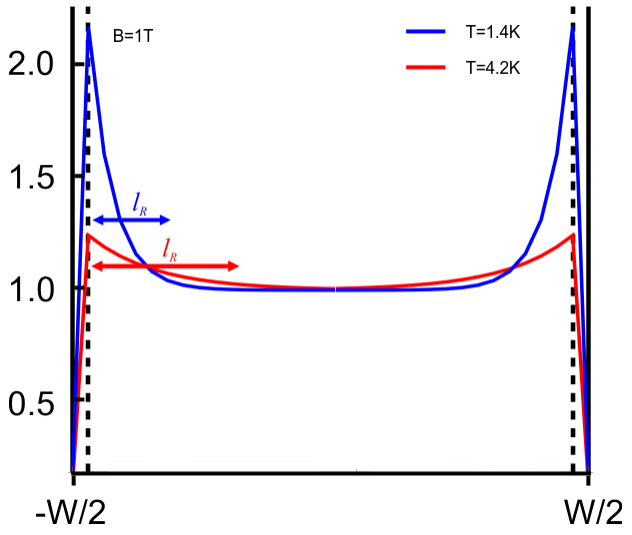

Fig. 40 *Flow profile for different temperatures at magnetic field B=1T.*

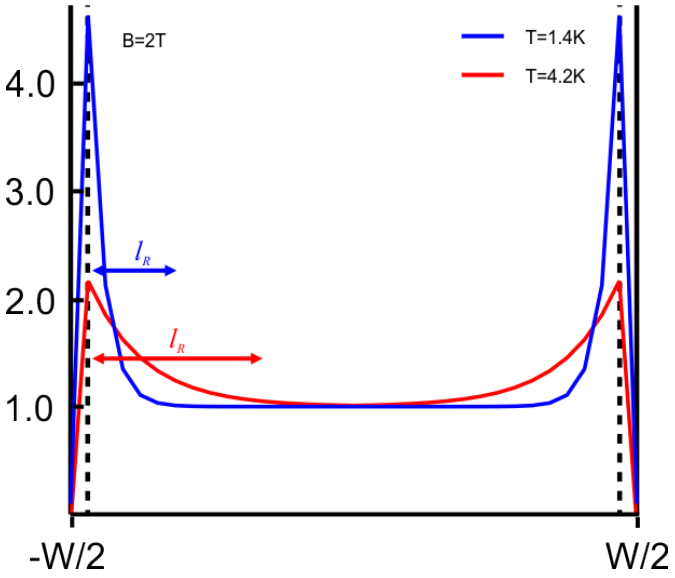

Fig. 41 *Flow profile for different temperatures at magnetic field B=2T.*

In the ***Fig. 40*** and ***Fig. 41*** are presented flow profiles at two different temperatures and magnetic field. Sample width W is equal 5×10^6μm. Plateau is normalized at 1 for both profiles. Y axis is in the arbitrary units and show the amplitude range of profile. Dashed lines are separating the boundary region and bulk of the sample. Width of this region is characterized by Gurzhy length l_G. For both temperatures and different magnetic fields Gurzhy length doesn't change significantly and it is much smaller than the sample width W and recombination length l_R. As possible to see in the figures the recombination length l_R is different for different temperatures. It has the same order that the sample width W and much longer than the Gurzhy length l_G.

Appendix II Magnetoresistance measurements of GeP

One of the extra work I did was measuring 3D GeP samples. It is a part of the ongoing collaboration with theoretical group. I took measurements on several samples at two different temperatures, 1.4K and 4.2K, to extract physical parameters. Then I plotted these results for different samples.

For most conducting pure single crystals, it is experimentally found that the application of a magnetic induction $\vec{B}$ results in an increase of the resistivity, i.e. the magnetoresistance is positive. However, in a number of heavily doped semiconductors, a negative magnetoresistance can be observed. There are many different models in the literature trying to explain this anomalous behavior. They are all related to a model by Toyozawa [21] where the conduction electrons scatter against localized spins. In a review article by Alexander and Holcomb [22] some of these models are discussed. Several mechanisms have been suggested to explain this behavior from geometrical, classical, quantum, ion implantation, and effective medium perspectives.

The experimental results are compared to a model which includes three main features: above the critical donor concentration, n_c, the electrons are delocalized; above a second critical donor concentration, n_{cb}, the Fermi level passes into the conduction band of the host crystal; for $n_c < n_d < n_{cb}$ where n_d is the donor density, the electrons exist in a poorly understood "impurity band" leading to anomalous properties.

Theory

The collaborators proposed an alternative model where the donor electrons end up in the conduction band of the host already at the critical concentration n_c. This model suggests that the anomalous properties on the metallic side of and close to the transition point are caused by many-body effects.

The first step, is to start with the relation between the Fermi wave vector k_0 and the doping density:

$$k_0 = (3\pi^2 n/\nu)^{1/3}, \quad (1)$$

where the ν is a filling factor. For Ge, it is equal to 4.

Then the relation for the Fermi energy is possible to write as follows:

$$E_0 = {\hbar^2 k_0^2}/{2m} = {\hbar^2 k_0^2}/{2m_{de} m_e}, \quad (2)$$

where m_{e} is the electron mass and m_{de} is the density of states effective mass for a Fermi sphere. Not only kinetic energy gives a contribution. There are contributions from the electrons interactions and from the interactions with the ionized-donor potentials. With these additional contributions the theory can be improved. Now, continue with the density of states. The density of states (DOS) is a quantity that determines the number of energy levels in the energy interval per volume for this study. Now, it is possible to write DOS as follows:

$$D(E) = {D(k)}\Big/{\frac{dE(k)}{dk}} = \frac{2 \cdot 4\pi k^2}{(2\pi)^3 \frac{dE(k)}{dk}} = \frac{k^2}{\pi^2 \frac{dE(k)}{dk}}. \quad (3)$$

Without any interaction between electrons ***eq. 3*** can be rewritten as:

$$D_0(E) = \frac{km}{\pi^2 \hbar^2}. \quad (4)$$

To introduce interactions between electrons it is necessary to substitute m to m^*. There the m^* is the effective mass. The effective mass has this form: $m^*(k) = m/(1 - \beta(k))$. For this case $\beta(\mathrm{k}) = \beta_{xc}(k) + \beta_b(k)$, where $\beta_{xc}(k)$ is a contribution from the exchange and correlation energy and $\beta_b(k)$ is a contribution from the band structure energy. The $\beta_{xc}(k)$ and $\beta_b(k)$ have the following form:

$$\beta_{xc}(k) = -\frac{m}{\pi^2 k} \frac{\partial}{\partial k} \frac{\delta N E_{xc}}{\delta n(\boldsymbol{k})} \text{ and } \beta_b(k) = -\frac{m}{\pi^2 k} \frac{\partial}{\partial k} \frac{\delta N E_b}{\delta n(\boldsymbol{k})}, \quad (5)$$

where E_{xc} and E_{b} exchange and correlation energy and the band structure energy, respectively. The $n(\boldsymbol{k})$ is the occupation number of the state with wave-vector **k**, N is the total number of electrons.

After the introducing initial conditions and quantities for the model, the resistivity ρ and relaxation time have the following form [24]:

$$\rho = \frac{1}{\sigma} = \frac{m^*}{ne^2\tau} \text{ and } \frac{1}{\tau} = \frac{4}{3} \frac{\nu e^4 m}{\pi \hbar^3 \kappa^2} \int_0^{2k_0} dq \, \frac{1}{q\varepsilon^2(q,0)}, \quad (6)$$

where $\rho, \sigma, \tau, \kappa$ are the resistivity, conductivity, transport time and dielectric constant.

If turn on the magnetic field the bands with spin up electrons move up and bands with spin down electrons move down. Due to redistribution, electrons with spin down are more than with spin up. Redistribution cause difference in the effective mass at the Fermi level, conductivity and transport time. The spin-polarization parameter, *s* which can take values from 0 to 1 is defined as:

$$s = \frac{n\downarrow - n\uparrow}{n}. \tag{7}$$

Now ***eq. (1)*** can be modified:

$$k_0^{\uparrow} = \frac{k_0}{a} \text{ and } k_0^{\downarrow} = \frac{k_0}{b}, \tag{8}$$

where $a = (1-s)^{-1/3}$ and $\mathrm{b} = (1+s)^{-1/3}$. Using k_0 from the ***eq. (8)*** in ***eq. (6)***, the resistance has the following form:

$$\rho = \frac{m/e^2}{n\uparrow\tau\uparrow(1-\beta\uparrow)+n\downarrow\tau\downarrow(1-\beta\downarrow)}. \tag{9}$$

The experimental results for resistivity are not given in the terms of spin-polarization parameter *s*, but as the function of the magnetic field, $\vec{B}$. For the measurements that were performed at the small magnetic fields relation between s and *B* has linear character:

$$B(T) = 2.64262 \times \frac{10^{-11}\left(\frac{n[cm^{-3}]}{\nu}\right)^{2/3}}{m_{de}(\chi/\chi_0)} s, \text{ where} \tag{10}$$

the spin-susceptibility enhancement-factor (χ/χ_0), used as a fitting parameter.

Samples and experimental results

I measured magnetoresistance of Ge samples with different doping concentration. Samples had the following characteristics, p-type, P doped (100)-oriented square of 7×7 mm^2, Ge samples were implanted with phosphorus at room temperature. The implanted P doses were ranged from 2×10^{13} cm^{-2} to 1.1×10^{12} cm^{-2}. Annealing and electrical activation were performed at 600 ^{0}C for 1 minute in the argon. Indium contacts were put at the corners of the samples to made Van der Pauw structure. Then, contacts were annealed to improved conductivity, for 1 minute at 80 ^{0}C. MT measurements were performed in VTI cryostat by using lock-in measurements technic (see ***Fig. 10***).

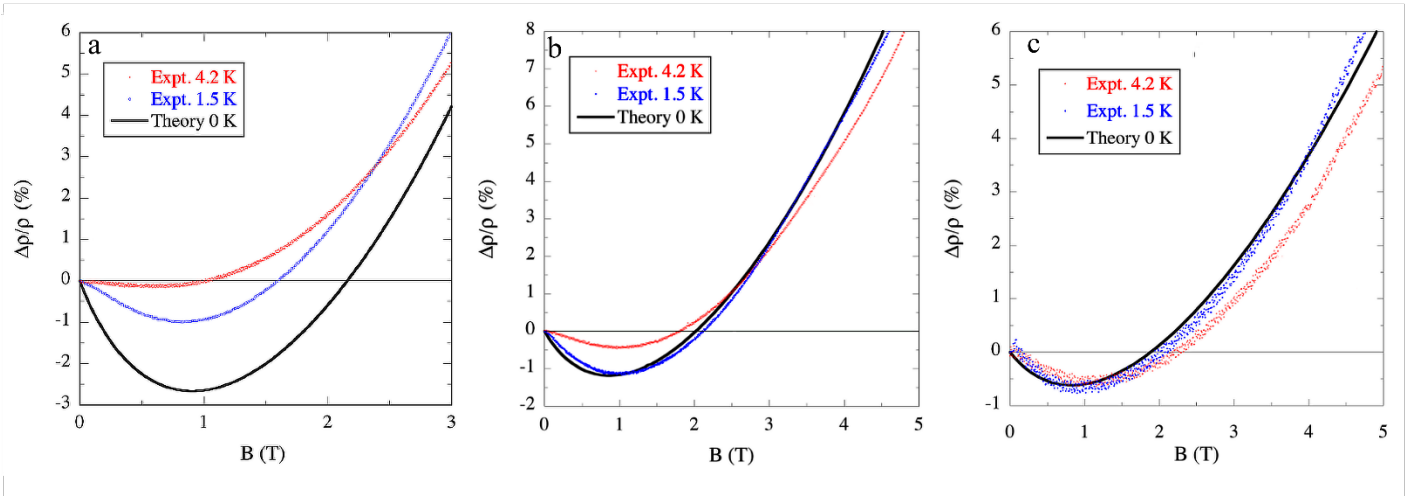

Fig. 42 *The magnetoresistance at the temperatures 4.2 K (red curve) and 1.5 K (blue curve) as a function of magnetic field B.*
GeP with doping concentrations: a) 2.96×10^{17} cm^{-3}; b) 6.25×10^{17} cm^{-3}; c) 1.17×10^{18} cm^{-3}.
The black solid curve is the theoretical result for 0 K.

The results of measurements and their comparison with the theory for samples with different doping concentrations are presented in the ***Fig. 42***. In the ***Fig. 42* (a)** are presented results for the sample with lower doping concentration. It is possible to see good minimum that increases for lower temperature. In the ***Fig. 42 (b)*** are presented results for a sample with larger concentration. In the ***Fig. 42 (c)*** are presented results for the sample with the highest doping concentration. The theoretical result fits close to the obtained experimental results. In all of these figures ***(a)***, ***(b)***, ***(c)*** it is possible to see two effects. Lowering of the doping concentration gives higher minima but at the same time, increasing temperature gives shallower minima.

Conclusion

Magnetoresistance of phosphorous doped germanium was measured and compared with theoretical calculations. The resistance was calculated by using the generalized Drude approach. Measurements show good agreement with theoretical calculations. In the ***Fig. 42*** for samples with different doping concentration it is possible to see negative magnetoresistance. Minima of the magnetoresistance are decreasing with increasing the doping concentration. The main contribution to negative magnetoresistance, in this case, comes from the many-body effect.

The many-body effects related to the enhancement of negative magnetoresistance. When the magnetic field is off the density of states is enhanced at the Fermi level and consequently, the resistance is lowered. When a magnetic field is applied, the bands are splitting for two, with

movement down for a spin down and up for spin up. Due to redistribution of electrons with up and down spins the Fermi level is the same for all bands. After the apply magnetic field, the Fermi wave-number has two values for spin up $k_0^{\uparrow}$ and spin down $k_0^{\downarrow}$. Magnetic field increases the density of states with spin up and down electrons. For electrons with spin up or down, only one remains at the Fermi level, other electrons move to an unoccupied part of the bands. Only the enhancement at the Fermi level can affect the resistivity. This is explaining negative magnetoresistance at the small magnetic fields.

Appendix III Microwave power dependence of GaAs samples in ballistic regime

DEG interaction models with microwave

The experimental discovery of the MW-induced resistance oscillations (MIRO) [6, 7] and the zero-resistance states (ZRS) [8, 9] have opened a new direction for research of non-equilibrium physics.

Most importantly, the observed phenomena demonstrated that the combined effect of the Landau quantization in the weak magnetic fields and the relatively weak MW radiation can give rise to very strong changes of the transport properties of a 2DEG. These novel non-equilibrium phenomena revealed unexpected and conceptually interesting physics which has proven to be of interest in many areas of condensed-matter physics.

As I mentioned before, in the main text, we used high quality GaAs samples in the experiments. In the ***Fig. 43*** is presented the typical dependence of a resistance from the microwave. Also, in the figure below is possible to see the MIRO and ZRS effects.

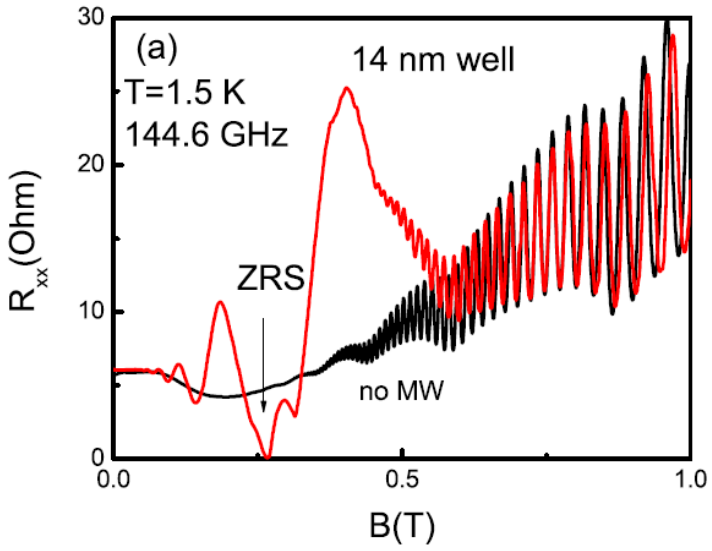

Fig. 43 *Magneto resistance w/o and with MW irradiation in a narrow quantum well. Arrows indicate the regions of vanishing resistance. MIRO is observed below 0.5 T Copied from [11].*

There are several theoretical models which can explain effects presented in the figure above. Basically they take into account interaction between low dimensional systems and MW radiation. The first is the displacement mechanism, which describes oscillations of conductivity (MIRO) and zero resistance states (ZRS) [10, 11] observed when 2DEG is illuminated by MW radiation.

Inelastic mechanism modeled by a change of the electron distribution function (see [12]). The correction to the distribution function has an oscillatory structure. The MW irradiation adds oscillations to the electronic distribution function and leads to a population inversion. In this case, it is possible to obtain states with negative conductivity.

In microwave-driven orbit mechanism, the electron orbit centers of the Landau states perform a classical trajectory consisting of a harmonic motion along the direction of the current. Thus, the 2DES moves periodically at the presence of MW. This model based on the exact solution of the electronic wave function in the presence of a static $\vec{B}$ interacting with MW radiation [34].

Ponderomotive forces model considers three types of electrons in 2DES samples: electrons far from edges, along the edge and near the contacts. Electrons in the bulk give the main contribution in the absorption experiments. In the near contact region observes an increase of the amplitude of electric field $\vec{E}$. This field $\vec{E}$ has a big inhomogeneity on the cyclotron radius scale. This can explain why in the MIRO experiments it is possible to observe several cyclotron harmonics. Edge mechanisms have been discussed separately in [35].

During the main study which included measurements of magnetoresistance in the absence of MW, I also participated in the study of the electron transport under the MW excitation. The experimental technique was modified by adding MW generator. Numerical simulations I did by applying the ballistic model.

As was mentioned before, electrons go through a sample without any interactions between them and defects. In the chapter 3.1 I presented a way how it is possible to describe electron motion in the presence of a magnetic field. If add MW electric field it is necessary to rewrite ***eq. 3.1*** as follows:

$$\vec{F} = -k\Delta\vec{r} + e\vec{E}\,cos(\omega t) + e[\vec{v} \times \vec{B}]. \quad (1)$$

Then I followed the same procedure that was shown in the chapter 3.1. In the presence of MW radiation, the ***eq. 3.3*** has the following form:

$$\frac{d\vec{V}}{dt} = -\frac{k}{mv_F}\Delta\vec{r} + \vec{\epsilon}\omega cos(\omega t) + [\vec{V} \times \vec{\omega}_c], \quad (2)$$

where $\vec{\epsilon}\omega = \frac{\vec{E}e}{\mathrm{m}v_F}$.

Finally, ***eq. (2)*** can be rewritten in new variables as follows:

$$\frac{d\vec{V}}{dT} = -\frac{kC}{mv_F}\Delta\vec{r} + \vec{\epsilon}\Omega\, cos(\Omega T) + [\vec{V} \times \vec{\Omega}_c], \tag{3}$$

where $\vec{\epsilon}\Omega = \frac{\mathrm{Ce}\vec{E}}{\mathrm{m}v_F}$ and $\vec{\mathrm{V}}$ measures in a units of the Fermi velocity. $C = 10^{-11}$ is the normalization coefficient that was chosen to scale a time.

Transformations of normalized velocity have the same form as in the chapter 3.1. Final equation has addition parameter which is responsible for the MW irradiation.

$$\frac{d^2}{dT^2}\vec{R} = -\frac{kC^2}{m}\Delta\vec{R} + \vec{\epsilon}\Omega\, cos(\Omega T) + [\frac{d\vec{R}}{dT} \times \vec{\Omega}_c]. \tag{4}$$

Fermi velocity in the samples can be estimated using the following expression for $v_F = \frac{\hbar \mathrm{k_F}}{\mathrm{m}}$, where for 2DEG $\mathrm{k_F} = (2\pi n)^{\frac{1}{2}}$, [32].

In the model described above, the shape of the wall potential is considered to be parabolic. The potential is estimated to be steepness from the assumption that the width of the region where the potential increases from the bottom to the Fermi energy is of the same order as the Fermi wavelength for typical electron concentrations. Assuming that the confinement edge potential is equal $U = \frac{kx^2}{2}$ (for coordinates outside the Hall bar geometry), the k is estimated as follows, $k = 0{,}008 meV/A^2$.

Pointing's vector and $\vec{E}$ the amplitude in the experiment

Pointing's vector is defined as $\mathrm{S} = \frac{1}{2\eta}\mathrm{E}^2 = \frac{P}{A}$, where P is the power of the source and A is the area of waveguide cross-section, η is the characteristic impedance of the transmission medium. For the used MW source the impedance is equal $\eta = 377\Omega$, $A = 1{,}33 \times 10^{-6}(m^2)$, $P = 10^{-3}(watt)$. Amplitude of $\vec{E}$ is:

$$E = \sqrt{\frac{2\times\eta\times P}{A}} \approx 753\left(V/m\right).$$

And, the ϵ coefficient is calculated from the relation:

$$\epsilon = \frac{Ee}{mv_F\omega},$$

where E is the wave amplitude, m is the effective mass of the electron and $\omega = 110 \div 170$ GHz is a frequency of MW.

I simulated trajectories of electrons at various initial conditions in the H bar patteren samples for different geometries. Electrons were injected into channel 1 with and without MW excitation. The initial position of trajectories was $x_0 = \mathrm{L}/2 - \mathrm{W}/2 + 0.3$, $y_0 = \mathrm{L}/2$. Where $\mathrm{L} = 18 \times 10^{-6}$(m) is the length and $\mathrm{W} = 3 \times 10^{-6}$(m) is the width of the "neck" of H bar pattern. Electrons were injected at the Fermi velocity, therefore the normalized velocity $\vec{\mathrm{V}} = \frac{\vec{\mathbf{v}}}{v_F}$ is equal to 1. The injection angle for trajectroties plotted in the ***Fig. 44*** was $\theta = \frac{\pi}{4.99}$. In the ***Fig. 44*** it is possible to see an example of two trajectories for electrons without and with MW excitation. As possible to see the MW excitation can strongly change the electron trajectory and, as a consequence, the dependence of the measured resistance in the samples.

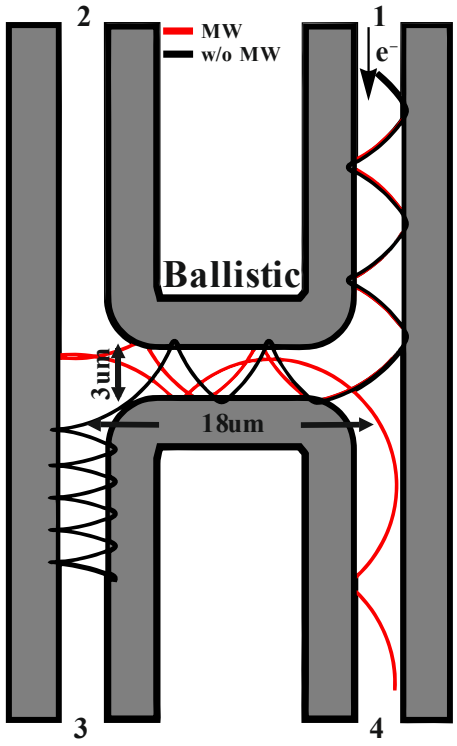

Fig. 44 *Trajectories of e⁻ in the H bar pattern w/o MW and with MW.*

MW power dependence

Also, I measured the resistance of H bar patterned samples under MW irradiation. The power dependence of local and non-local magnetoresistance was observed. The results of the experiments (solid) are presented in the ***Fig. 46*** and ***Fig. 47***. The ballistic model was able to closely reproduce the shape of the observed features. However, the most pronounced effect of

the almost complete disappearance (10 times reduction) of the non local peak at B=0,013T reproduced not very well.

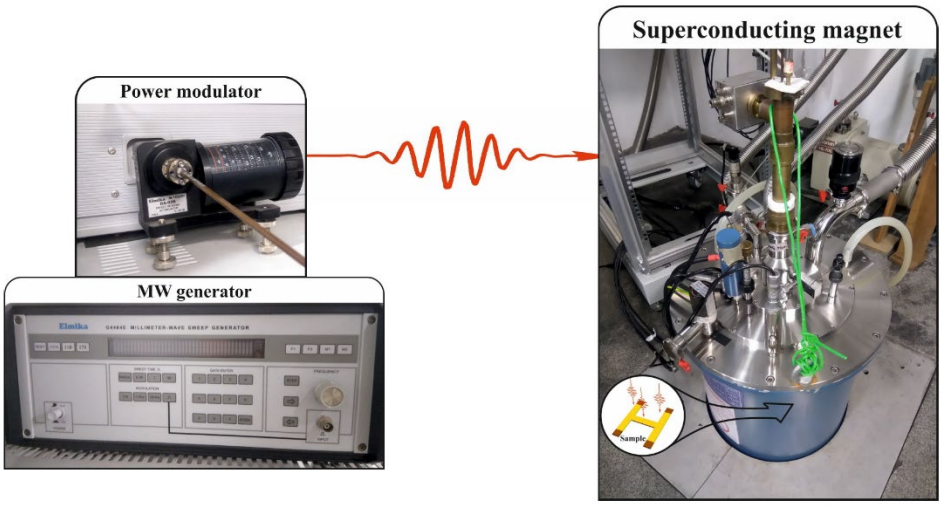

Fig. 45 *Experimental setup to measure MT in the H-Shape structure under MW excitation.*

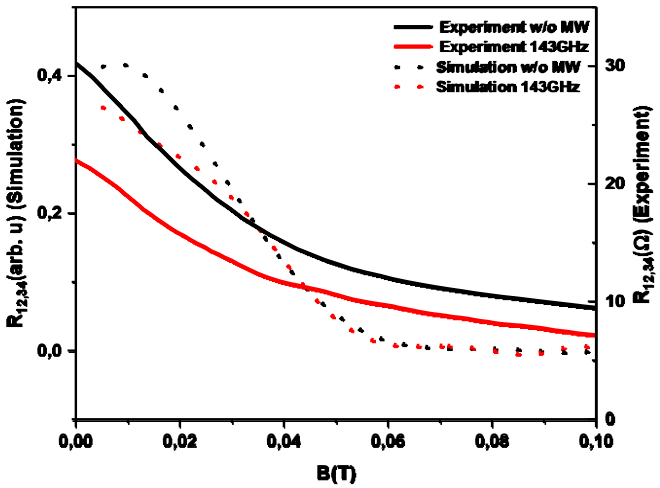

Fig. 46 *Comparison of local resistance for the H bar structure w/o and under MW irradiation (solid) with numerical simulations (dashed).*

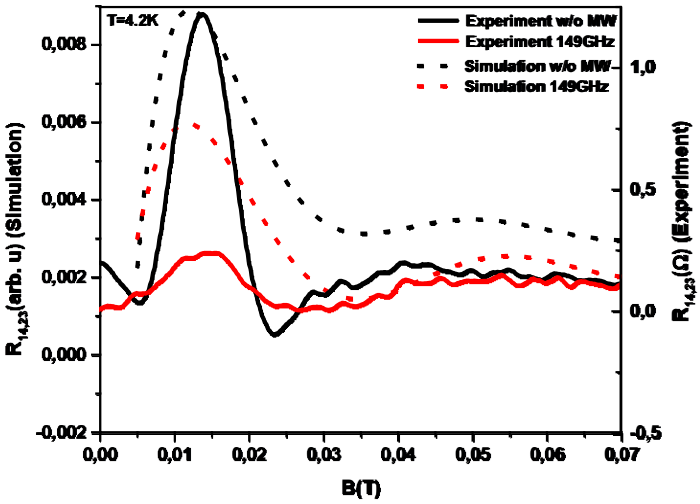

Fig. 47 *Comparison of non local resistance for the H bar structure w/o and under MW irradiation (solid) with numerical simulations (dashed).*

A larger discrepancy between the ballistic model and the experiment occurred after reproducing measurements of frequency dependence. The results are presented in the ***Fig. 48***. The geometrical parameters were varied in a wide range and had poor reproduction of experimental data.

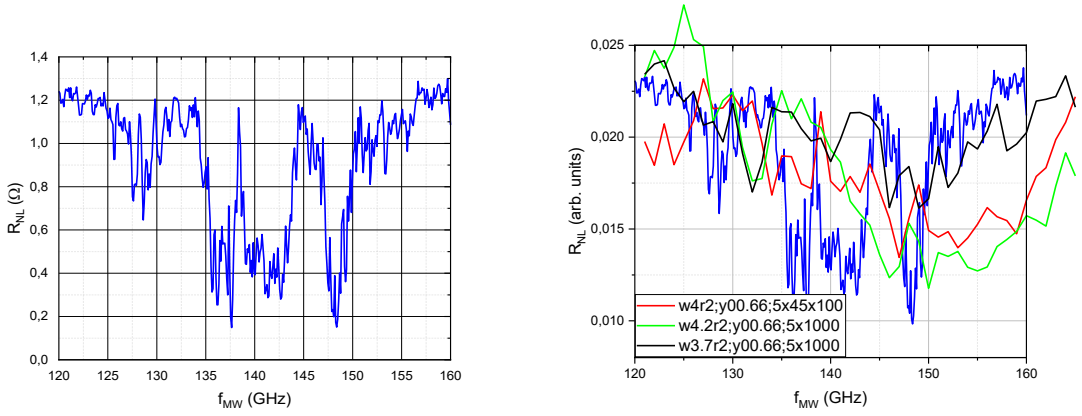

Fig. 48 *Non-local resistance as a function of MW frequency. (Left) resistance measurements, (Right) the same measurements with several attempts to fit it to ballistic model.*

Appendix IV Transmission matrix for cross geometry

It is possible to calculate only transmissions for one cross-section with terminal 1, 2, 3, 4 labeled clockwise (left half of the figure) T_{12}, T_{22}, T_{32}, T_{42}.

From these quantities the rest of the matrix can be constracted. The symmentry gives that $T_{22} = T_{11} = T_{33} = T_{44}$:

$$T = \begin{bmatrix} T_{22} & T_{12} & & \\ & T_{22} & T_{12} & \\ & T_{32} & T_{22} & T_{12} \\ T_{12} & T_{42} & & T_{22} \end{bmatrix}$$

The straight pass is symmetric too, $T_{42} = T_{13} = T_{24} = T_{31}$:

$$T = \begin{bmatrix} T_{22} & T_{12} & T_{42} & \\ & T_{22} & T_{12} & T_{42} \\ T_{42} & T_{32} & T_{22} & T_{12} \\ T_{12} & T_{42} & & T_{22} \end{bmatrix}$$

Finally, for transmission clockwise, $T_{32} = T_{43} = T_{14} = T_{21}$:

$$T = \begin{bmatrix} T_{22} & T_{12} & T_{42} & T_{32} \\ T_{21} & T_{22} & T_{12} & T_{42} \\ T_{42} & T_{32} & T_{22} & T_{12} \\ T_{12} & T_{42} & T_{21} & T_{22} \end{bmatrix}$$

Appendix V Statistical anlyses

For statistical analysis, the same modeling parameters were used with the exception of the number of trajectories, initial positions and time. Statistical analyze was the important step to optimize time of simulation. The plots are made on a logarithmic scale, where G is the conductivity $G_{L(NL)} = R_{L(NL)}^{-1}(\Omega^{-1})$.

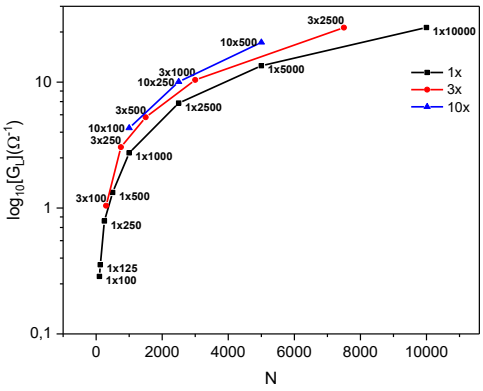

Fig. 49 *G_L vs number of points for an angle with different quantity of initial positions and R_c=W/2, $W = 3\mu m$, at B=0.02T*

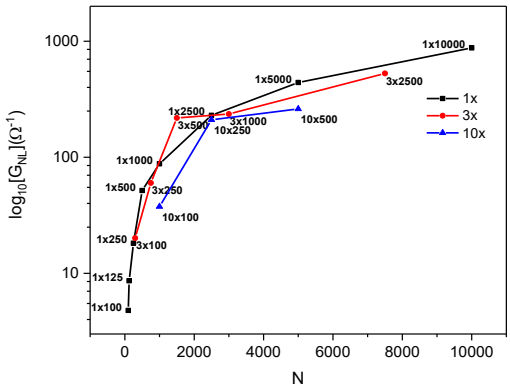

Fig. 50 *G_{NL} vs number of points for the angle with different quantity of initial positions and R_c=W/2, $W = 3\mu m$, at B=0.02*

Attachements

I. Magnetoresistance of doped germanium

Antonio Ferreira da Silva
Instituto de Fisica, Universidade Federal da Bahia, Campus Ondina 40210 340 Salvador, BA, Brazil

Alexandre Levine and Eduard Levinson
Instituto de Fisica, Universidade de São Paulo Laboratório de Novos Materiais Semicondutores 05508-090 Butantã, São Paulo, SP, Brazil

Henri Boudinov
Instituto de Fisica, Universidade Federal do Rio Grande do Sul 91501 970 Porto Alegre, Rio Grande do Sul , RS, Brazil

Bo E. Sernelius*
Division of Theory and Modeling, Department of Physics, Chemistry and Biology, Linköping University, SE-581 83 Linköping, Sweden

We have performed longitudinal magnetoresistance measurements on heavily n-doped germanium for donor concentrations exceeding the critical value for the metal-non-metal transition. The results are compared to those from a many-body theory where the donor-electrons are assumed to reside at the bottom of the many-valley conduction band of the host. Good qualitative agreement between theory and experiment is obtained.

I. INTRODUCTION

The magnetoresistance was first discovered by Lord Kelvin [1] in the middle of the 19th century. Many spectacular effects are found in either magnetic systems or in special geometrical structures [2–8]. Also in ordinary non-magnetic bulk materials there are interesting magnetoresistance effects. For all conducting pure single crystals it is experimentally found that the application of a magnetic induction **B** results in an increase of the resistivity ρ, i.e. the magnetoresistance is positive.

However, in a number of heavily doped semiconductors one observes a negative magnetoresistance. There are many different models [9–16] in the literature trying to explain this anomalous behavior. They are all related to a model by Toyozawa [17] where the conduction electrons scatter against localized spins. In a review article by Alexander and Holcomb [18] some of these models are discussed. The discussion is organized around a model which includes three main features: above the critical donor concentration, n_c, the electrons are delocalized; above a second critical donor concentration, n_{cb}, the Fermi level passes into the conduction band of the host crystal; for $n_c < n_d < n_{cb}$ the electrons exist in a poorly understood "impurity band" leading to anomalous properties. We proposed a different description [19] where the donor electrons end up in the conduction band of the host already at the critical concentration n_c. We suggested that the anomalous properties on the metallic side of and close to the transition point were caused by many-body effects. Some examples of anomalous behavior are that the resistivity, the heat capacity, and the spin susceptibility are all enhanced close to n_c. Another example is the negative magnetoresistance treated in this work.

Lately much research has been devoted to systems with positive magnetoresistance showing a linear dependence on the applied magnetic field [20–23]. Several mechanisms have been suggested to explain this behavior from geometrical [24], classical [25–27], quantum [28, 29], and effective medium [30, 31] perspectives.

In this work we focus on the magnetoresistance of heavily doped semiconductors near and on the metallic side of the metal-non-metal transition. In Ref. [32] we presented the theory but did not present any experimental results. Here we combine theory and experiment and can make comparisons. In an earlier work [33] we studied n-doped silicon and now we repeat the work for n-doped germanium.

The material is arranged in the following way. In Sec. II we present the experimental details. Sec. III is devoted to the theoretical model and derivations. Our experimental and theoretical results are compared in Sec. IV. Finally, Sec. V is a brief summary and conclusion section.

II. EXPERIMENTAL DETAILS

P-type, Ga doped (100)-oriented square, $7 \times 7\,\mathrm{mm}^2$, Ge samples with resistivity in the range of 1-10 Ωcm were implanted with phosphorus at room temperature. Five implantations with energies of 240,140, 80, 40, and 20 keV were accumulated in each sample with proper doses to result in a plateau like profile of P from the surface to the depth of about 0.40 μm, according to TRIM code simulation [34]. The implanted P doses were $2.0 \times 10^{13}\,\mathrm{cm}^{-2}$ (at

* bos@ifm.liu.se

240 keV), $6.0\times10^{12}\,\mathrm{cm}^{-2}$ (at 140 keV), $4.0\times10^{12}\,\mathrm{cm}^{-2}$ (at 80 keV), $2.0\times10^{12}\,\mathrm{cm}^{-2}$ (at 40 keV), and $1.1\times10^{12}\,\mathrm{cm}^{-2}$ (at 20 keV) in order to achieve a P atomic concentration of $1\times10^{18}\,\mathrm{cm}^{-3}$. The doses in the other samples were scaled to this sample, according to the ratio of the desired P concentration. The damage annealing and the electrical activation of P were performed at 600 C for 1 minute in argon atmosphere in a Rapid Thermal Annealing furnace to avoid high thermal budget. Van der Pauw structures [35] were fabricated by manually applied Indium contacts at the corners of the samples. Annealing at 80 C on a hot plate for 1 minute was performed to improve the contacts. The implantation process is described in Refs. [33, 36, 37].

We performed magneto-transport measurements on the described structures with Van der Pauw geometries, exploiting conventional lock-in technique with frequencies 7-13 Hz, in the temperature range of 1.5-4.2 K and bias current of 10 μA which is low enough to prevent heating effect and at the same time provide a well defined signal for our measurements. Both Hall and longitudinal resistance measurements were done in an Oxford cryostat with VTI (Variable Temperature Insert), in the presence of perpendicular magnetic field provided by a superconducting coil.

III. THEORY

We start with our approximations and notation. Most of the material is identical to what we presented for Si in Ref. [33]. To avoid duplication we just give parts that are specific for Ge and limit the rest of the material as much as possible.

Ge is a semiconductor with $\nu=4$ anisotropic conduction band valleys. There are actually 8 minima in the $(\pm1,\pm1,\pm1)/\sqrt{3}$ directions but they all are on the zone boundary so only half of each cigar shaped Fermi volume is inside the Brillouin zone. For heavily n-type doped germanium, on the metallic side of the metal-non-metal transition ($n>n_c$), the donor electrons are up in the conduction band valleys. The anisotropy has some effects on the resistivity [38] but we neglect this here and let the electrons be distributed in ν Fermi spheres. The relation between the Fermi wave vector, k_0, and the doping density, n, is given by

$$k_0=\left(3\pi^2 n/\nu\right)^{1/3}. \tag{1}$$

The Fermi energy is

$$E_0=\hbar^2k_0^2/\left(2m\right)=\hbar^2k_0^2/\left(2m_{de}m_e\right) \tag{2}$$

where m_e is the electron mass and the density of states effective mass for a Fermi sphere is $m_{de}=\left(m_l m_t^2\right)^{1/3}=.220$. Apart from the kinetic energy there are contributions from the interactions between the electrons (the exchange and correlation energy, E_{xc}) and from the interactions with the ionized-donor potentials (the band-structure energy, E_b). These interaction energies lead to a deformation of the parabolic band dispersion and a modification of the density of states. This modification is important for the effects discussed in this work so we discuss the density of states here.

The density of states is the number of states per energy and volume. The density of states from one valley is

$$\begin{aligned} D_E &= D_k/\left(dE\left(k\right)/dk\right)=\frac{2\cdot4\pi k^2}{(2\pi)^3(dE(k)/dk)} \\ &= \frac{k^2}{\pi^2(dE(k)/dk)}, \end{aligned} \tag{3}$$

where we have taken into account that in each valley there are two states for each $\mathbf{k}$, one with spin up and one with spin down. For non-interacting electrons the corresponding density of states is

$$D_E^0=\frac{k^2}{\pi^2\left(dE^0\left(k\right)/dk\right)}=\frac{km}{\pi^2\hbar^2}. \tag{4}$$

We may express the density of states for interacting electrons on an analogous form by introducing a wave-number dependent effective mass,

$$D_E=\frac{km^*}{\pi^2\hbar^2}. \tag{5}$$

The effective mass can be written as

$$m^*\left(k\right)=m/\left[1-\beta\left(k\right)\right], \tag{6}$$

where $\beta\left(k\right)$ gets a contribution from each of the interaction energies, $\beta\left(k\right)=\beta_{xc}\left(k\right)+\beta_b\left(k\right)$, where

$$\begin{aligned} \beta_{xc}\left(k\right) &= -\tfrac{m}{\pi^2k}\tfrac{\partial}{\partial k}\tfrac{\delta N\cdot E_{xc}}{\delta n(\mathbf{k})}, \\ \beta_b\left(k\right) &= -\tfrac{m}{\pi^2k}\tfrac{\partial}{\partial k}\tfrac{\delta N\cdot E_b}{\delta n(\mathbf{k})} \end{aligned} \tag{7}$$

The quantity $n\left(\mathbf{k}\right)$ is the occupation number of the state with wave-vector $\mathbf{k}$, and N is the total number of electrons. One effect of the interactions, that turns out to be very important for the present work, is that the effective mass and density of states are enhanced in a region around the Fermi level (see Fig. 3 of Ref. [32]).

The resistivity we calculate by using the so-called generalized Drude approach [39–41]. In the static case which is what we need here the results agree with the so-called Ziman's formula [42],

$$\begin{aligned} \rho &= \tfrac{1}{\sigma}=\tfrac{1}{ne^2\tau/m^*}, \\ \tfrac{1}{\tau} &= \tfrac{4}{3}\tfrac{\nu e^4 m}{\pi\hbar^3\kappa^2}\int_0^{2k_0}dq\tfrac{1}{q\tilde{\varepsilon}^2(q,0)}, \end{aligned} \tag{8}$$

where ρ, σ, τ, and κ are the resistivity, conductivity, transport time, and dielectric constant, respectively. For Ge $\kappa=15.36$.

When a static and spatially homogeneous magnetic field (magnetic induction $\mathbf{B}$) is applied the bands with spin up electrons (spin parallel to $\mathbf{B}$) move up in energy and those with spin down electrons (spin antiparallel to $\mathbf{B}$) move down. There is a redistribution of the electrons so that more electrons have spin down than have spin

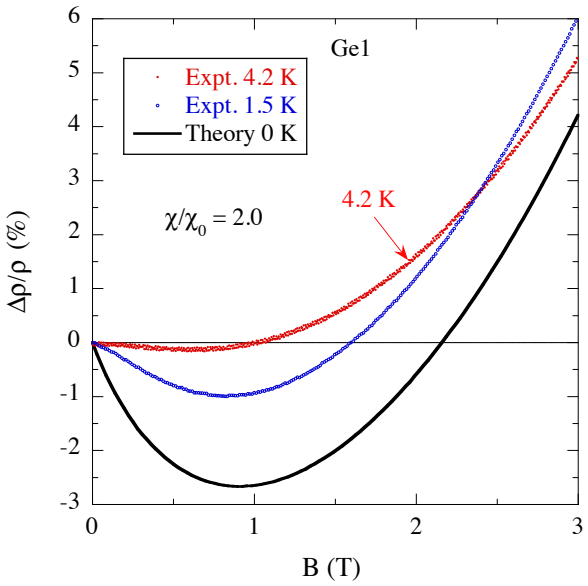

Figure 1. (Color online)The magnetoresistance at the temperatures 4.2 K (*red* curve) and 1.5 K (*blue* curve) as function of magnetic induction, B, for a Ge:P sample with doping concentration 2.96×10^{17} cm^{-3}. The *black* solid curve is our theoretical result for 0 K. See the text for details.

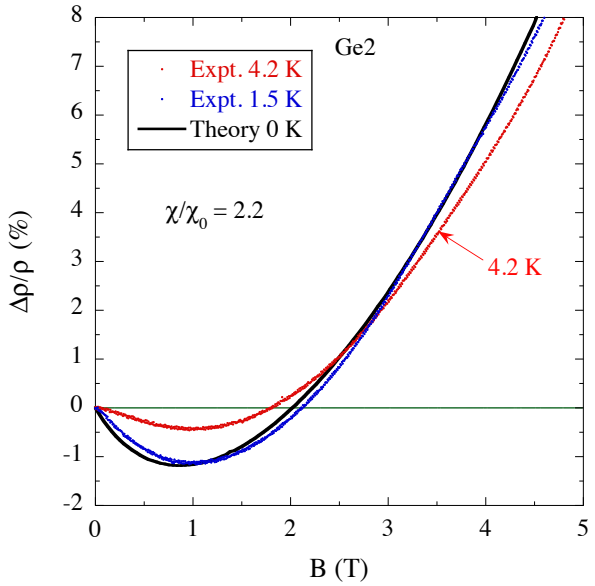

Figure 2. (Color online) The same as Fig. 1 but now for the doping concentration 6.25×10^{17} cm^{-3}.

up. This has the effect that the density of states, the effective mass at the Fermi level, the contribution to the conductivity, and the transport time are no longer the same for the two groups of electron. Let us introduce the spin-polarization parameter, s, that varies from zero in absence of **B** to 1 at full polarization (all electrons have spin down),

$$s = \frac{n^{\downarrow} - n^{\uparrow}}{n}. \tag{9}$$

The density and Fermi wave-number of spin up and down electrons are

$$\begin{array}{l} n^{\uparrow} = \frac{1-s}{2} n, \\ n^{\downarrow} = \frac{1+s}{2} n, \\ {k_0}^{\uparrow} = k_0/a, \\ {k_0}^{\downarrow} = k_0/b, \end{array} \tag{10}$$

where

$$\begin{array}{l} a = (1-s)^{-1/3}, \\ b = (1+s)^{-1/3}. \end{array} \tag{11}$$

The resistivity is now

$$\begin{aligned} \rho &= \frac{1}{n^{\uparrow} e^2 \tau^{\uparrow}/m^{*\uparrow} + n^{\downarrow} e^2 \tau^{\downarrow}/m^{*\downarrow}} \\ &= \frac{1}{\frac{n^{\uparrow} e^2 \tau^{\uparrow}(1-\beta^{\uparrow})}{m} + \frac{n^{\downarrow} e^2 \tau^{\downarrow}(1-\beta^{\downarrow})}{m}} \\ &= \frac{m/e^2}{n^{\uparrow}\tau^{\uparrow}(1-\beta^{\uparrow}) + n^{\downarrow}\tau^{\downarrow}(1-\beta^{\downarrow})}. \end{aligned} \tag{12}$$

Now we have all formalism needed for the calculation of the magnetoresistance, $\Delta\rho/\rho = [\rho(s) - \rho(0)]/\rho(0)$, as a function of spin polarization s. The detailed expressions for the quantities involved were given in Ref. [33]. The experimental results are not given as functions of s but as functions of B. If the fields are small enough we can assume a linear relation between B and s. It can be written as

$$B[T] = \frac{2.64262 \times 10^{-11} \left(n\left[cm^{-3}\right]/\nu\right)^{2/3}}{m_{de}(\chi/\chi_0)} s. \tag{13}$$

IV. EXPERIMENTAL AND THEORETICAL RESULTS

Our theoretical and experimental results are compared in Figs. 1 - 3. We have adjusted the spin-susceptibility enhancement-factor (χ/χ_0) appearing in Eq. (13) to get a reasonable fit between the theoretical and experimental curves. The adjustment only affects the theoretical curves in the horizontal direction. We have furthermore enhanced the effective mass, m_{de}, characterizing the Fermi spheres with a factor of 1.5, i.e. it has been changed from .22 to .33.

In Fig. 1 we present the results for our sample with lowest doping concentration, i.e. the sample that is closest to the metal-non-metal transition. We find rather deep minima, that increase with lowering of the temperature. The experimental results are given as functions of B. The theoretical result is obtained as a function of s, the spin polarization parameter. The theoretical relation

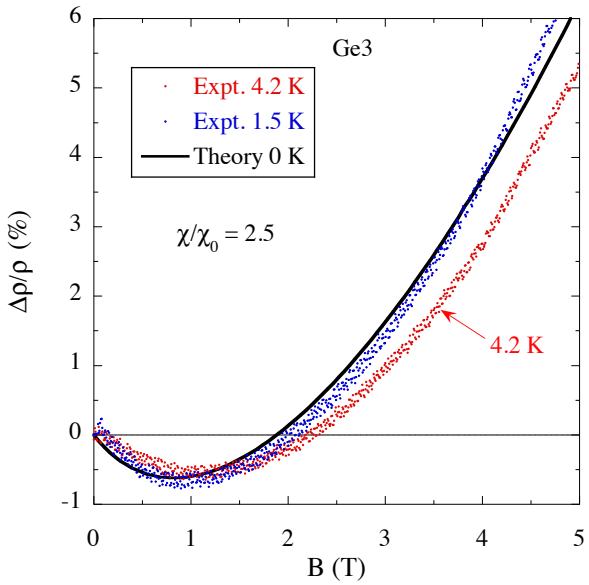

Figure 3. (Color online) The same as Fig. 1 but now for the doping concentration 1.17×10^{18} cm^{-3}.

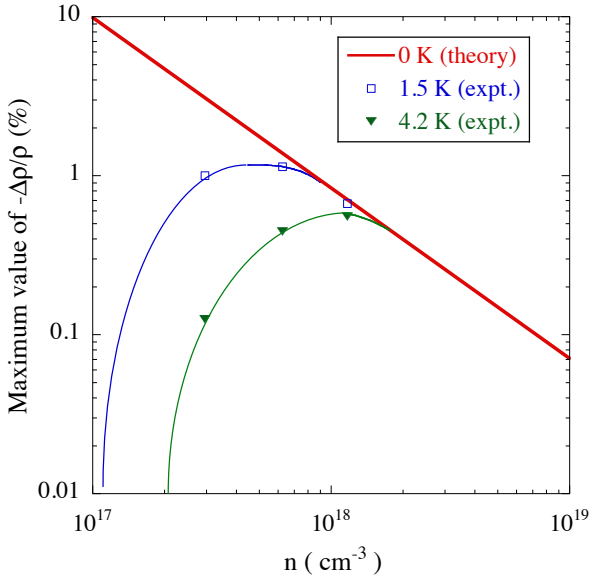

Figure 4. (Color online) The depth of the magnetoresistance minima as function of doping concentration. The *red* thick solid straight line is the theoretical result for 0 K; the *blue* open squares are the experimental results at 4.2 K; the *green* filled triangles are the experimental results for 1.5 K; the thin solid curves are just guides for the eye. See the text for details.

between B and s is found in Eq. (13). In a rather ad hoc manner we have given χ/χ_0 the value 2.0.

In Fig. 2 we present the results for our sample with the next lowest doping concentration. We find a more shallow minimum at 0 K, but the minima are a little deeper for the finite temperature results compared to what we found for the sample with lowest concentration. Here we gave χ/χ_0 the value 2.2.

Fig. 3 shows the results for our sample with the highest doping concentration. Here we gave χ/χ_0 the value 2.5.

There are two competing effects. Lowering of the doping density gives deeper minima; increasing the temperature gives shallower minima. This is clearly seen in Fig. 4 where the size of the minima as a function of doping concentration is presented for the zero temperature theoretical result and for the experimental results performed at finite temperatures.

The enhancement of the density of states at the Fermi level increases when the density comes closer to n_c ($n_c \approx 2.5 \times 10^{17}$cm^{-3} [43]) from the metallic side. It is furthermore well known that the spin susceptibility χ is more and more enhanced the closer to n_c one gets and that the enhancement is reduced when the temperature goes up [44–47].

Now, what causes the negative magnetoresistance? As we mentioned above the density of states is enhanced at the Fermi-level in absence of a magnetic field. This leads to an enhancement of the resistivity. In absence of a magnetic field the spin up and spin down bands are degenerate and the Fermi wave-numbers are the same for both spin types. When the magnetic field is introduced the spin down bands move down in energy and the spin up bands move up. There is a redistribution of electrons from the spin up bands to the spin down bands so that the Fermi-level is the same in all bands. The Fermi wave-numbers are now different in the two band types. See the inset of Fig. 2 of Ref. [33]. When the magnetic field is introduced the density of states of both electron types, i.e. spin up and spin down electrons, are enhanced for states with wave-number $k_0{}^{\uparrow}$ and $k_0{}^{\downarrow}$. This means that the peak in the density of states at the Fermi-level is for each spin type split up into two. The states involved in the enhancement of the density of states are indicated by circles in the inset of Fig. 2 of Ref. [33]. For spin up electrons one peak remains at the Fermi-level while the other moves up into the unoccupied part of the bands. For spin down electrons one peak remains at the Fermi-level and one moves further down in the occupied part of the bands. For both spin types the enhancement at the Fermi-level is hence reduced. It is only the enhancement at the Fermi level that effects the resistivity. This causes the initial negative magnetoresistance. The enhancement of the density of states at the Fermi-level for both spin types as function of magnetic induction is shown in Fig. 5 for the sample with doping concentration 2.96×10^{17} cm^{-3}.

There is another effect that acts in the same direction. There are Friedel oscillations [48] in the screening-charge density centered around each impurity potential with Fourier component $q = 2k_0$. This leads to an enhanced scattering rate in the back scattering direction across the Fermi spheres and an enhancement of the resistivity. At zero magnetic field the Friedel oscillations have the same periodicity for spin up and spin down electrons; both

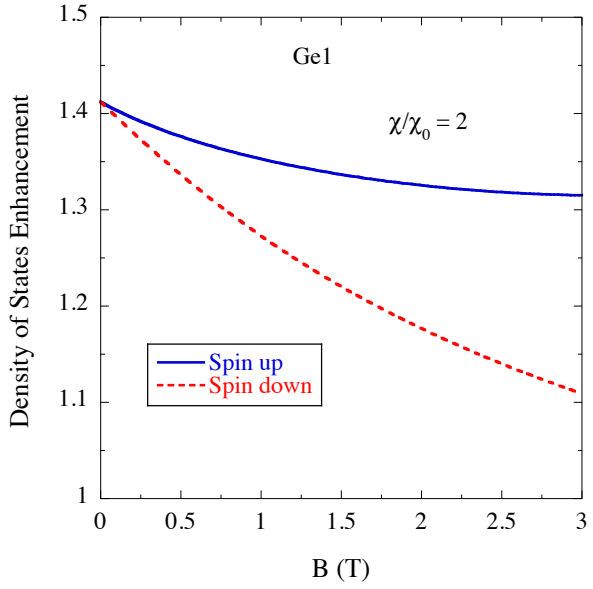

Figure 5. (Color online) The enhancement of the density of states at the Fermi level for both spin types as function of magnetic induction B. The results are valid for the doping concentration 2.96×10^{17} cm^{-3}

type of electrons scatter equally strongly against both Friedel oscillations. When the magnetic field is turned on the Friedel oscillations will split up into two; one with Fourier component $q = 2k_0{}^{\uparrow}$; one with Fourier component $q = 2k_0{}^{\downarrow}$. This means that the back-scattering rate for an electron of a certain spin against the Friedel oscillations of the opposite spin is reduced. The enhancement of the resistivity is thus reduced leading to a negative magnetoresistance. However, this effect is expected to give a much smaller contribution to the negative magnetoresistance than the density of states effect since the electron can scatter with a wave number ranging from zero up to two times the Fermi wave number.

All our calculations are for zero temperature. What happens for non-zero temperatures? If we study classical experiments [9] we find that the negative magnetoresistance effect is gradually reduced when the temperature is enhanced. This is consistent with our theory. The peak at the Fermi-level of the density of states is expected to be broadened. Besides, at zero temperature only states at the Fermi-level takes part in the conductivity. When the temperature goes up also states away from the Fermi-level where the enhancement in the density of states is weaker take part. Both these effects are expected to gradually remove the negative magnetoresistance. The temperature effects are expected to be more and more important the lower the density. This is also what what was found experimentally here and in Ref. [9].

In Fig. 4 we see that the maximum negative magnetoresistance increases linearly on a log-log plot when the density is reduced. For finite temperature the maximum is expected to start decreasing at a density that depends on the temperature. The higher the temperature the earlier the decrease is expected to set in. This is exactly what we have found and what was observed in Fig. 8 of Ref. [9].

V. SUMMARY AND CONCLUSIONS

We have performed magnetoresistance measurements of heavily phosphorous doped germanium and compared the results to theory. The resistance was calculated using the so-called generalized Drude approach taking many-body effects into account. We propose that the origin of the negative magnetoresistance is a combination of two effects. The many-body effects lead to an enhancement of the density of states at the Fermi level which in turn results in an enhancement of the resistivity. Friedel oscillations in the screening charge density cause an enhanced back-scattering rate across the Fermi volumes leading to an additional enhancement of the resistivity.

When the magnetic field is turned on the enhancement of the density of states for each spin type is split up into two peaks, one at the Fermi-level and one that moves away from the Fermi-level with enhanced magnetic field. This reduces the resistivity. Also, the back-scattering rate against the Friedel oscillations will be reduced in the presence of a magnetic field. Both these effects act towards a negative magnetoresistance. The first effect is expected to be dominating.

We found good agreement between theory and experiment. More experimental samples in the doping range 10^{18}-10^{19} cm^{-3} would be helpful for further verification of the theory.

ACKNOWLEDGMENTS

A.F.d.S., A.L., E.L., and H.B. acknowledge financial support of the Brazilian agencies National Research Council of Scientific and Technological Development (CNPq), Bahia Research Foundation (FAPESB)/PRONEX, CAPES Foundation within the Ministry of Education, and São Paulo Research Foundation (FAPESP).

[1] W. Thomson, Proc. Royal Soc. London **8** 546 (1857).
[2] M. N. Baibich, J. M. Broto, A. Fert, F. Nguyen Van Dau, F. Petroff, P. Etienne, G. Creuzet, A. Friederich, and J. Chazelas, Phys. Rev. Lett. **61**, 2472 (1988).
[3] G. Binasch, P. Grünberg, F. Saurenbach, and W. Zinn, Phys. Rev. B **39** 4828 (1989).

[4] G. H. Jonker, and J. H. Van Santen, Physica **16**, 337(1950).
[5] A. P. Ramirez, Journal of Physics: Condensed Matter **9**, 8171(1997).
[6] M. Julliere, Phys. Lett. **54A**, 225 (1975).
[7] S. A Solin, T. Thio, D. R. Hines, J. J. Heremans, Science **289**, 1530 (2000).
[8] M. N. Ali, J. Xiong, S. Flynn, J. Tao, Q. D. Gibson, L. M. Schoop, T. Liang, N. Haldolaarachchige, M. Hirschberger, N. P. Ong, and R. J. Cava, Nature **514**, 205 (2014).
[9] C. Yamanouchi, K. Miziguchi, and W. Sasaki, J. Phys. Soc. Jpn. **22**, 859 (1967), and references therein.
[10] W. Sasaki, J. Phys. Soc. Jpn. **21**, 543 (1966).
[11] A. N. Ionov, I. S. Shlimak, and A. L. Efros,Fiz. Tverd. Tela **17**, 2763 (1975) [Sov. Phys. Solid State **17**, 1835 (1976)].
[12] D. G. Andrianov, G. U. Lazareva, A. S. Savel'ev, and V. I. Fistul', Fiz. Tekh. Poluprovodn. **9**, 210 (1974) [Sov. Phys. Semicond. **9**, 141 (1975)].
[13] E. I. Zavitskaya, I. D. Voronova, and N. V. Roshdestvenskaya, Fizika Tekhn. Poluprov. **6**, 1945 (1972) Fizika Tekhn. Poluprov. 6, 1945 (1972) [Sov. Phys. Semicond.6, 1668 (1973)].
[14] 0. V. Emel'yanenko, T. S. Lagunova, K. G. Masagutov, D. N. Nasledov, and D. D. Nedeoglo, Fiz. Tekh. Poluprovodn. **9**, 1517 (1975) [Sov. Phys. Semicond. **9**, 1001 (1976)].
[15] S. Ishida and E. Otsuka, J. Phys. Soc. Jpn. **42**, 542 (1977).
[16] B. P. Khosla and J. R. Fisher, Phys. Bev. B **2**, 4084 (1970).
[17] Y. Toyozawa, J. Phys. Soc. Jpn. **17**, 986 (1962)
[18] M. N. Alexander, and D. F. Holcomb, Rev. Mod. Phys. **40**, 815 (1968).
[19] B. E. Sernelius, and K.-F. Berggren, Phil. Mag. **43** 115 (1981).
[20] H. G. Johnson, S. P. Bennett, R. Barua, L. H. Lewis, and D. Heiman, Phys. Rev. B **82**, 085202 (2010).
[21] N. A. Porter, and C. H. Marrows, Sci. Rep. 2, 565 (2012).
[22] Tao Wang, Zhaolong Yang, Wei Wang, Mingsu Si, Dezheng Yang, Huiping Liu, and Desheng Xue, AIP Advances **7**, 056604 (2017).
[23] V. F. Mitin, V. V. Kholevchuk, and E. A. Soloviev, Appl. Phys. Lett. **110**, 012102 (2017).
[24] W. R. Branford, A. Husmann, S. A. Solin, S. K. Clowes, T. Zhang, Y. V. Bugoslavsky, and L. F. Cohen, Appl. Phys. Lett. **86**, 202116-1 (2005).
[25] M. M. Parish, and P. B. Littlewood, Nature (London) **426**, 162 (2003).
[26] M. M. Parish, and P. B. Littlewood, Phys. Rev. B **72**, 094417 (2005).
[27] J. Hu, M. M. Parish, and T. F Rosenbaum, Phys. Rev. B **75**, 214203 (2007).
[28] A.A. Abrikosov, Phys. Rev. B **58**, 2788 (1998).
[29] A.A. Abrikosov, Europhys. Lett. **49**, 789 (2000).
[30] V. Guttal and D. Stroud, Phys. Rev. B **71**, 201304(R) (2005).
[31] V. Guttal and D. Stroud, Phys. Rev. B **73**, 085202 (2006).
[32] Bo E. Sernelius, and K.-F. Berggren, Phys. Rev. B **19**, 6390 (1979).
[33] A. F. da Silva, A. Levine, Z. S. Momtaz, H. Boudinov, and Bo E. Sernelius, Phys. Rev. B **91**, 214414 (2015).
[34] J. F. Ziegler, J. P. Biersak, and U. Littmark, *The Stopping and Ranges of Ion in Solids* Vol. I (Pergamon, New York, 1985).
[35] L. J. Van der Pauw, *Philips Res. Rep.* **13**, 1 (1958).
[36] A. Ferreira da Silva, Bo E. Sernelius, J. P. de Souza, H. Boudinov, H. Zheng, and M. P. Sarachik, Phys. Rev. B **60**, 15824 (1999).
[37] E. Abramof, A. Ferreira da Silva, Bo E. Sernelius, J. P. de Souza, and H. Boudinov, Phys. Rev. B **55**, 9584 (1997).
[38] Bo E. Sernelius, Phys. Rev. B **41**, 3060 (1990).
[39] Bo E. Sernelius, and M. Morling, in *Shallow Impurities in Semiconductors 1988*, Inst. Phys. Conf. Ser. No 95, edited by B. Monemar (IOP, Bristol, 1989), p. 555.
[40] Bo E. Sernelius, Phys. Rev. B **40**, 12438 (1989).
[41] Bo E. Sernelius, Phys. Rev. B **43**, 7136 (1991).
[42] J. M. Ziman, Phil. Mag. **6**, 1013 (1961).
[43] N. F. Mott, *Metal-Insulator Transitions*, (Taylor and Frances, London, 1974).
[44] J. D. Quirt and J. R. Marco, Phys Rev. Lett. **26**, 318 (1971).
[45] J. D. Quirt and J. R. Marco, Phys. Rev. B **7**, 3842 (1973).
[46] J. D. Quirt and J. R. Marco, Phys. Rev. B **5**, 1716 (1972).
[47] A. Ferreira da Silva, Phys. Rev. B **38**, 10 055 (1988).
[48] J. Friedel, Nuovo Cimento Suppl. **7**, 287 (1958).

Microwave induced edge transport in two-dimensional system: comparison with experiment

Instituto de Física

E. V. Levinson[1], A. D. Levin[1], G. M. Gusev[1], A. K. Bakarov[2]

1 Instituto de Física da Universidade de São Paulo
2 Institute of Semiconductor Physics, Novosibirsk State University

Introduction

- The new structure (H-shape) has been used for measurements of local and non-local resistance
- Drastic microwave (MW) effect on non-local resistance is observed
- Experimental results are modelled based on Landauer, Büttiker formalism [1,2]

Experimental setup

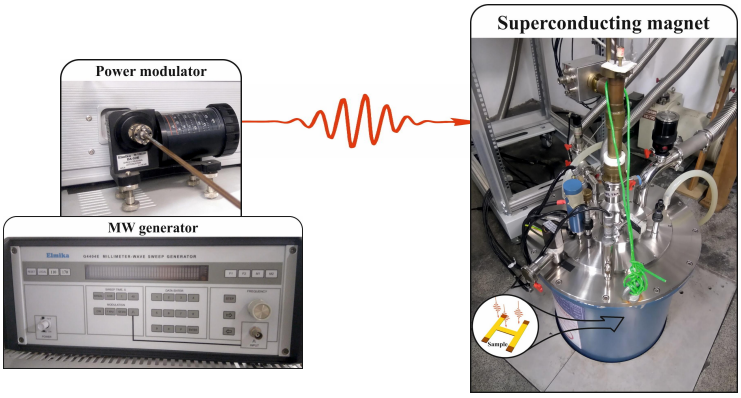

Sample

We have studied narrow (14 nm) quantum wells GaAs\AlGaAs with electron density $n_s \approx 10^{12}$ cm^{-2} and mobility $\mu = 2 \times 10^6$ cm^2/V s.

Photo of sample and photolithography designed structure

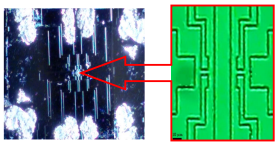

Theoretical model

Semi classical model [3]

$$\frac{d\vec{V}}{dt} = \underbrace{-\frac{k}{mv_F}\Delta\vec{r}}_{\text{soft wall potential}} + \underbrace{\vec{\epsilon}\omega\cos(\omega t)}_{\text{microwave}} + \underbrace{[\vec{V}\times\vec{\omega}_c]}_{\text{magnetic field}}$$

,where $\vec{V} = \frac{\vec{v}}{v_F}$. Resistance calculations based on Landauer formalism [1]

$$G = \left(\frac{e^2}{\pi\hbar}\right)\frac{T}{R}, \frac{1}{G} = \mathcal{R}$$

and Büttiker formula [2]

$$\mathcal{R}_{mn,kl} = \frac{h}{e^2}\frac{(T_{km}T_{ln} - T_{kn}T_{lm})}{D(T)}$$

Example of trajectories with and without MW

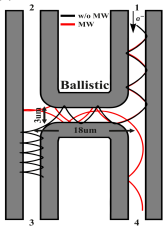

Experimental results

Comparison between experiment and theoretical calculations for local and non-local measurements with and w/o MW irradiation

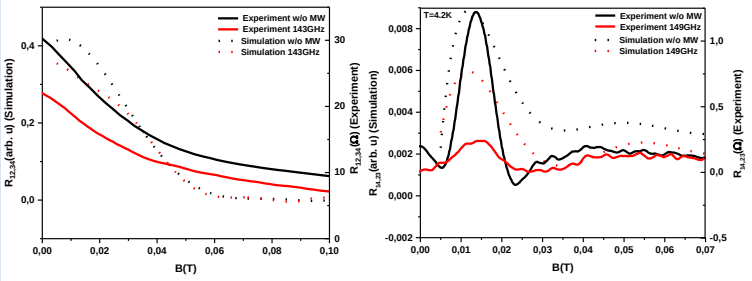

Poincare sections for the trajectories with different incidence angles w/o MW (left) and with MW 148GHz (righ) at B=0.013 T (max).

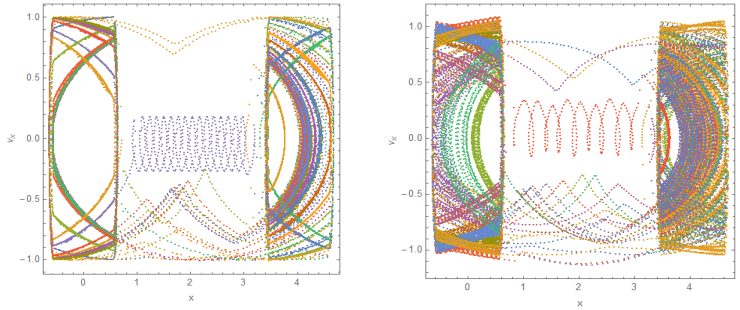

Conclusions

- MW suppress of local and non-local resistance
- Numerical simulations allow us to model observed behavior
- It's possible to extract geometry parameters based on comparison of experiment and simulated resistance
- Geometry of the structure influences on resistance frequency dependence

Acknowledgements

CAPES, CNPq, FAPESP

References

1. M. Büttiker, Y. Imry, R. Landauer and S. Pinhas, *PhysRevB*, **31**, *6207 (1985)*
2. M. Büttiker, *PhysRevLett*, **57**, *1761 (1986)*
3. A. D. Chepelianskii and D. L. Shepelyansky, *Phys.RevB.* **80**, *241308(R) (2009)*

III. Viscous electron flow in mesoscopic 2DEG

G. M. Gusev,[1,a] A. D. Levin,[1] E. V. Levinson,[1] and A. K. Bakarov[2,3]
[1]*Instituto de Física da Universidade de Sao Paulo, 135960-170 Sao Paulo, SP, Brazil*
[2]*Institute of Semiconductor Physics, Novosibirsk 630090, Russia*
[3]*Novosibirsk State University, Novosibirsk 630090, Russia*

(Received 27 December 2017; accepted 12 February 2018; published online 26 February 2018)

We report electrical and magneto transport measurements in mesoscopic size, two-dimensional (2D) electron gas in a GaAs quantum well. Remarkably, we find that the probe configuration and sample geometry strongly affects the temperature evolution of local resistance. We attribute all transport properties to the presence of hydrodynamic effects. Experimental results confirm the theoretically predicted significance of viscous flow in mesoscopic devices. https://doi.org/10.1063/1.5020763

In the last two decades, there has been considerable progress in the understanding of electron transport in micro and nanometer scaled systems. Successful fabrication of ballistic field-effect transistors requires a fundamental understanding of the mechanism of charge carrier transport. The commonly accepted mechanism for the transport properties is described semiclassically or by the Landauer-Buttiker formalism. Note, however, that these models are based on the assumption that the rate of momentum conserving scattering exceeds that of momentum relaxation scattering. It is important to look at different principles for a theory of transport. There has been increasing interest in the fabrication of devices with new types of functionality whose operation is determined by new principles. A remarkable possibility is the hydrodynamic regime of a Fermi liquid of electrons in a two-dimensional system, when the mean free path for electron-electron collisions l_{ee} is smaller than the mean free path with static defects and phonons l, and transport resembles a viscous electron fluid.[1–8] The viscosity contribution to the transport can be specially enhanced in a pipe-low set up, where the mean free path l_{ee} is much less than the sample width W, while $l >> W$. In such a hydrodynamic regime, the theory makes a number of dramatic predictions, for example, the resistivity is inversely proportional to the square of the temperature, $\rho \sim T^{-2}$, so-called "Gurzhi effect", and the square of the sample width $\rho \sim W^{-2}$.[1,2] This effect has not been experimentally observed until now, even where other signatures for hydrodynamics have been demonstrated. Conventional liquid Fermi theory predicts $\rho \sim T^2$, since quasiparticles near the Fermi surface scatter at a rate T^2.

In experiments, the viscous 2D electron transport has been examined in electrostatically defined GaAs wires using current heating technique.[9,10] Recently large negative magnetoresistance has been observed in high mobility 2D gas in GaAs macroscopic samples.[11,12] However, a significant portion of the attention in hydrodynamic effects has been dedicated to graphene for its very weak scattering against acoustic phonons, which allows for the realization of hydrodynamic flow at high temperatures. Indeed several theoretical predictions have been confirmed in high quality, encapsulated, single layer graphene: negative vicinity[13] resistances have been observed and successfully explained by vorticity generated in viscous flows.[14–17] Note, that such a dramatic experimental appearance of electron viscosity in nonlocal transport has not been accompanied by effects in longitudinal resistance and magnetotransport.

[a]Electronic address: gusev@if.usp.br

A series of updated theoretical approaches has been published recently,[18–21] providing additional possibilities to determine the viscosity from local and magnetotransport measurements, which require experimental verifications.

In the present paper, we have gathered all the requirements for observation of the hydrodynamic effect in a 2D electron system and present experimental results accompanied with quantitative analysis. For this purpose, we have chosen GaAs mesoscopic samples with high mobility 2D electron gas. The finding of previous studies[9–12] and theoretical approaches,[18–21] illustrate that it has become necessary to revisit electron transport in high quality GaAs systems. We employ commonly used longitudinal resistance and magnetoresistance to characterize electron shear viscosity, electron-electron scattering time, and reexamine electron transport over a certain temperature range 1.5-40 K. One particularly striking observation is the change in the sign of the resistance temperature dependence with changing current injection probe configuration. Moreover, we observe the "Gurzhi effect" in devices with H-bar geometry. The electron-electron scattering time and viscosity are extracted from transport measurements and its temperature dependence in a wide region of temperatures.

Our samples are high-quality, GaAs quantum wells with a width of 14 nm, high electron density $n_s \simeq 9.1 \times 10^{11}$ cm^{-2}, and a mobility of $\mu \simeq 2 \times 10^6$ cm^2/Vs at $T = 1.4$ K. We present experimental results on two different types of mesoscopic size devices, refereed to as Hall-bar and H-shaped bar, fabricated from the same wafer. The Hall bar is designed for multi-terminal measurements. The sample consists of three, $5\mu m$ wide consecutive segments of different length (10, 20, $10\mu m$), and 8 voltage probes. The four terminal, H-shaped bar consist of a $4 \times 10\mu m^2$ central channel between $5\mu m$ wide legs. The measurements were carried out in a VTI cryostat, using a conventional lock-in technique to measure the longitudinal R_{xx} resistance with an ac current of $0.1 - 1\mu A$ through the sample, which is sufficiently low to avoid overheating effects. Two Hall bars and 4 H-shaped devices from the same wafers have been studied. We also compare our results with transport properties of 2D electrons in a macroscopic sample.

Fig. 1 shows the longitudinal magnetoresistivity ρ_{xx} measured in local configuration for a H-bar sample as a function of magnetic field and temperature. One can see two characteristic features: a giant negative magnetoresistance ($\sim 400 - 1000\%$) and a pronounced temperature dependence of the zero field resistance. Surprisingly, the resistance decrease with temperature almost follows $\rho \sim T^{-2}$ dependence, as in the Gurzhi effect. Fig. 2 shows the longitudinal magnetoresistivity ρ_{xx} measured in local configuration for a Hall-bar sample as a function of magnetic field and temperature. Note, that we use a set up, where the current is injected through the system at a lateral contact (referred as C1 configuration), which resembles current flow in a H-bar sample. The magnetoresistance feature is qualitatively similar, although the decrease is not so rapid as in the H-bar. We also check the conventional set up, where current is injected through probe 1 to 4, and the voltage is measured between probes 2 and 3 (referred as C3 configuration) Strikingly, while in the viscous regime it is expected that electro-electron scattering time τ_{ee} behaves as $\propto T^{-2}$ in both set ups, resistance increases with T in the conventional measurement set up C3 and decreases with T in the set up where the current injection probes are positioned against the voltage probes C1. The results for the different schematic set ups in zero magnetic field are shown in Fig. 3. One can see that the temperature coefficient of resistance is strongly affected by probe configuration.

In mesoscopic samples, two transport regimes can be identified: ballistic and hydrodynamics. In order to distinguish the ballistic and hydrodynamic regimes more in depth analysis of the problem should be done. Significant temperature dependence of the value and shape of magnetoresistance and dependence on the probe configurations is inconsistent with dominant ballistic contribution.

We compare our results with previously published models.[18–20] A more advanced model, however, restricted by a zero magnetic field, consider both local and nonlocal transport in graphene.[17] The model is generic and can be applied to other material with a parabolic spectrum such as GaAs quantum wells. The resulting conductivity of 2D gas in constrained geometry is given by

$$\sigma = \sigma_0(1 - \mathcal{F}), \quad \mathcal{F} = 2\frac{D}{W\xi}\sinh\left(\frac{W}{2D}\right), \tag{1}$$

where $\sigma_0 = e^2 n\tau/m = 1/\rho_0$ is the Drude conductivity, τ is momentum relaxation time due to interaction with phonons and static defects, $D = \sqrt{\eta\tau_{ee}}$, $\xi = l_s \sinh(W/2D) + D\cosh(W/2D)$ is characteristic

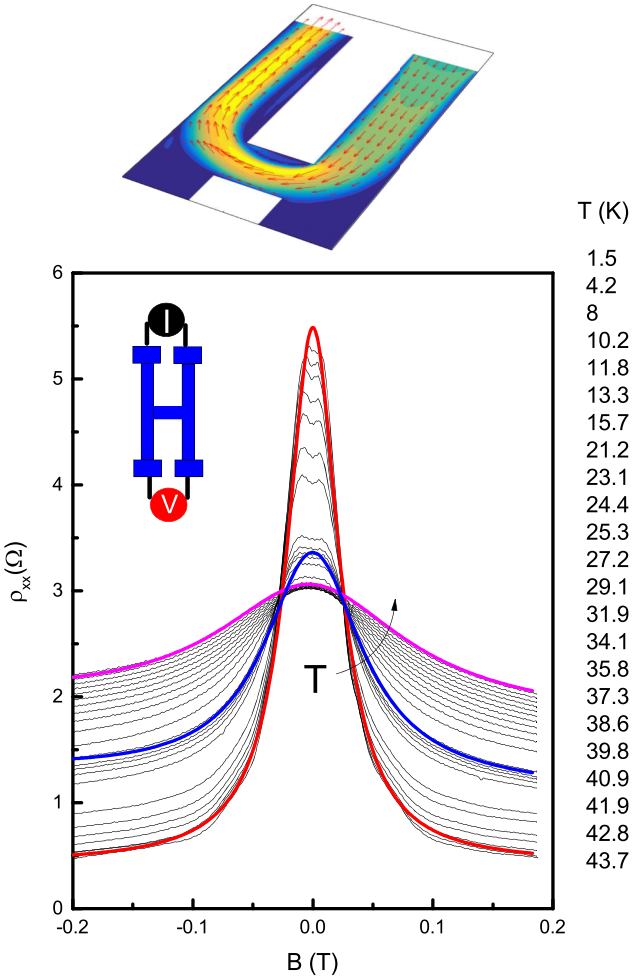

FIG. 1. Top- a sketch of the velocity flow profile for viscous flow in the experimental set up used in this study. Temperature dependent magnetoresistance of a GaAs quantum well in an H-bar sample. Thick curves are examples illustrating magnetoresistance calculated from Eqs. 1,2 in main text for different temperatures: 1.5 K (red), 27,2 K (blue) and 43,7 K (magenta). The schematics show how the current source and the voltmeter are connected for the measurements.

length which depends on the boundary slip length l_s. The boundary no-slip conditions correspond to the ideal hydrodynamic case of diffusive boundaries with $l_s = 0$, while the opposite limit (free surface boundary conditions) corresponds to the ideal ballistic case with $l_s = \infty$. Asymptotic limit (ideal hydrodynamic approach) $l_s = 0$ has been considered in Refs. 18 and 19 and extended to nonzero magnetic field. In this case, the conductivity (1) can be substituted by a simple interpolation formula

$$\rho = \rho_0 \frac{1}{1 - 2\frac{D}{W}\tanh(\frac{W}{2D})} \approx \rho_0 \left(\frac{1}{\tau} + \frac{1}{\tau^*}\right), \tag{2}$$

where the effective relaxation time is given by:[18–20]

$$\tau^* = \frac{W(W + 6l_s)}{12\eta} \tag{3}$$

$$\eta = \frac{1}{4} v_F^2 \tau_2. \tag{4}$$

$$\frac{1}{\tau_2(T)} = A_{ee}^{FL} \frac{T^2}{[ln(E_F/T)]^2} + \frac{1}{\tau_{2,0}} \tag{5}$$

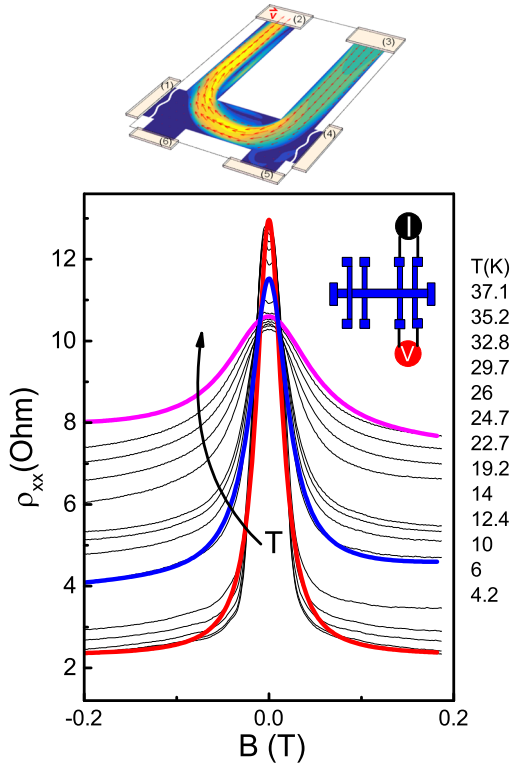

FIG. 2. Top- a sketch of the velocity flow profile for viscous flow in the experimental set up used in this study. Temperature dependent magnetoresistance of a GaAs quantum well in a Hall bar sample. Thick curves are examples illustrating magnetoresistance calculated from Eqs. 1,2 for different temperatures: 4.2 K (red), 19,2 K (blue) and 37,1 K (magenta). The schematics show how the current source and the voltmeter are connected for the measurements.

where the coefficient A_{ee}^{FL} be can expressed via the Landau interaction parameters ($A_{ee}^{FL} = 1.5 \times 10^{10} s^{-1} K^{-2}$), and $\tau_{2,0}$ is the scattering time from disorder.

Therefore, viscosity leads to incorporation of an extra relaxation mechanism, which contains the contribution from the electron-electron scattering time $\tau_{2,ee}(T)$ and temperature independent electron

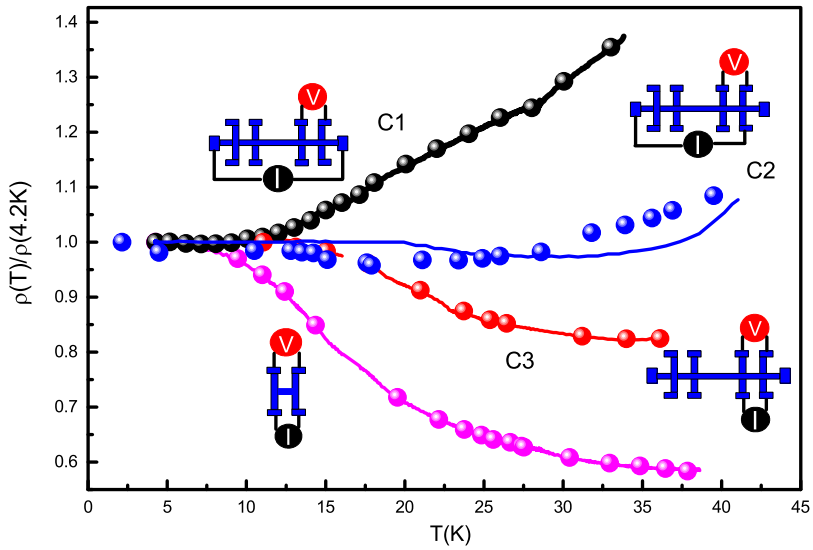

FIG. 3. Temperature dependent resistivity of a GaAs quantum well in a Hall bar and H-bar for different configurations in zero magnetic field. Circles show calculations from theoretical formula (1) with numerical parameters described in the main text.

scattering from disorder $\tau_{2,0}$.[18,19] In other words, the small ratio between relaxation of the second moment of electron distribution function and first moment $\tau^*/\tau = l_{2,\ ee}/l << 1$ corresponds to the dominant viscous contribution to resistivity. Such separation of the conductivity in two independent channels allows the introduction of the magnetic field dependent viscosity tensor and the derivation of magnetoresistivity:[18,19]

$$\rho_{xx} = \rho_0 \left(\frac{1}{\tau} + \frac{1}{\tau^*} \frac{1}{1 + (2\omega_c \tau_2)^2} \right). \tag{6}$$

We fit the magnetoresistance curves in Figs. 1 and 2 and resistance in zero magnetic field, shown in fig. 3, with the following fitting parameters: $\tau_{2,0} = 0.8 \times 10^{-11}$ s, $\tau_0 = 10^{-9} s$, $A_{ee}^{FL} = 1.5 \times 10^{10} s^{-1} K^{-2}$. We also find that in both microscopic and macroscopic samples $\frac{1}{\tau(T)} = A_{ph} T + \frac{1}{\tau_0}$ Assuming that the viscous effect is small in macroscopic samples, we can reduce the number of independent parameters by measuring $\rho_0(T) \sim 1/\tau(T)$ and extract A_{ph} independently. We find $A_{ph} = 10^9 s^{-1} K^{-1}$.

Fig. 4a shows the dependencies of $\tau_2(T)$ extracted from comparison with the theory. Indeed the electron-electron scattering time follows expected behaviour described by equation 5. The effective relaxation time τ^* is proportional to the second moment relaxation rate $\frac{1}{\tau_2}$ (not a time) and can be also compared with the theory, as we can see from eqs. 3 and 4. Note, however, that τ^* contains additional parameter -boundary slip length, which depends on the viscous flow conditions. We are able to reproduce the evolution of characteristic time with temperature, assuming that l_s depends on probe configuration. We find the value of l_s for corresponding set ups and sample geometries: $19 \mu m$ (C1), $14, 6 \mu m$ (C2), $6, 3 \mu m$ (H-bar). Although it could have been expected that all dependencies merge in a single curve, the curves show a tendency to collapse into one. The remaining misfitting may be related to temperature dependence of l_s. Therefore, the different sign of the temperature coefficient for different set ups is explained by the viscous flow conditions because of the decreasing of τ^* or l_s. It is worth noting that, the dependence of the boundary slip length on the probe configuration and

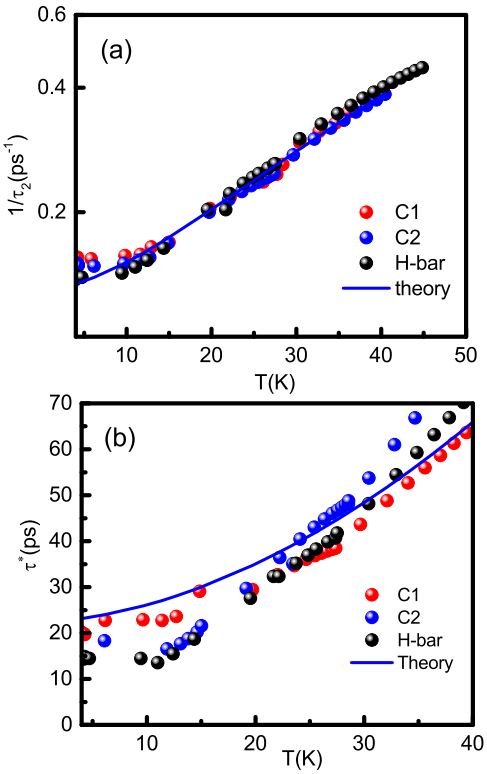

FIG. 4. (a) The relaxation time τ_2 as a function of the temperature obtained by fitting the theory with experimental results. The solid line is theory. (b) The relaxation time τ^* as a function of the temperature obtained by fitting the theory with experimental results. The solid line is theory with parameters presented in the main text.

geometry still requires further investigation. We modeled the Poiseuille flow for two dimensional situations depicted in Figs. 1 and 2 (top). We find that the velocity profile is strongly depends on the geometry and liquid flow injections. Calculation of potential distribution in a viscous charged liquid is a very challenging theoretical task and is out of the scope of the present experimental work. Note, however, that more advanced consideration predicts that diffusive scattering on the rough edge and inhomogeneity of the velocity field due to geometry may result in a similar effect.[18] In this case $\tau^* \sim d^2/\eta$, where d is the characteristic period of static defects or velocity inhomogeneity.[18]

In conclusion, we have measured the evolution of several magnetotransport characteristics in high quality GaAs quantum wells with temperature. In order to fulfill requirements for a hydrodynamic regime, we use mesoscopic samples, where very recently numerous different predictions have been made.[18–21] These results open up possibilities to control the current flow in microstructures by variation of the viscosity and manipulation of the fluids at a micro and nanoscale, developing new microtechnologies.

We thank Z. D. Kvon for helpful discussions. The financial support of this work by FAPESP, CNPq (Brazilian agencies) is acknowledged.

[1] R. N. Gurzhi, Sov. Phys. Usp. **11**, 255 (1968); R. N. Gurzhi, A. N. Kalinenko, and A. I. Kopeliovich, Phys. Rev. Lett. **74**, 3872 (1995).
[2] M. Dyakonov and M. Shur, Phys. Rev. Lett. **71**, 2465 (1993).
[3] M. I. Dyakonov and M. S. Shur, Phys. Rev. B **51**, 14341 (1995).
[4] M. Dyakonov and M. Shur, IEEE Trans. Electron Devices **43**, 380 (1996).
[5] A. O. Govorov and J. J. Heremans, Phys. Rev. Lett. **92**, 026803 (2004).
[6] R. Bistritzer and A. H. MacDonald, Phys. Rev. B **80**, 085109 (2009).
[7] A. V. Andreev, S. A. Kivelson, and B. Spivak, Phys. Rev. Lett. **106**, 256804 (2011).
[8] B. N. Narozhny, I. V. Gornyi, M. Titov, M. Schutt, and A. D. Mirlin, Phys. Rev. B **91**, 035414 (2015).
[9] L. W. Molenkamp and M. J. M. de Jong, Solid-State Electron. **37**, 551 (1994).
[10] M. J. M. de Jong and L. W. Molenkamp, Phys. Rev. B **51**, 13389 (1995).
[11] Q. Shi, P. D. Martin, Q. A. Ebner, M. A. Zudov, L. N. Pfeiffer, and K. W. West, Phys. Rev. B **89**, 201301(R) (2014).
[12] L. Bockhorn, P. Barthold, D. Schuh, W. Wegscheider, and R. J. Haug, Phys. Rev. B **83**, 113301 (2011).
[13] D. A. Bandurin, I. Torre, R. Krishna Kumar, M. Ben Shalom, A. Tomadin, A. Principi, G. H. Auton, E. Khestanova, K. S. Novoselov, I. V. Grigorieva, L. A. Ponomarenko, A. K. Geim, and M. Polini, Science **351**, 1055 (2016).
[14] L. Bockhorn, P. Barthold, D. Schuh, W. Wegscheider, and R. J. Haug, Phys. Rev. B **83**, 113301 (2011).
[15] L. Levitov and G. Falkovich, Nature Physics **12**, 672 (2016).
[16] G. Falkovich and L. Levitov, Phys. Rev. Lett. **119**, 066601 (2017).
[17] I. Torre, A. Tomadin, A. K. Geim, and M. Polini, Phys. Rev. B **92**, 165433 (2015).
[18] P. S. Alekseev, Phys. Rev. Lett. **117**, 166601 (2016).
[19] T. Scaffidi, N. Nandi, B. Schmidt, A. P. Mackenzie, and J. E. Moore, Phys. Rev. Lett. **118**, 226601 (2017).
[20] L. V. Delacretaz and A. Gromov, Phys. Rev. Lett. **119**, 226602 (2017).
[21] F. M. D. Pellegrino, I. Torre, and M. Polini, Phys. Rev. B **96**, 195401 (2017).

IV. Vorticity-induced negative nonlocal resistance in a viscous 2DES

A. D. Levin,[1] G. M. Gusev,[1] E. V. Levinson,[1] Z. D. Kvon,[2,3] and A. K. Bakarov[2,3]
[1]*Instituto de Física da Universidade de São Paulo, 135960-170, São Paulo, SP, Brazil*
[2]*Institute of Semiconductor Physics, Novosibirsk 630090, Russia*
[3]*Novosibirsk State University, Novosibirsk 630090, Russia*

(Received 10 April 2018; revised manuscript received 6 June 2018; published 25 June 2018)

We report nonlocal electrical measurements in a mesoscopic size two-dimensional (2D) electron gas in a GaAs quantum well in a hydrodynamic regime. Viscous electric flow is expected to be dominant when electron-electron collisions occur more often than the impurity or phonon scattering events. We observe a negative nonlocal resistance and attribute it to the formation of whirlpools in the electron flow. We use the different nonlocal transport geometries and compare the results with a theory demonstrating the significance of hydrodynamics in mesoscopic samples.

DOI: 10.1103/PhysRevB.97.245308

I. INTRODUCTION

It is generally believed that, in the absence of disorder, a many-body electron system resembles the viscous flow. Hydrodynamic characteristics can be specially enhanced in a pipe flow setup, where the mean free path for electron-electron collision l_{ee} is much shorter than the sample width W, while the mean free path due to impurity and phonon scattering l is larger than W. Viscosity is characterized by momentum relaxation in the fluid and, in narrow samples, occurs at the sample boundary. Calculation of the shear viscosity η is a difficult task because it requires knowledge of particle interactions on the scale of l [1].

It has been predicted that the resistivity of metals in the hydrodynamic regime is proportional to electron shear viscosity $\eta = \frac{1}{4} v_F^2 \tau_{ee}$, where v_F is the Fermi velocity and τ_{ee} is the electron-electron scattering time $\tau_{ee} = l_{ee}/v_F$ [2–6]. This dependency could lead to interesting properties. For example, resistance decreases with the square of temperature $\rho \sim \eta \sim \tau_{ee} \sim T^{-2}$, the so called Gurzhi effect, and with the square of sample width $\rho \sim W^{-2}$. The negative differential resistance has been observed previously in GaAs wires, which has been interpreted as the Gurzhi effect due to heating by the current [7]. A remarkable manifestation of the hydrodynamic effect is a swirling feature in the flow field, referred to as a vortex. The vorticity can drive the current against an applied electric field and generate backflow near the current injection region, which can be detected in the experiment as a negative voltage drop [8]. A different transport measurement setup has been proposed for the identification of viscosity related features in the hydrodynamic regime [8–11].

When fluid flows along a pipe, a quadratical velocity profile is formed, which leads to the Gurzhi effect, and can be detected from the anomalous temperature and sample width dependence, as is mentioned above. For illustration we modeled the Poiseuille flow for a two-dimensional neutral fluid. Figure 1(a) shows the configuration, which has been proposed in [8], and where the current is injected across the sample between vertical probes. In this geometry, one can see the vortex or whirlpools in the liquid flow outside of the main current path. As a consequence, for an electronic fluid, a negative voltage drop occurs across the strip in close proximity to the current probes. Figure 1(b) illustrates the nonlocal, vicinity transport geometry, where the current is injected in the left lateral and bottom contacts, while the voltage drop occurs near the current injection region. This geometry has been proposed in [9–11], and the model clearly demonstrates the formation of whirlpools in the hydrodynamic flow, yielding a negative nonlocal signal in transport measurements [11]. Note that the swirling features can be observed only in the nonlocal configuration.

The nonlocal vicinity effect has been studied experimentally in an ultraclean graphene sheet [11]. It has been demonstrated that the nonlocal signal undergoes a sign change from positive, at low temperatures, to negative, above elevated temperatures, that is associated with whirlpool emergence in the hydrodynamic regime. Near room temperature, the signal again undergoes a sign change because the Ohmic contribution starts to dominate the vicinity response at high T. Note that such dramatic experimental appearance of hydrodynamic features in nonlocal transport has not been accompanied by observation of the Gurzhi effect in local transport. Moreover, the transversal nonlocal geometry (Fig. 1) has not been studied experimentally with respect to possible vorticity effects. Other materials, such as GaAs quantum wells, have a particular interest because they possess the highest mobility over wide temperature ranges. It is also worthwhile to extend the theoretical approach [8–11] to a two-dimensional electron in GaAs with a parabolic energy spectrum, which is different from the linear spectrum in graphene.

A series of updated theoretical approaches has been published recently [12–15], providing additional possibilities to determine the viscosity from magnetotransport measurements, which can be used for comparison with nonlocal measurements.

In this study we measure the nonlocal resistance in mesoscopic GaAs quantum well systems. We determine all relevant electron viscous parameters from the longitudinal magnetoresistance in a wide temperature range, which provides an estimate of the nonlocal signal, and compare it with

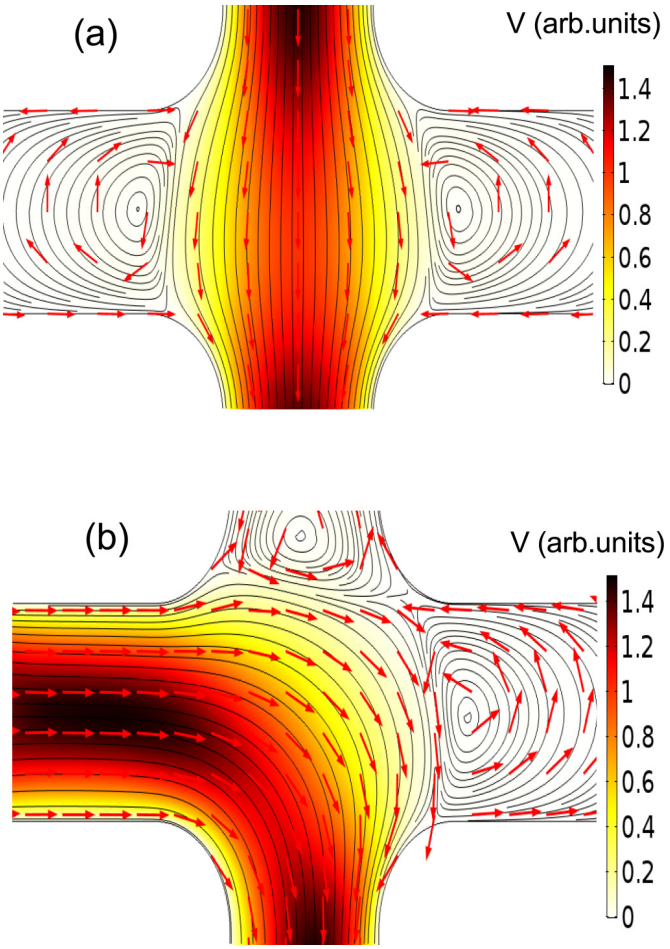

FIG. 1. Sketch of the different transport setup measurements, showing a velocity flow profile. (a) Nonlocal transport setup, proposed in [8]. (b) Nonlocal (vicinity) transport setup, proposed in [8–11].

experimental results. A good qualitative agreement between experimental and simulated data has been obtained.

II. NEGATIVE GIANT MAGNETORESISTANCE, EXPERIMENT, AND DISCUSSION

Our samples are high-quality, GaAs quantum wells with a width of 14 nm. Parameters characterizing the electron system are given in Table I. We present experimental results on Hall-bar devices designed in two different configurations. Design I consists of three 5 μm wide consecutive segments of different length (10, 20, 10 μm), and eight voltage probes. Figure 2(top) shows the image of a typical multiprobe Hall device I. Design II is also a Hall bar with three 2 μm wide

TABLE I. Parameters of the electron system in a mesoscopic samples at $T = 1.4$ K. Parameters are defined in the text.

W (μm)	n_s (10^{11} cm^2)	v_F (10^7 cm/s)	l (μm)	l_2 (μm)	η (m^2/s)
5	9.1	4.1	40	2.8	0.3
2	6.0	3.3	20.6	1.4	0.12

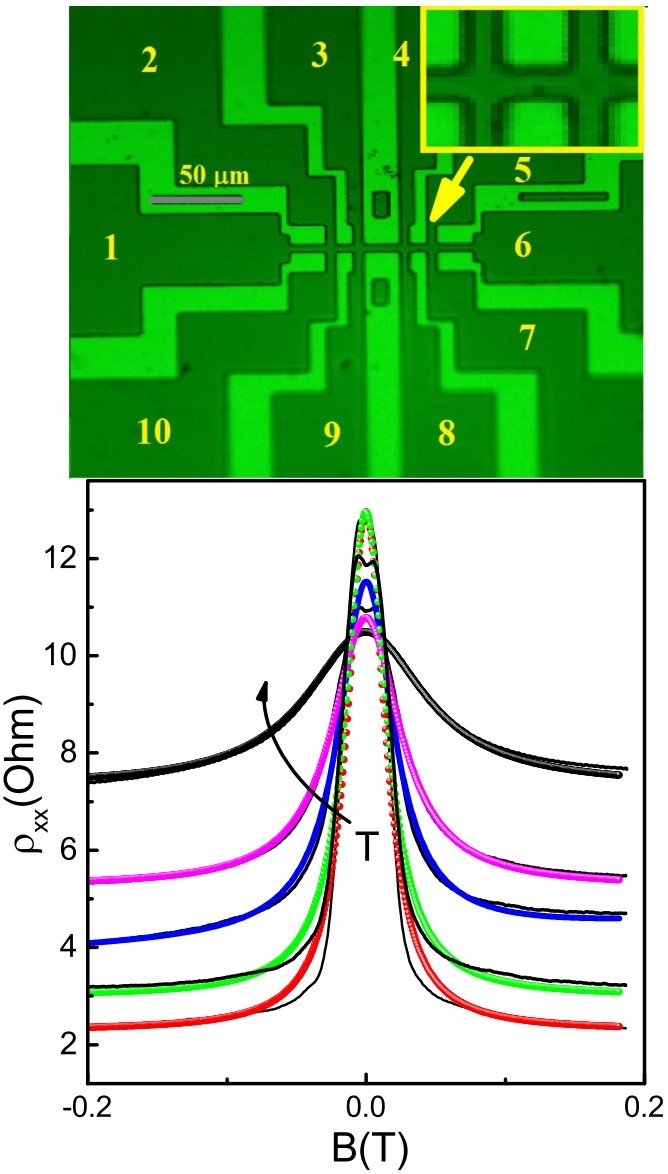

FIG. 2. Top: Image of the Hall-bar device. Top right: Zoomed Hall-bar bridge. Temperature dependent magnetoresistance of a GaAs quantum well in a Hall bar sample $W = 5$ μm. Thick lines are examples illustrating magnetoresistance calculated from Eqs. (1) and (2) for different temperatures: 4.2 K (red), 14 K (green), 19 K (blue), 26 K (magenta), and 37.1 K (black).

consecutive segments of different length (2, 7, 2 μm), and eight voltage probes. The measurements were carried out in a VTI cryostat, using a conventional lock-in technique to measure the longitudinal ρ_{xx} resistivity with an ac current of 0.1–1 μA through the sample, which is sufficiently low to avoid overheating effects. Five Hall bars from two different wafers were studied.

Longitudinal magnetoresistance has been studied in previous research for different configurations of the current and voltage probes [16]. Before analyzing the nonlocal effect and in order to make this analysis more complete, we present the results of measurements of the longitudinal magnetoresistivity $\rho_{xx}(B)$. Figure 2(a) shows $\rho_{xx}(B)$ as a function of magnetic field and temperature. One can see two characteristic

features: a giant negative magnetoresistance (∼400%–600%) with a Lorentzian-like shape, and a pronounced temperature dependence on zero field resistance. In the hydrodynamic approach, the semiclassical treatment of the transport describes the motion of carriers when the higher order moments of the distribution function are taken into account. The momentum relaxation rate $1/\tau$ is determined by electron interaction with phonons and static defects (boundary). The second moment relaxation rate $1/\tau_{2,ee}$ leads to the viscosity and contains the contribution from the electron-electron scattering and temperature independent scattering by disorder [12,13]. It has been shown that conductivity obeys the additive relation and is determined by two independent *parallel* channels: the first is due to momentum relaxation time and the second due to viscosity [12,13]. This approach allows the introduction of the magnetic field dependent viscosity tensor and the derivation of the magnetoresisivity tensor [12–15]:

$$\rho_{xx} = \rho_0^{\text{bulk}}\left(1 + \frac{\tau}{\tau^*}\frac{1}{1+(2\omega_c\tau_{2,ee})^2}\right), \tag{1}$$

where $\rho_0^{\text{bulk}} = m/ne^2\tau$, $\tau^* = \frac{W(W+6l_s)}{12\eta}$, viscosity $\eta = \frac{1}{4}v_F^2\tau_{2,ee}$.

We also collect the equations for relaxation rates separately:

$$\frac{1}{\tau_{2,ee}(T)} = A_{ee}^{FL}\frac{T^2}{[\ln(E_F/T)]^2} + \frac{1}{\tau_{2,0}}, \tag{2}$$

where E_F is the Fermi energy, and the coefficient A_{ee}^{FL} be can expressed via the Landau interaction parameter, however, it is difficult to calculate quantitatively (see discussion in [12]). The relaxation rate $\frac{1}{\tau_{2,0}}$ is not related to the electron-electron collisions, since any process responsible for relaxation of the second moment of the distribution function, even scattering by static defect, gives rise to viscosity [12]. A logarithmic factor is also present in the expression for quantum lifetime of weakly interacting 2D gas due to electron-electron scattering [17]:

$$\frac{\hbar}{\tau_{0,ee}(T)} = A_{ee}^{0}\frac{T^2[\ln(2E_F/T)]}{E_F} + \frac{\hbar}{\tau_{2,0}}, \tag{3}$$

where A_{ee}^0 is a numerical constant of the order of unity. Note, however, that since the relaxation time $\tau_{0,ee}$ is related to the kinematic of the electron-electron collisions, Expression (2) is more convenient and it is preferable to use. Finally, it has been shown that due to the disorder assisted contribution to the relaxation rate of the second moment of the distribution function, the expression is rewritten as

$$\frac{1}{\tau_{2,ee}^{da}(T)} = A_{ee}^{da}T^2 + \frac{1}{\tau_{2,0}}, \tag{4}$$

where the coefficient A_{ee}^{da} depends on the disorder type and its strength [12]. The moment relaxation rate is expressed as

$$\frac{1}{\tau} = A_{\text{ph}}T + \frac{1}{\tau_0}, \tag{5}$$

where A_{ph} is the term responsible for the phonon scattering [18,19], and $\frac{1}{\tau_0}$ is the scattering rate due to static disorder (not related to the second moment relaxation rate $\frac{1}{\tau_{2,0}}$).

We fit the magnetoresistance curves in Fig. 2 and the resistance in zero magnetic field with the three fitting parameters: $\tau(T)$, $\tau^*(T)$, and $\tau_{2,ee}(T)$. Figure 3 shows the dependencies of $1/\tau_{2,ee}(T)$ extracted from the comparison of the magnetoresistance shown in Fig. 2 and Eq. (1). We compare the temperature dependence of $\frac{1}{\tau_{2,ee}(T)}$ with theoretical predictions given by Eqs. (2)–(4) and present the results of such comparison in Fig. 3. The following parameters are extracted: $1/\tau_{2,0} = 1.45\times10^{11}$ s, $A_{ee}^{FL} = 0.9\times10^9$ s^{-1} K^{-2}, $A_{ee}^0 = 1.3$, $A_{ee}^{da} = 2.0\times10^{10}$ s^{-1} K^{-2}. All theoretical curves demonstrate reasonable agreement within experimental uncertainty. Hence, these mechanisms lead to nearly equivalent results and cannot be unambiguously distinguished based only on the temperature dependence of the relaxation time. Note that analysis of the nonlocal effect, considered below, does not depend on the relaxation mechanism.

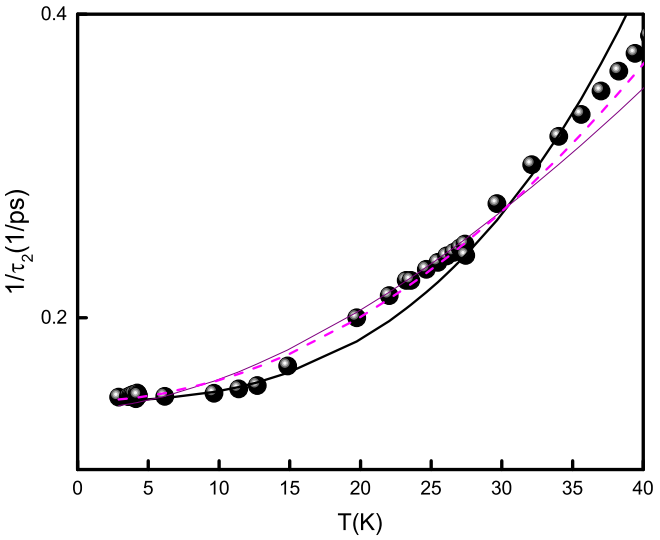

FIG. 3. Relaxation rate $1/\tau_2$ as a function of the temperature obtained by fitting the theory with experimental results $W = 5$ μm. Thick black line is Eq. (2), thin black line is Eq. (3), dashes are Eq. (4).

In addition, we extract the temperature dependence of the moment scattering rate and determine parameters $A_{\text{ph}} = 10^9$ s K^{-1} and $\tau_0 = 5\times10^{-10}$ s, which are correlated with previous studies [17,18]. Relaxation time $\tau^*(T)$ depends on the $\tau_{2,ee}(T)$ and boundary slip length l_s. Comparing these values, we find that $l_s = 3.2$ μm $< L$, and, therefore, in our case, it is appropriate to use diffusive boundary conditions. Table I shows the mean free paths $l = v_F\tau$, $l_2 = v_F\tau_{2,ee}$, and viscosity, calculated with parameters extracted from the fit of experimental data.

III. EXPERIMENT: NONLOCAL RESISTANCE

In this section we focus on the nonlocal configurations because such geometry facilitates the observation of current whirlpools. Figure 4 shows the transport in a nonlocal setup, where the current is injected across the strip between probes 4 and 8. The voltage drop is measured between probes 5 and 7. Below we refer to it as C1 configuration. Poiseuille flow for a two-dimensional liquid is presented in Fig. 1(a). Note, however, that 2D charged liquid displays pronounced ballistic transport behavior. One can see strong oscillations

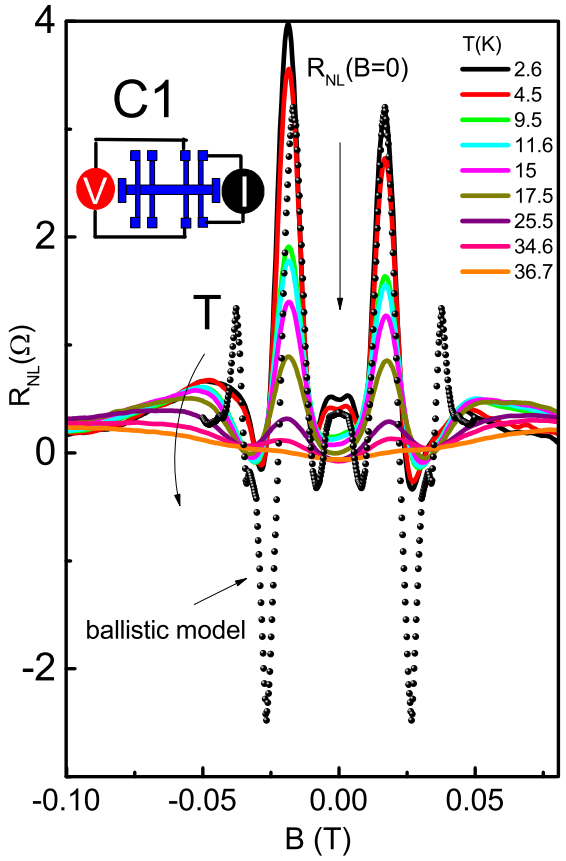

FIG. 4. Nonlocal transport signal versus magnetic field for different temperatures $W = 5$ μm. The dots represent results for the billiard model.

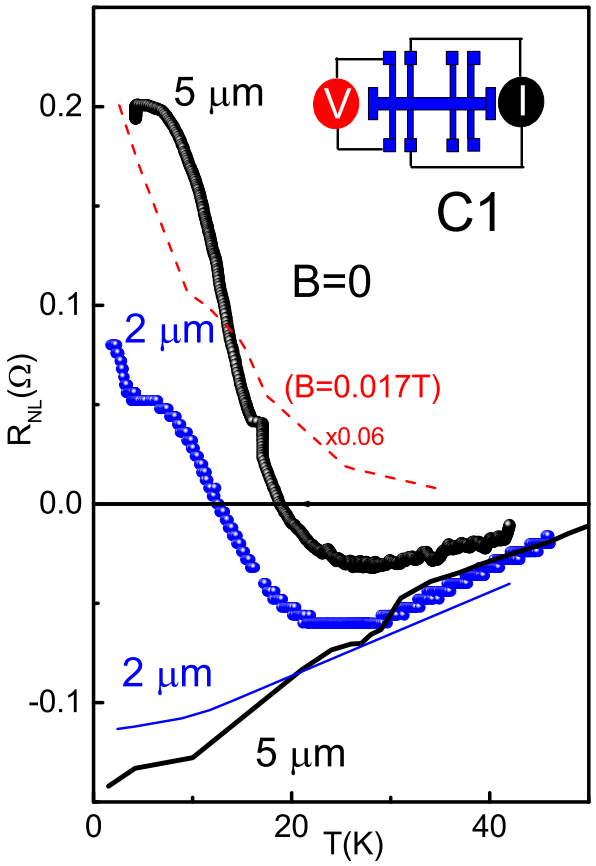

FIG. 5. T dependence of the nonlocal signal for different sample configuration. Solid lines show the calculations from Eq. (6) for $x = 10$ μm ($W = 5$ μm) and $x = 5$ μm ($W = 2$ μm). Dashes: T dependence of the ballistic peak at $B = 0.017T$.

in weak magnetic fields due to geometrical resonance effects considered in the semiclassical billiard model [20,21]. We perform numerical simulations of the electron trajectories in ballistic structures. The results of theses simulations (black dots) are compared to the experimental data. We observe an agreement with experimental data only at low magnetic field. Although the position of the resistance peaks at higher magnetic field coincide with calculations, the negative peak has a much smaller value, and the positive peak is wider than that obtained from the billiard model. Figure 4 also shows the evolution of the nonlocal magnetoresistance with temperature. One can see that all oscillations are smeared out by temperature and magnetoresistance at high temperature has a parabolic shape. Remarkably, the nonlocal resistance at $B = 0$ is positive at low temperatures, in accordance with the billiard model calculations, and then it changes sign and becomes negative at higher temperatures (Fig. 5). Figure 6 shows the transport in a nonlocal setup, where the current is injected between probes 1 and 8 and the voltage is measured between probes 5 and 6 (referred to as configuration C2). The Poiseuille flow for a two-dimensional liquid is presented in Fig. 1(b). As in configuration C1, one can see strong oscillations due to the geometrical resonance effect. Note that the ballistic transport in this configuration is very well established and studied previously in numerous publications [20,21]. In cross junction geometry, it was denominated as bend resistance [21]. We also perform the classical simulations for the transport in configuration C2, and the results are displayed in Fig. 6. Note, however, that in contrast to configuration C1, the bend resistance reveals a strong negative resistance peak near zero magnetic field [21,22]. This peak may mask the negative nonlocal signal due to viscosity, and detailed comparison is required to examine the significance of the hydrodynamic effect at low and high temperatures. Figure 7 presents the results of the nonlocal resistance temperature measurements in configuration C2 in zero magnetic field. One can see that the signal dramatically drops to zero in the $W = 5$ μm sample, and resistance changes sign at high temperature in the $W = 2$ μm sample. We also used a similar voltage measurement setup, where the current is injected between probes 1 and 8 and the voltage is measured between probes 4 and 5 (referred to as configuration C3). The nonlocal resistance in configuration C3 at zero magnetic field is shown in Fig. 7 for both samples designs.

IV. THEORY AND DISCUSSION

As has been shown in the previous section the viscosity leads to the incorporation of an extra relaxation mechanism [12–15] in zero magnetic field: $\rho = \rho_0^{\text{bulk}}(1 + \frac{\tau}{\tau^*})$. The dominant viscous contribution to resistivity corresponds to the small ratio between relaxation of the second moment of the electron distribution function and the first moment $\tau^*/\tau \ll 1$.

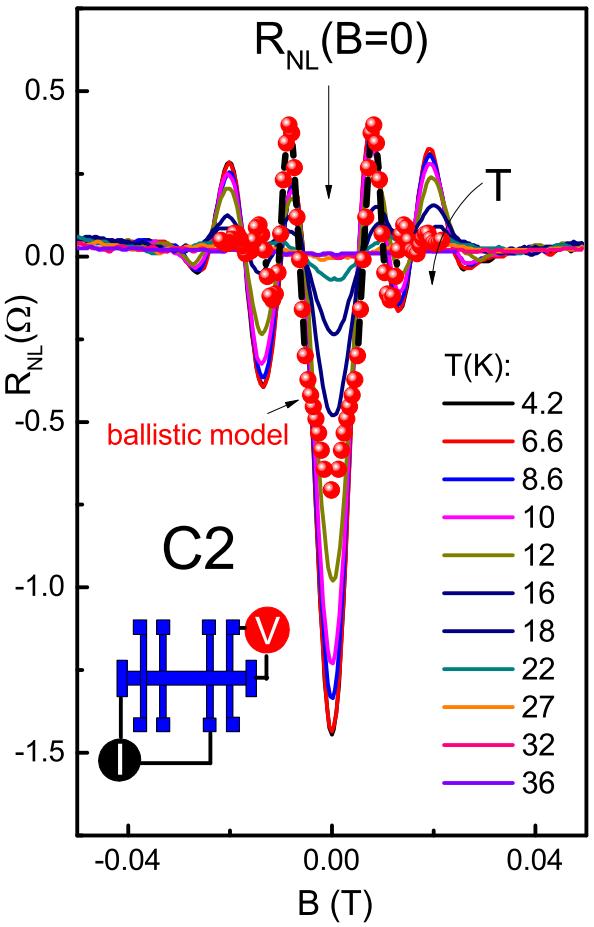

FIG. 6. Nonlocal transport signal versus magnetic field for different temperatures $W = 5\ \mu$m. The dots represent results for the billiard model.

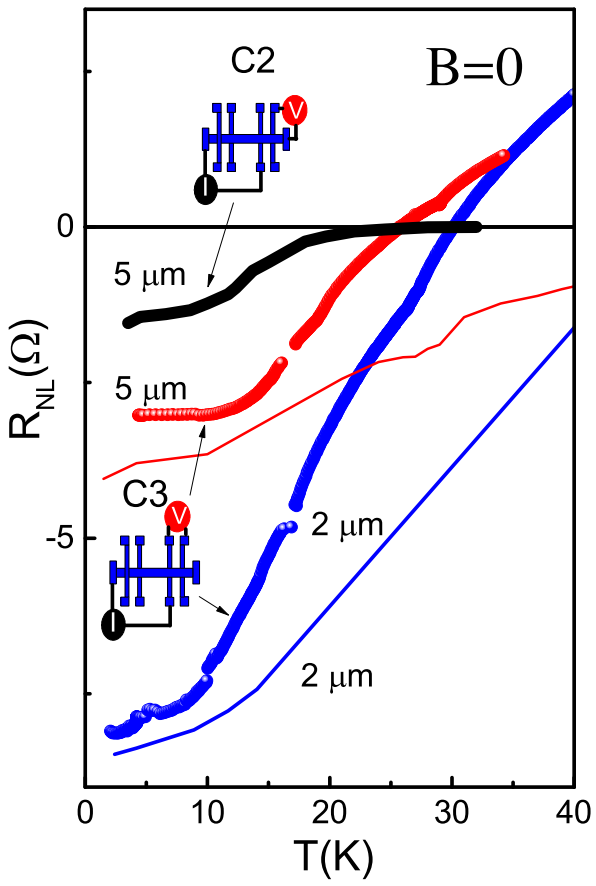

FIG. 7. T dependence of the nonlocal signal for different sample configurations. Thin solid lines show the calculations from Eq. (7) for $x = 3\ \mu$m ($W = 5\ \mu$m) and $x = 1.5\ \mu$m ($W = 2\ \mu$m).

Comparative analysis between nonlocal geometries C1 and C2 demonstrates a qualitative difference. Crucially, the experimental observation of swirling features depends on the parameters that affect the spacial distribution of the two-dimensional potential inside the viscous charge flow. The first parameter is the boundary slip length l_s. The boundary no-slip conditions correspond to the ideal hydrodynamic case of diffusive boundaries with $l_s = 0$. It has been shown that the negative nonlocal signal is robust to boundary conditions [10]. For example, the Gurzhi effect disappears for free surface boundary conditions ($l_s = \infty$), while whirlpools in hydrodynamic electron flow, and the resulting negative nonlocal response, do exist. The second parameter which drastically affects whirlpool behavior is the vorticity diffusion length $D_\eta = \sqrt{\eta\tau}$. Figure 8 represents the temperature dependence of characteristic lengths in a $W = 5\ \mu$m sample. Previous studies have not investigated whether typically developed current whirlpools show sensitivity to the geometry and confinement effect [8–10]. However, the careful inspection of theoretical results [9] reveals that geometry C1 exhibits the occurrence of whirlpools only above the threshold value of $D_\eta = 0.225W$ (Fig. 8). The vicinity geometry C2, which is shown in Fig. 1(b), by contrast, allows the formation of current whirlpools for arbitrary small values of D_η, but only in very close proximity to the current injector probe [10]. However, the value of D_η affects the spatial extension of the whirlpools, therefore, a high viscosity system facilitates observation of the negative vicinity resistance for a voltage detector placed at a large distance from the current injection probe. Moreover, the ballistic effect may induce the negative vicinity signal [19] and, therefore, requires more careful qualitative analysis. In the previous section we show the temperature dependence of low field magnetoresistance as well as the electrical resistivity over a temperature range extending from 1.7 to 40 K and obtain variation of the viscosity time with temperature. We use this data to estimate the nonlocal signal in our samples. The models [8–10] predict negative nonlocal resistance in configuration C1 at the distance $\overline{x} = \pi x/W$ from the main current path in the limits of free surface boundary conditions ($l_s = \infty$) in zero magnetic field:

$$R_{\rm NL}^{\rm C1} = -\rho_0 \left\{ \frac{\ln[\tanh^2(\overline{x}/2)]}{\pi} + 4\pi \left(\frac{D_\nu}{W}\right)^2 \frac{\cosh(\overline{x})}{\sinh^2(\overline{x})} \right\}. \quad (6)$$

In contrast to configuration C1, the results for vicinity geometry can be simplified only in the limit where the distance between the current injection probe is infinite:

$$R_{\rm NL}^{\rm C2} = -\frac{\rho_0}{2} \left\{ \frac{\ln[4\mathcal{T}]}{\pi} - \frac{\overline{x}}{W} + \pi \left(\frac{D_\nu}{W}\right)^2 \frac{1}{\mathcal{T}} \right\}, \quad (7)$$

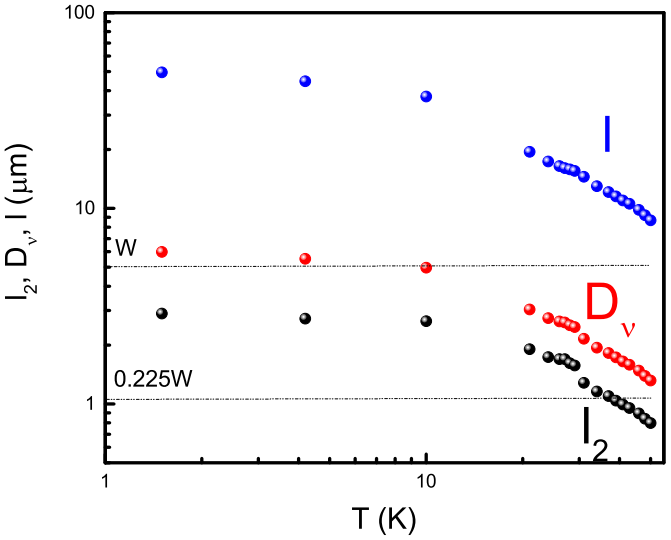

FIG. 8. The characteristic parameters as a function of the temperature for the sample with width $W = 5\ \mu$m. The whirlpool threshold is indicated by the dashes.

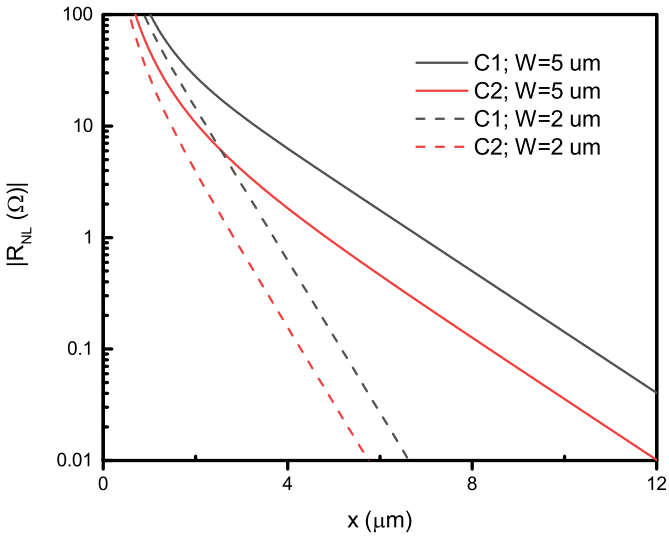

FIG. 9. The absolute value of the nonlocal resistance for two configurations as a function of the distance from the injector electrode $T = 4.2$ K, parameters are determined from local magnetoresistance measurements.

where $\mathcal{T} = \sinh^2(\overline{x}/2)$. Figure 9 shows the nonlocal resistances in both configurations as a function of distance between voltage probe and current injector $\overline{x}$ calculated from Eqs. (6) and (7) with parameters independently extracted from the local magnetoresistance measurements at $T = 4.2$ K. For visualization of the data in the negative range, we used an absolute log scale. We observe that the magnitudes of nonlocal signals exhibit a universally exponential decay with distance from the current injector. Note that the nonlocal resistance is much stronger for geometry C1. The advantage of configuration C1 is that the ballistic contribution is positive and, therefore, it can be unambiguously discriminated from the negative viscous contribution. The calculated temperature dependence of $R_{\rm NL}^{\rm C1}$ is shown in Fig. 5 for $x = 10\ \mu$m ($W = 5\ \mu$m) and $x = 5\ \mu$m ($W = 2\ \mu$m), which roughly correspond to the distance between the center of the probes. Note that the ballistic contribution to the transport also depends on the temperature due to the thermal broadening of the Fermi distribution function and scattering by the phonons. A rough estimate of the nonlocal ballistic resistance temperature dependence for $L < l$ may be obtained using the formula $R_{\rm NL} \sim \exp(-L/l)$, where L is the distance between probes [23]. Figure 5 shows the T dependence of the ballistic peak at $B = 0.017T$. One can see a rapid decrease of the peak with temperature. Therefore, the negative nonlocal resistance in zero field and at high temperature can be attributed only to hydrodynamic effects.

We also compare predictions for configurations C2 and C3 with experimental results. Note that we normalized ballistic resistance for the peak value at $B = 0.008T$ (Fig. 6), which we found more reliable, since this peak weakly depends on the boundary conditions and sample geometry [20]. The residual contribution at zero magnetic field could be due to viscous effects. In general, the ballistic contribution alone can explain the temperature dependence in zero field, below 20 K, without taking into account the viscous term. Above $T = 20$ K, ballistic contribution should be exponentially small (see Fig. 5).

Figure 7 shows the calculations from Eq. (7). Note that the analytical formula has been derived under several assumptions and we can apply the formula just for the evaluation of the upper limits of the signal. Figure 7 presents the results of such calculations. One can see that the predicted signal agrees with experimental data for $x = 3\ \mu$m ($W = 5\ \mu$m) and $x = 1.5\ \mu$m ($W = 2\ \mu$m), which roughly correspond to the distance between the centers of the probes. Note that, in a realistic sample, the width of the probes is comparable with the sample width W, while the theory considers $x \ll W$, also indicating the approximate character of the calculation. We may conclude here that geometry C1 exhibits a direct relation between the negative signal and formation of the current whirlpools. In geometries C2 and C3, negative nonlocal resistance follows the hydrodynamic predictions up to 30 K, however, it is very likely that the ballistic contribution is comparable or bigger than the hydrodynamic one at low temperatures. Above 30 K we observe a positive signal, which disagrees with both ballistic and hydrodynamic predictions. We attribute this behavior to approaching the condition $D_\eta = 0.225W$. Note that the observation of negative vicinity nonlocal resistance in graphene [11] requires more careful inspection of the ballistic contribution. Moreover, the condition $D_\eta = 0.225W$ is not fully completed (see also discussion in [10]), therefore, our observation of the negative nonlocal resistance in geometry C1 provides more clear evidence of current vortices. It is important to note that the transport signatures of the viscosity in the nonlocal effect are correlated in our samples with other observations, such as a giant longitudinal magnetoresistance and the Gurzhi effect [16].

V. SUMMARY AND CONCLUSIONS

In conclusion, we have studied nonlocal transport in a mesoscopic two-dimensional electron system in terms of viscosity of the fluids. In contrast to the Ohmic flow of the

particles, viscous flow can result in a backflow of the current and negative nonlocal voltage. We have measured voltage in different arrangements of current and voltage contacts and found a negative response, which we attributed to the formation of current whirlpools. Nonlocal viscosity-induced transport is strongly correlated with observations of the Gurzhi effect and low magnetic field transport described by hydrodynamic theory.

ACKNOWLEDGMENTS

The financial support of this work by the Russian Science Foundation (Grant No.16-12-10041), FAPESP (Brazil), and CNPq (Brazil) is acknowledged.

[1] S. Conti and G. Vignale, Phys. Rev. B **60**, 7966 (1999).
[2] R. N. Gurzhi, Sov. Phys. Usp. **11**, 255 (1968); R. N. Gurzhi, A. N. Kalinenko, and A. I. Kopeliovich, Phys. Rev. Lett. **74**, 3872 (1995).
[3] M. Dyakonov and M. Shur, Phys. Rev. Lett. **71**, 2465 (1993).
[4] M. I. Dyakonov and M. S. Shur, Phys. Rev. B **51**, 14341 (1995).
[5] M. Dyakonov and M. Shur, IEEE Trans. Electron Devices **43**, 380 (1996).
[6] A. O. Govorov and J. J. Heremans, Phys. Rev. Lett. **92**, 026803 (2004).
[7] L. W. Molenkamp and M. J. M. de Jong, Solid-State Electron. **37**, 551 (1994); M. J. M. de Jong and L. W. Molenkamp, Phys. Rev. B **51**, 13389 (1995).
[8] L. Levitov and G. Falkovich, Nat. Phys. **12**, 672 (2016).
[9] I. Torre, A. Tomadin, A. K. Geim, and M. Polini, Phys. Rev. B **92**, 165433 (2015).
[10] F. M. D. Pellegrino, I. Torre, A. K. Geim, and M. Polini, Phys. Rev. B **94**, 155414 (2016).
[11] D. A. Bandurin, I. Torre, R. K. Kumar, M. B. Shalom, A. Tomadin, A. Principi, G. H. Auton, E. Khestanova, K. S. Novoselov, I. V. Grigorieva, L. A. Ponomarenko, A. K. Geim, and M. Polini, Science **351**, 1055 (2016).
[12] P. S. Alekseev, Phys. Rev. Lett. **117**, 166601 (2016).
[13] T. Scaffidi, N. Nandi, B. Schmidt, and A. P. Mackenzie, and J. E. Moore, Phys. Rev. Lett. **118**, 226601 (2017).
[14] L. V. Delacretaz and A. Gromov, Phys. Rev. Lett. **119**, 226602 (2017).
[15] F. M. D. Pellegrino, I. Torre, and M. Polini, Phys. Rev. B **96**, 195401 (2017).
[16] G. M. Gusev, A. D. Levin, E. V. Levinson, and A. K. Bakarov, AIP Adv. **8**, 025318 (2018).
[17] Z. Qian and G. Vignale, Phys. Rev. B **71**, 075112 (2005).
[18] J. J. Harris, C. T. Foxon, D. Hilton, J. Hewett, C. Roberts, and S. Auzoux, Surface Science **229**, 113 (1990).
[19] T. Kawamura and S. Das Sarma, Phys. Rev. B **45**, 3612 (1992).
[20] C. W. J. Beenakker and H. van Houten, Phys. Rev. Lett. **63**, 1857 (1989).
[21] M. L. Roukes, A. Scherer, S. J. Allen, Jr., H. G. Craighead, R. M. Ruthen, E. D. Beebe, and J. P. Harbison, Phys. Rev. Lett. **59**, 3011 (1987).
[22] G. Timp, H. U. Baranger, P. de Vegvar, J. E. Cunningham, R. E. Howard, R. Behringer, and P. M. Mankiewich, Phys. Rev. Lett. **60**, 2081 (1988).
[23] Y. Hirayama and S. Tarusha, Appl. Phys. Lett. **63**, 2366 (1993).

V. Viscous transport and Hall viscosity in a 2DES

G. M. Gusev,[1] A. D. Levin,[1] E. V. Levinson,[1] and A. K. Bakarov[2,3]
[1]*Instituto de Física da Universidade de São Paulo, 135960-170 São Paulo, SP, Brazil*
[2]*Institute of Semiconductor Physics, Novosibirsk 630090, Russia*
[3]*Novosibirsk State University, Novosibirsk 630090, Russia*

(Received 5 December 2017; revised manuscript received 10 August 2018; published 15 October 2018)

Hall viscosity is a nondissipative response function describing momentum transport in two-dimensional (2D) systems with broken time-reversal symmetry. In the classical regime, Hall viscosity contributes to the viscous flow of 2D electrons in the presence of a magnetic field. We observe a pronounced, negative Hall resistivity at low magnetic field in a mesoscopic size, two-dimensional electron system, which is attributed to Hall viscosity in the inhomogeneous charge flow. Experimental results supported by a theoretical analysis confirm that the conditions for the observation of Hall viscosity are correlated with predictions.

DOI: 10.1103/PhysRevB.98.161303

Considerable progress has been made recently in the nonperturbative understanding of the interaction effects in the electronic transport properties of metals within a hydrodynamic framework [1]. A hydrodynamic description is valid when the electron-electron scattering time is much shorter than the electron-impurity or electron-phonon scattering times. The theory of the hydrodynamic regime, where transport is dominated by a viscous effect, has been developed in many theoretical studies [2–8]. It has been shown that the shear viscosity contribution can be especially enhanced in the case where the mean free path due to the electron-electron interaction l_{ee} is much less than the sample width W, and the transport mean free path l is in the order of or greater than the width, $l \ll W$. In such a hydrodynamic regime, resistivity is proportional to the electron shear viscosity $\eta = \frac{1}{4} v_F^2 \tau_{ee}$, where v_F is the Fermi velocity and τ_{ee} is the electron-electron scattering time $\tau_{ee} = l_{ee}/v_F$ [2]. It has been predicted that resistance decreases with the square of temperature, $\rho \sim \eta \sim \tau_{ee} \sim T^{-2}$, and with the square of the sample width $\rho \sim W^{-2}$ [2–8].

Works demonstrating a feasible way to realize a hydrodynamic regime, so far, have been achieved in experiments with electrostatically defined GaAs wires [9,10] and graphene [11]. Until very recently, experimental studies have been carried out in zero external magnetic field. In order to describe the large negative magnetoresistance in GaAs with high-mobility electrons [12], the theoretical approach has been extended to include the magnetohydrodynamic behavior of two-dimensional (2D) systems [13]. Similar magnetoresistance has been observed in previous studies [14–16], which could be interpreted as a manifestation of the viscosity effects. Recently, it has been demonstrated that palladium cobaltate wires [17] and mesoscopic GaAs structures [18] allow for the study of the underlying physical principles of the viscous system in a magnetic field and the carrying out of experiments to confirm theoretical predictions [13].

One interesting property of a 2D fluid is Hall viscosity, which describes a nondissipative response function to an external magnetic field [12,14–29]. It is remarkable that, besides the importance of Hall viscosity in the context of condensed matter physics [19], it has been demonstrated that Hall viscosity arises in many different and seemingly unconnected fields such as hydrodynamics, plasma, and liquid crystals [30]. It has been shown that classical Hall viscosity can be extracted from transport measurements in the emergent magnetohydrodynamic regime in 2D electron systems [31–33]. Note that such a possibility has been questioned in a paper [13], where just the conventional Hall effect was found. However, one must take into account the higher-order terms in the expansion of the electron distribution function by the angular harmonics of the electron velocity (related to inhomogeneities of a flow) [34]. Therefore the experimental study of the Hall resistivity in a viscous system may provide a useful platform for future theoretical developments in Hall viscosity.

In the present Rapid Communication, we have gathered all requirements for the observation of the hydrodynamic effect and Hall viscosity in a 2D electron system and present experimental results accompanied by a quantitative analysis. For this purpose, we chose GaAs mesoscopic samples with high-mobility 2D electrons. We employ commonly used longitudinal resistance, magnetoresistance, and the Hall effect to characterize electron shear viscosity, electron-electron scattering time, and reexamine electron transport over a certain temperature range, 1.5–40 K. We observe negative corrections to the Hall effect near zero magnetic field, which we attribute to classical Hall viscosity.

Our samples are high-quality GaAs quantum wells with a width of 14 nm and electron density $n \simeq 9.1 \times 10^{11}\,\mathrm{cm}^{-2}$ at $T = 1.4\,\mathrm{K}$. Parameters characterizing the electron system are given in Table I. The Hall bar is designed for multiterminal measurements. The sample consists of three 5-μm-wide consecutive segments of different lengths (10, 20, and 10 μm), and eight voltage probes. The measurements were carried out in a VTI cryostat, using a conventional lock-in technique to measure the longitudinal ρ_{xx} and Hall ρ_{xy} resistivities with an ac current of 0.1–1 μA through the sample, which is sufficiently low to avoid overheating effects. We also compare our results with the transport properties of 2D electrons in a

TABLE I. Parameters of the electron system in a mesoscopic sample at $T = 1.4$ K. Parameters are defined in the text.

n_s (cm^{-2})	μ ($\mathrm{cm}^2/\mathrm{V\,s}$)	v_F (cm/s)	E_F (meV)	l (μm)	l_2 (μm)	η (m^2/s)
9.1×10^{11}	2.5×10^6	4.1×10^7	32.5	40	2.8	0.3

macroscopic sample [34]. Three mesoscopic Hall bars from the same wafer were studied.

Figure 1 shows deviations from conventional Hall resistivity $\Delta\rho_{xy}(T) = \rho_{xy}(T) - \rho_{xy}^{\mathrm{bulk}}$ (referred to as the H1 configuration) as a function of temperature. In order to determine the bulk Hall resistivity $\rho_{xy}^{\mathrm{bulk}}$, we measured the Hall effect in mesoscopic samples in a wider interval of the magnetic field (-0.2 T $< B < 0.2$ T) and high $T \sim 40$ K temperature. Indeed, we found $\rho_{xy}^{\mathrm{bulk}} = -B/en_s$, where e is the electron charge. Figure 1(b) shows the ratio $\Delta\rho_{xy}(T)/\rho_{xy}^{\mathrm{bulk}}$ for different temperatures. One can see a strong (∼10%–20%) deviation from the linear slope. The slope is opposite to the bulk Hall slope at low fields and has the same sign (negative for electrons) at large positive magnetic field and low temperatures. Before analyzing the Hall effect quantitatively

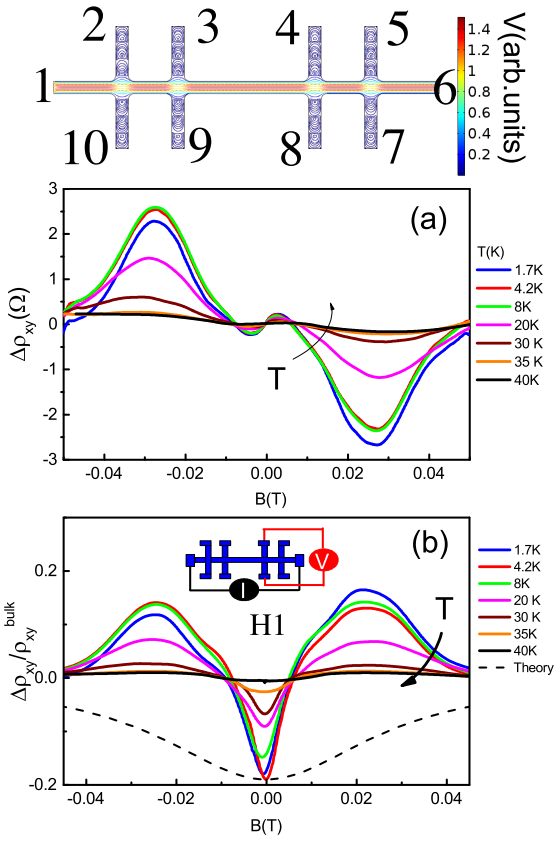

FIG. 1. Top: Sketch of the velocity profile for viscous flow in the experimental setup used in this study. (a) Temperature-dependent deviations from the conventional Hall resistivity $\Delta\rho_{xy}(T)$ of a mesoscopic GaAs well. (b) The ratio $\Delta\rho_{xy}(T)/\rho_{xy}^{\mathrm{bulk}}$ for different temperatures. Dashes: Theory with parameters described in the main text.

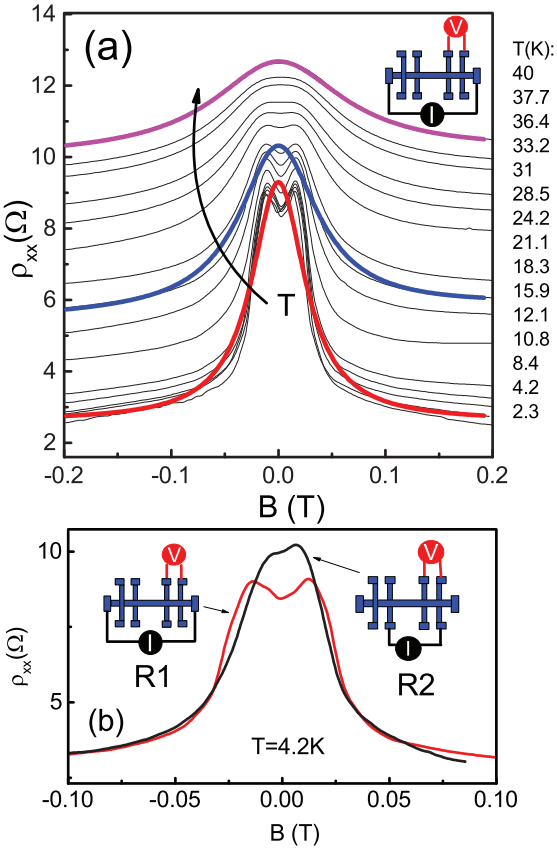

FIG. 2. (a) Temperature-dependent magnetoresistance of a mesoscopic GaAs quantum well. Thick curves are examples illustrating magnetoresistance calculated from Eqs. (1) and (2) for different temperatures: (a) 2.3 K (red), 21.1 K (blue), and 40 K (magenta); (b) 4.2 K (red), 19.2 K (blue), and 37.1 K (magenta). (b) Comparison of the magnetoresistance for different configurations. The schematics show how the current source and the voltmeter are connected for measurements.

and in order to make this analysis more complete, we also measured the longitudinal magnetoresistivity $\rho_{xx}(B)$ in the conventional configuration (referred to as R1). Note that the longitudinal magnetoresistance has been studied previously for different configurations of the current and voltage probes [18]. Figure 2(a) shows $\rho_{xx}(B)$ as a function of magnetic field and temperature. One can see two characteristic features: a giant negative magnetoresistance (∼400%–600%) with a Lorentzian-like shape (except for the small feature near the zero field) and a pronounced temperature dependence of the zero-field resistance. In general, we expect that the character of the viscous flow strongly depends on the geometry and probe configurations [11]. Figure 2(b) shows a comparison of the magnetoresistance measurements in two configurations: a conventional R1 configuration, and when the current is injected between probes 9 and 7 and the voltage is measured between probes 4 and 5 (referred to as the R2 configuration). Strikingly, the resistance at zero magnetic field increases in amplitude and the width of the Lorentzian magnetoresistance is slightly reduced. The features near zero magnetic field are also smeared out. Surprisingly, we found that the resistance at $B = 0$ is independent of temperature for the R2 configuration

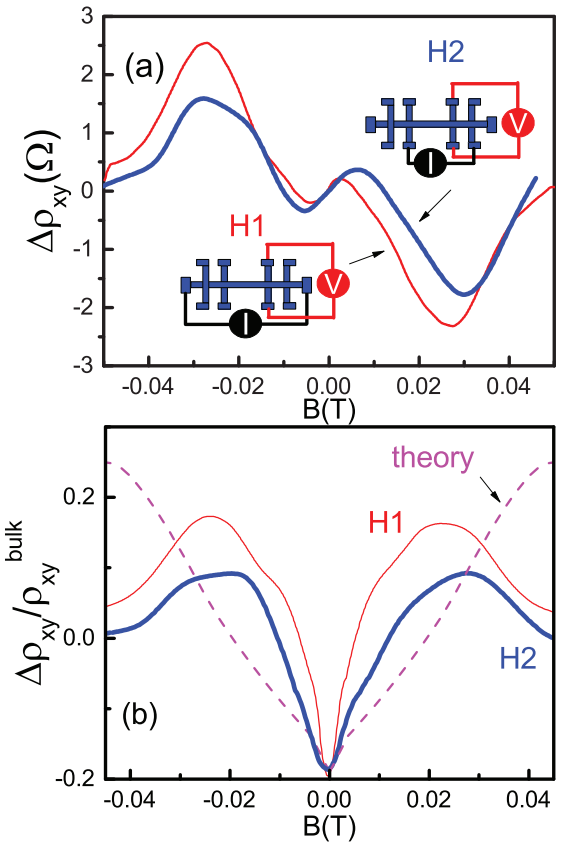

FIG. 3. (a) Hall effect for two configurations, $T = 4.2$ K. (b) The ratio $\Delta\rho_{xy}(T)/\rho_{xy}^{\rm bulk}$ for different configurations. Dashes (magenta) present calculations from ballistic+hydrodynamic theory with parameters described in the main text.

[35]. We attribute these results to the enhancement of the viscous contribution, and further, we prove it by a quantitative comparison with theory. Furthermore, we check the Hall resistance in a modified probe configuration [35]. Figure 3 shows a comparison of the Hall effect in the H1 configuration with the H2 configuration, where the current is injected between probes 9 and 7 and the voltage is measured between probes 4 and 8. One can see that $\Delta\rho_{xy}$ at low magnetic field is wider in the H2 configuration, and, therefore, the ratio $\Delta\rho_{xy}(T)/\rho_{xy}^{\rm bulk}$ exhibits a wider negative peak near zero B.

Classical transport can be characterized on different length scales: the ohmic case ($l \ll W$), ballistic regime ($W \ll l, l_{ee}$), and the hydrodynamic regime ($l_{ee} \ll W \ll l$). In real samples, electrons are scattered by static defects, phonons, and the sample edge. All these processes can be expressed in terms of the scattering relaxation time τ and the boundary slip length l_s. Boundary no-slip conditions correspond to the ideal hydrodynamic case of diffusive boundaries with $l_s = 0$, while the opposite limit (free-surface boundary conditions) corresponds to the ideal ballistic case with $l_s = \infty$.

In the hydrodynamic approach, the semiclassical treatment of the electron transport describes the motion of carriers, when the higher-order moments of the distribution function are taken into account. The momentum relaxation rate $1/\tau$ is determined by an electron interaction with phonons and static defects (boundary). The second moment relaxation rate $1/\tau_2$ leads to the viscosity and contains the contribution from electron-electron scattering and temperature-independent scattering by disorder [13]. It has been shown that conductivity obeys the additive relation and is determined by two independent *parallel* channels: The first is due to the momentum relaxation time and the second is due to viscosity [13,31]. This approach allows for the introduction of the magnetic-field-dependent viscosity tensor and the derivation of the magnetoresistivity tensor [13,31–33],

$$\rho_{xx} = \rho_0^{\rm bulk}\left(1 + \frac{\tau}{\tau^*}\frac{1}{1+(2\omega_c\tau_2)^2}\right), \quad (1)$$

$$\rho_{xy} = \rho_{xy}^{\rm bulk}\left(1 - r_H\frac{2\tau_2}{\tau^*}\frac{1}{1+(2\omega_c\tau_2)^2}\right), \quad (2)$$

where $\rho_0^{\rm bulk} = m/ne^2\tau$, $\tau^* = \frac{W(W+6l_s)}{12\eta}$, viscosity $\eta = \frac{1}{4}v_F^2\tau_2$, and r_H is the numerical coefficient in the order of 1 [13]. At the limit of zero magnetic field ($B \to 0$), one obtains negative corrections to Hall resistivity due to Hall viscosity in the limit of small l_s, $\rho_{xy} = \rho_{xy}^{\rm bulk}[1 - 6r_H(l_2/W)^2]$.

It is instructive to collect the equations for relaxation rates separately, $\frac{1}{\tau_2(T)} = A_e^{\rm FL}\frac{T^2}{[\ln(E_F/T)]^2} + \frac{1}{\tau_{2,0}}$, and $\frac{1}{\tau(T)} = A_{\rm ph}T + \frac{1}{\tau_0}$, where E_F is the Fermi energy, and the coefficient $A_e^{\rm FL}$ can be expressed via the Landau interaction parameter, however, it is difficult to calculate quantitatively (see the discussion in Ref. [13]). The term $A_{\rm ph}$ is due to scattering electrons by acoustic phonons [36,37], and $\frac{1}{\tau_0}$ is the scattering rate due to static disorder. Note that the effective relaxation time τ^* is proportional to the rate $\frac{1}{\tau_2}$ (not time). We represent the evolution of ρ_{xx} at $B = 0$ with temperature in Fig. 4(a) for configurations R1 and R2. We fit the magnetoresistance curves in Fig. 2 and the resistance in zero magnetic field shown in Fig. 4(a) with the three fitting parameters $\tau(T)$, $\tau^*(T)$, and $\tau_2(T)$. Comparing the temperature dependencies, we extract the following parameters, $\tau_{2,0} = 0.8 \times 10^{-11}$ s, $A_e^{\rm FL} = 0.9 \times 10^9$ s^{-1} K^{-2}, $l_s = 3.2$ μm, $A_{\rm ph} = 10^9$ s^{-1} K^{-1}, and $\tau_0 = 5 \times 10^{-10}$ s for configuration R1. For configuration R2 all parameters are the same, except for $l_s = 2.8$ μm. Assuming that the viscous effect is small in a macroscopic sample, we attempt to reduce the number of independent parameters by measuring $\rho_0(T) \sim 1/\tau(T)$ and extracting $A_{\rm ph}$ independently [35]. However, we find a parameter in the macroscopic sample $A_{\rm ph}^{\rm macr} = 1.3 \times 10^9$ s^{-1} K^{-1}, which is slightly higher than in the mesoscopic sample [35]. Table I shows the mean free paths $l = v_F\tau$, $l_2 = v_F\tau_2$, and viscosity, calculated with the parameters, which we extracted from the fit with experimental data. Figure 4(b) shows the dependencies of $1/\tau_2(T)$ and $\tau^*(T)$ extracted from the comparison with theory. Note that $\tau^*(T)$ depends on the boundary conditions, and the difference in its behavior for configurations R1 and R2 could be explained by the difference in the parameter l_s. More diffusive boundary conditions (smaller value of l_s) correspond to stronger hydrodynamic effects.

Now we return to the issue of Hall viscosity. Figure 3(b) shows the dependence $\rho_{xy}/\rho_{xy}^{\rm bulk}$ at $B \to 0$ as a function of temperature for configurations H1 and H2 with calculations obtained independently from magnetoresistance measurements. From comparison with the experiment, we find the adjustable parameter $r_H = 0.4$. This value agrees with numerical calculations performed in the model [31], where

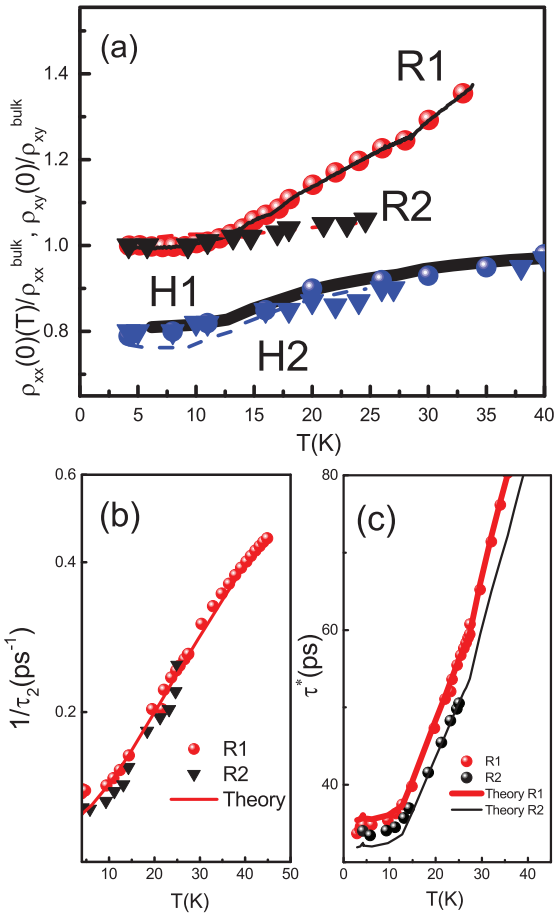

FIG. 4. (a) Temperature-dependent resistivity and the Hall effect of a GaAs quantum well at ($B \to 0$) for different configurations. The solid lines and dashes show calculations based on theoretical Eqs. (1) and (2) with numerical parameters described in the main text. (b) Relaxation time τ_2 as a function of temperature obtained by fitting the theory with experimental results. The solid line is the theory. (c) Relaxation time τ^* as a function of temperature. The solid lines are the theory with parameters presented in the main text.

the parameter $r_H \approx 0.35$ was obtained. The existence of the parameter $r_H < 1$ simply reflects the fact that the viscous Hall correction in Eq. (2) never exceeds 100%, which one expects even for a small ratio l_2/W [see, for example, $l_2/L = 0.04$ and $W/l = 0.1$, considered in Fig. 2(b) of Ref. [31]].

Figure 1(b) shows the Hall curve as a function of B calculated from Eq. (2). Note that the theory predicts a broad Loreantzian-like peak, while a rapid change of the sign is observed near $B \approx 0.01$ T. The discrepancy could be related to the higher-order expansion terms of the angular velocity harmonics of the electron velocity, which are not considered for longitudinal magnetoresistivity [13].

It is important to note that, in the ballistic regime, ρ_{xx} and ρ_{xy} strongly depend on the magnetic field due to the size effects [38–41]. Unfortunately the changing B scale is almost the same $\sim W/R_L$ ($R_L = mV_F/eB$ is the Larmor radius) for both contributions [31], and ballistic and hydrodynamic effects can obscure each other. The magnitude of the ballistic contribution depends on the ratio W/l. In addition, the relative ballistic contribution $\rho_x^{\rm ball}/\rho_0^{\rm bulk}$ exhibits a strong variation with W/R_L because the resistivity directly depends on the relaxation time τ through the boundary scattering, while the relative contribution to the Hall effect $\rho_{xy}^{\rm ball}/\rho_{xy}^{\rm bulk}$ is almost independent of W/R_L, since the Hall effect does not depend on the relaxation time (but rather the size effect) [37–39]. Note that the sign of the effects is the same: The ballistic contribution leads to an increase in boundary scattering, an increase of ρ_{xx}, amplification of the classical Hall slope at $W/R_L = 0.55$, and quenching of the Hall effect near $B = 0$ [39,40]. From comparison with theory, at low temperatures, we found that $\rho_x^{\rm ball} < \rho_0$ [see Fig. 2(a)]. We attempted to fit the magnetoresistance curves with a smaller Lorentzian amplitude, considering the features near $W/R_L = 0.55$ due to the ballistic contribution, and found the fitting parameters $\frac{\tau}{\tau^*}$ only 10% smaller. Note also that since the ballistic and hydrodynamic contributions have the same sign, the B scale of the magnetoresistance is almost the same, when $\rho_x^{\rm ball}$ is added to the magnetoresistance. However, for the same parameters, $\rho_{xy}^{\rm ball}$ is comparable with the hydrodynamic contribution and the ballistic corrections tend to counteract the hydrodynamic corrections in the Hall effect. The ballistic model predicts the quenching of $\rho_x^{\rm ball}$ near $B = 0$ [40,41], therefore, $\rho_{xy}/\rho_{xy}^{\rm bulk}$ is not affected by the ballistic effect in very close proximity to zero field. However, the ballistic contribution leads to a decrease in the B scale of the $\rho_{xy}(B)$, when $\rho_x^{\rm ball}$ is added to the Hall effect. We performed a calculation of the ballistic transport in our sample geometry [35]. We confirmed that the billiard model reproduces earlier numerical calculations. Figure 3(b) shows our numerical results together with the hydrodynamic model. Indeed, the ballistic contribution results in a decrease of the width of the negative peak near $B = 0$. One can see that, for the H2 configuration with stronger hydrodynamic effects (smaller l_s), the calculated curve could be brought in better agreement with the measurements, indicating the relevance of this explanation.

In conclusion, we have measured the evolution of the longitudinal and Hall resistivities with temperature in high-quality GaAs quantum wells. Our observations are correlated with the predictions of classical Hall viscosity for electron flow.

We thank P. S. Alekseev and Z. D. Kvon for helpful discussions. The financial support of this work by FAPESP, CNPq and CAPES (Brazilian agencies) is acknowledged.

[1] A. V. Andreev, S. A. Kivelson, and B. Spivak, Phys. Rev. Lett. **106**, 256804 (2011).
[2] R. N. Gurzhi, Sov. Phys. Usp. **11**, 255 (1968); R. N. Gurzhi, A. N. Kalinenko, and A. I. Kopeliovich, Phys. Rev. Lett. **74**, 3872 (1995).
[3] M. Dyakonov and M. Shur, Phys. Rev. Lett. **71**, 2465 (1993).
[4] M. I. Dyakonov and M. S. Shur, Phys. Rev. B **51**, 14341 (1995).
[5] M. Dyakonov and M. Shur, IEEE Trans. Electron Devices **43**, 380 (1996).

[6] A. O. Govorov and J. J. Heremans, Phys. Rev. Lett. **92**, 026803 (2004).
[7] R. Bistritzer and A. H. MacDonald, Phys. Rev. B **80**, 085109 (2009).
[8] B. N. Narozhny, I. V. Gornyi, M. Titov, M. Schutt, and A. D. Mirlin, Phys. Rev. B **91**, 035414 (2015).
[9] L. W. Molenkamp and M. J. M. de Jong, Solid-State Electron. **37**, 551 (1994).
[10] M. J. M. de Jong and L. W. Molenkamp, Phys. Rev. B **51**, 13389 (1995).
[11] D. A. Bandurin, I. Torre, R. Krishna Kumar, M. Ben Shalom, A. Tomadin, A. Principi, G. H. Auton, E. Khestanova, K. S. Novoselov, I. V. Grigorieva, L. A. Ponomarenko, A. K. Geim, and M. Polini, Science **351**, 1055 (2016).
[12] Q. Shi, P. D. Martin, Q. A. Ebner, M. A. Zudov, L. N. Pfeiffer, and K. W. West, Phys. Rev. B **89**, 201301 (2014).
[13] P. S. Alekseev, Phys. Rev. Lett. **117**, 166601 (2016).
[14] L. Bockhorn, P. Barthold, D. Schuh, W. Wegscheider, and R. J. Haug, Phys. Rev. B **83**, 113301 (2011).
[15] A. T. Hatke, M. A. Zudov, J. L. Reno, L. N. Pfeiffer, and K. W. West, Phys. Rev. B **85**, 081304 (2012).
[16] R. G. Mani, A. Kriisa, and W. Wegscheider, Sci. Rep. **3**, 2747 (2013).
[17] P. J. W. Moll, P. Kushwaha, N. Nandi, B. Schmidt, and A. P. Mackenzie, Science **351**, 1061 (2016).
[18] G. M. Gusev, A. D. Levin, E. V. Levinson, and A. K. Bakarov, AIP Adv. **8**, 025318 (2018).
[19] J. E. Avron, R. Seiler, and P. G. Zograf, Phys. Rev. Lett. **75**, 697 (1995).
[20] I. V. Tokatly and G. Vignale, J. Phys.: Condens. Matter **21**, 275603 (2009).
[21] N. Read, Phys. Rev. B **79**, 045308 (2009).
[22] S.-S. Lee, S. Ryu, C. Nayak, and M. P. A. Fisher, Phys. Rev. Lett. **99**, 236807 (2007).
[23] G. Y. Cho, Y. You, and E. Fradkin, Phys. Rev. B **90**, 115139 (2014).
[24] T. L. Hughes, R. G. Leigh, and E. Fradkin, Phys. Rev. Lett. **107**, 075502 (2011).
[25] N. Read and E. H. Rezayi, Phys. Rev. B **84**, 085316 (2011).
[26] F. D. M. Haldane, Phys. Rev. Lett. **107**, 116801 (2011).
[27] C. Hoyos and D. T. Son, Phys. Rev. Lett. **108**, 066805 (2012).
[28] B. Bradlyn, M. Goldstein, and N. Read, Phys. Rev. B **86**, 245309 (2012).
[29] M. Sherafati, A. Principi, and G. Vignale, Phys. Rev. B **94**, 125427 (2016).
[30] M. Lingam, Phys. Lett. A **379**, 1425 (2015).
[31] T. Scaffidi, N. Nandi, B. Schmidt, A. P. Mackenzie, and J. E. Moore, Phys. Rev. Lett. **118**, 226601 (2017).
[32] L. V. Delacretaz and A. Gromov, Phys. Rev. Lett. **119**, 226602 (2017).
[33] F. M. D. Pellegrino, I. Torre, and M. Polini, Phys. Rev. B **96**, 195401 (2017).
[34] P. S. Alekseev (private communication).
[35] See Supplemental Material at http://link.aps.org/supplemental/10.1103/PhysRevB.98.161303 for details in mesoscopic and macroscopic samples measurements, and calculation of the Hall effect within a semiclassical billiard model, which includes Refs. [12,13,36,37].
[36] J. J. Harris, C. T. Foxon, D. Hilton, J. Hewett, C. Roberts, and S. Auzox, Surf. Sci. **229**, 113 (1990).
[37] T. Kawamura and S. Das Sarma, Phys. Rev. B **45**, 3612 (1992).
[38] M. L. Roukes, A. Scherer, S. J. Allen, Jr., H. G. Craighead, R. M. Ruthen, E. D. Beebe, and J. P. Harbison, Phys. Rev. Lett. **59**, 3011 (1987).
[39] C. W. J. Beenakker and H. van Houten, Phys. Rev. Lett. **63**, 1857 (1989).
[40] Z. Qian and G. Vignale, Phys. Rev. B **71**, 075112 (2005).
[41] T. Geisel, R. Ketzmerick, and O. Schedletzky, Phys. Rev. Lett. **69**, 1680 (1992).

List of Publications

1. G. M. Gusev, A. D. Levin, E. V. Levinson, and A. K. Bakarov “Viscous electron flow in mesoscopic two-dimensional electron gas” *AIP.Adv.**8**.025318 (2018)*
2. A. D. Levin, G. M. Gusev, E. V. Levinson, Z. D. Kvon, and A. K. Bakarov “Vorticity-induced negative nonlocal resistance in a viscous two-dimensional electron system” *Phys.Rev.B.**97**.245308 (2018)*
3. G. M. Gusev, A. D. Levin, E. V. Levinson, and A. K. Bakarov “Viscous transport and Hall viscosity in a two-dimensional electron system” *Phys.Rev.B.**98**.161303 (2018)*

Submitted to publication:

1. A. F. da Silva, A. Levine, E. Levinson, H. Boudinov, and Bo. E. Sernelius “Magnetoresistance of doped germanium” *J.Appl.Phys*

Participation and presentation in conferences and workshops

18th Brazilian Workshop on Semiconductor Physics, São Sebastião, SP, Brazil, August 2017.

- *Microwave induced edge transport in two-dimensional system: comparison with experiment (poster presentation).*